# Current Scan Methods to Predict Radiated Emissions of Automotive Components According to CISPR 25

A Thesis Submitted to the Faculty of Electrical Engineering and Information Technology of Technischen Universität Dortmund in Partial Fulfillment of the Requirements for the Degree of Doctor of Engineering Sciences (Dr.-Ing.)

by

M. Sc. JIN JIA

Dortmund, 2015

Date of Oral Examination:      29.05.2015
Supervisor:                    Prof. Dr.-Ing. Stephan Frei
Second Supervisor:             Prof. Dr.-Ing. Frank Jenau

# Abstract

High density of electrical modules and electronic control units are, nowadays, extensively integrated into modern automotive systems. Estimate and further control the electromagnetic emissions from these components tend to be increasingly indispensable before marketing them. Full-compliance Absorber Lined Shielded Enclosure (ALSE) method or so-called antenna method according to CISPR 25, gives a standardized test configuration to estimate the radiated emissions on component level. However, this emission test method often suffers from the need of a large anechoic chamber, where often only the integrated impact of common-mode current on the test cable bundle is measured. Availability of a specific-size anechoic chamber and repeated experimental runs after a test failure increase the cost for the development of a new product.

Since the common-mode current can be measured quite easily, it is promising to estimate the level of radiated emissions directly from the measured current. This thesis aims to develop a common-mode current based method to predict the radiated emissions according to CISPR 25 and discuss its applicability based on several complex test cases. Different problems linked to this approach have to be solved. Firstly, appropriate common-mode current acquisition methods are required. Secondly, a flexible common-mode radiation model of the cable bundle is required. Thirdly, in order to get comparable data the real ALSE-test environment has to be taken into account. For the mentioned problems, different solutions are developed and discussed. The proposed solutions are applied to several cable structures and a real stepper-motor drive system. Capabilities and limitations are shown and discussed.

# Contents

# Nomenclature and Abbreviations

| | |
|---|---|
| $\alpha$ | attenuation coefficient |
| $\beta$ | phase coefficient |
| $C'$ | capacitance |
| $L'$ | inductance |
| $R'$ | electrical resistance |
| $G'$ | electrical conductance |
| $Y'$ | admittance |
| $Z'$ | impedance |
| $v_0$ | speed of light in vacuum $= 299.79 \cdot 10^6$ m/s |
| $\varepsilon_0$ | vacuum permittivity $= 8.852 \cdot 10^{-12}$ F/m |
| $\varepsilon_r$ | relative static permittivity |
| $f$ | frequency |
| $\gamma$ | propagation coefficient |
| $\gamma_{com}$ | common-mode propagation coefficient |
| $H$ | magnetic field intensity |
| $E$ | electric field intensity |
| $j$ | imaginary unit |
| $I$ | electric current |
| $V$ | voltage |
| $V_{com}$ | common-mode voltage |
| $I_{com}$ | common-mode current |
| $\sigma$ | conductivity |
| $\mu_0$ | vacuum permeability/ magnetic constant $= 4\pi \cdot 10^{-7}$ H/m |
| $\mu_r$ | relative magnetic permeability |
| $\omega$ | angular frequency |
| $v$ | current phase velocity |
| $v_{com}$ | common-mode current phase velocity |
| $Z_C$ | characteristics impedance |
| $Z_{com}$ | common-mode characteristics impedance |
| $\Gamma$ | transmission line reflection factor |

| | |
|---|---|
| ALSE | Absorber Lined Shielded Enclosure |
| WLAN | Wireless Local Area Networks |
| Wi-Fi | Wireless Fidelity |
| EMI | Electromagnetic Interference |
| EMC | Electromagnetic Compatibility |
| EUT | Equipment under Test |
| FDTD | Finite-Difference Time-Domain |
| MoM | Moment Method |
| FFT | Fast Fourier Transform |
| BB | Broadband |
| NB | Narrowband |
| PWM | Pulse Width Modulation |
| SNR | Signal-to-Noise Ratio |
| TEM | Transverse Electromagnetic |
| MTL | Multiconductor Transmission Line |
| PEC | Perfect Electric Conductor |
| EFIE | Electric Field Integration Equation |
| BEM | Boundary Element Method |
| FIT | Finite Integration Technique |
| TLM | Transmission-Line-Method |
| TDIE | Time-Domain Integral Equation |
| PCB | Printed Circuit Board |
| TRR | Trust-Region-Reflective |
| DC | Direct Current |
| VNA | Vector Network Analyzer |
| BW | Band Width |
| MT | Measure Time |
| SWR | Standing Wave Ratio |
| CVP | Common-Mode Voltage Probe |

# Introduction

A variety of electrical modules and electronic control systems are integrated into modern automotive systems, with the aim to improve vehicle safety, energy efficiency and drive comfort, such as ABS, Airbag, Energy manage system, Multimedia entertainment system etc. [1]. Compared with traditional combustion engine vehicles, hybrid- and electric-vehicle power systems require higher voltage architecture and additional power conversion systems (DC/DC converter and DC/AC inverter) [2]. Novel automotive real-time Ethernet [3] as well as car2car technology [4] based on Wireless Local Area Networks (WLAN) or Wireless Fidelity (Wi-Fi) may be incorporated into traditional vehicle communication system, which largely extends the frequency bandwidth. These new technologies and facilities, on the one hand, are capable to meet consumer expectations. On the other hand, different types of electrical and electronic equipments coexisting in the confined space of a vehicle can increase the electromagnetic emissions level significantly, and even risk the functional safety of some sensitive devices [5]. Due to a large number of electrical and electronic components in vehicles, which are characterized by high clock-frequency and short launch-cycle, Electromagnetic Interference (EMI) estimations for these components are essential procedures in a whole-car development process.

As the primary interconnection medium of electrical or electronic systems, cable bundles play a vital role in automotive Electromagnetic Compatibility (EMC) problems, such as conducted emissions, radiated emissions, immunity and signal integrity [7]-[8]. They provide main paths for various electromagnetic interferences: as conducted paths, interference sources might directly be injected into sensitive equipments; as receiving antennas, radiated emissions from environment or peripheral equipment also could be coupled into sensitive systems; particularly as highly effective transmitting antennas, most of the electrical or electronic devices attached by cable bundles can emit radiated interferences to other systems or equipments. Previous work in [6] shows that most under tested systems fail to pass commercial radiation limits due to the radiated emissions of cable bundles in these systems.

Based on the fact that the cable bundle plays a main role in radiated emissions in real vehicles, common commercial radiation test methods require the Equipment-Under-Test (EUT) to be connected to a cable bundle of a certain length, such as the ALSE method in accordance with CISPR 25. This test method is often assumed to be the most reliable, showing good correlation with the device emission behavior in a complete vehicle. In order to guarantee test reliability and repeatability, regulations are issued to specify this method in terms of the test site, the test set-up, as well as the corresponding radiation limits [9]. Particularly, it requires an anechoic chamber to eliminate extraneous disturbance and avoid wall reflections. Most equipment

manufacturers cannot afford this facility due to cost and space constrains. This expensive full-compliance ALSE method can lead to high development-costs and time-scales, especially when a device repeatedly fails to meet the required regulations. For these reasons, low-cost but highly-reliable alternative methods are desirable. In the past, some alternative methods to the ALSE test method have been developed to estimate the radiation of electrical components with simple equipments:

The first group of these methods is the transfer function based approach. One transfer function is based on the cable common-mode current and the test antenna voltage, which is firstly introduced to estimate the radiation of components in [10]. This method generates a set of transfer functions of currents at different cable positions and antenna voltages. The deficient current phase distribution is approximated by an empirically-derived function. The radiation estimation for a cable bundle is the sum of the measured cable segmental current amplitudes multiplying available segmental transfer functions. An advanced version of this method is developed in [11]. Differing from the current phase approximation by an empirically-derived function, it views the measured current amplitude distribution as a composition of a series of propagation current waves with different phase shifts, each of which can be calculated based on the maximum and minimum positions of measured amplitude distribution. In these propagation current waves, the maximum current envelope is assumed to be responsible for the radiated field. The advantage of this transfer function based approach is easy to incorporate the influence factors from an ALSE test environment, such as the anechoic chamber characteristic and the near field coupling of test antenna and under test set-up. However, in this approach the current phase shift along the cable bundle is only roughly approximated by an empirically-derived function which would lead to serious inaccuracies, especially at high frequencies. The calculated phase shift based on the maximum current envelope requires the cable transmission line propagation constant. Moreover, only consideration of the maximum current envelope in the radiation estimation is not accurate. Additionally, the vertical currents from the cable to ground plate are not considered in the transfer functions. The vertical current component is also an important contribution to the radiated field both in vertical and horizontal polarization. Therefore, this transfer function based radiation prediction method is limited below 200 MHz. Another transfer function is based on the simplified monopole antenna voltage and the real test antenna voltage [12]. This method firstly uses a simple monopole antenna close to the calibration wire set-up according to ALSE method. And then it obtains a transfer function of the monopole antenna voltage and the real test antenna voltage. In real cable bundle radiation simulations, this transfer function can correlate the simulations to real ALSE measurements. The advantage of this transfer function based approach can speed up generation of cable simulation model, without the consideration of modeling the complex ALSE environment.

However, only the vertical field in this transfer function is presented in the verifications. Additionally, this method cannot be free from the problems of modeling the detailed cable bundle compositions and modeling the complex EMI behaviors of various EUTs. The last transfer function is based on the near field distribution on Huygens surface around test set-up and the test antenna voltage [13]. This novel approach divides the radiation estimation problem from ALSE set-ups into two parts: a near-field problem in small scale; and an ALSE test set-up problem in large scale. This method can effectively simplify the radiation simulation considering the large-scale ALSE set-up. The accuracy can be acquired below 5 dB error compared with antenna measurements, when the antenna model is accurate enough. However, in this phase this method is not applied to a real application which has to encounter the challenges of the near-field measurement efficiency and the near-field data (amplitude and phase) reliability.

The second group of these methods is the equivalent circuit model based approach. An equivalent circuit model is proposed to rapidly estimate the radiated emissions due to common-mode currents along the cable attached to a switching power supply [14]. This equivalent circuit method models the cable using the transmission line theory, and models the coupling effects from the cable to the test antenna using lumped capacitances. Based on these lumped parameters, test antenna voltage can be simulated. A study [15] establishes equivalent circuit models for different components in a DC/AC inverter system. Moreover, it uses an equivalent circuit to simulate a rod antenna measurement below 30 MHz. However, these equivalent circuits and the lumped parameters are only available for the specified applications and layouts, which are not suitable for more general test cases. Additionally, the lumped circuit models are inaccuracy as the frequency rises.

The third group of these methods is the full-wave numeric algorithms based approach. In [16], EMI currents from a DC/DC converter system are measured, which are used as the radiation source of a simple cable. Finite-Difference Time-Domain (FDTD) model of this cable set-up is established to estimate the radiated emissions from this system. In [17], a simplified model for the common-mode radiation of a cable bundle is proposed. All the conductors in a cable bundle are reduced to several equivalent conductors by simplifying the transmission line parameter matrix and the termination impedances. And then the radiated emissions of this reduced cable bundle can be simulated based on Moment method (MoM) with higher efficiency. In [18], a MoM model for the ALSE test configuration is constructed to validate real ALSE test set-ups. These full-wave models based approach are often effective for very simple configurations. However, a general cable bundle with complex wires, which needs detailed modeling, is still a challenge for the computation resource. Additionally, the stochastic radiation characteristic due to random wire positions within a real cable bundle is also beyond full-wave simulations [19]. More importantly,

complex behaviors of an anechoic chamber are difficult to describe only based on simulation models.

These three groups of alternative methods to the real ALSE test method are listed in Table R.1, but they are often limited by at least one side of flowing aspects: the accuracy in wider frequency, more versatility in general applicability, or the correlation to the real ALSE test method. Therefore, a common-mode current based alternative is proposed to improve these aspects in this thesis. In order to realize radiated field predictions for more complex applications in a wider frequency range, three problems have to be solved: Accurate common-mode current (amplitude and phase) measurement are needed. Flexible and easily adjustable common-mode cable models must be found. Simple to use radiation models considering the real environment used in CISPR 25 ALSE method is required.

**Table R.1**  Typical alternative methods to the ALSE method in recent publications

| Method | Input | Output of Field | | Verification Case | Maximum Error | Ref. |
|---|---|---|---|---|---|---|
| | | Polarization | Frequency Range | | | |
| Empirically-Derived Transfer function | Cable Current Distributions | Vertical Polarization | 10 MHz to 190 MHz | A Cable Driven by Generator | 5 dB | [10] |
| Multiple-Segment Transfer function | Cable Current Distributions | Vertical and Horizontal Polarization | 0.15 MHz to 200 MHz | A Real Wiper-Motor System | 5 dB (<30 MHz) 20 dB (>30 MHz) | [11] |
| Monopole Antenna-Based Transfer function | Vertical Field from Monopole Antenna | Vertical Polarization | 0.1 MHz to 1 GHz | A 10-wire Cable Driven by a Network Analyzer | Less than 10 dB | [12] |
| Huygens-Based Transfer function | Near-Field Distributions on Huygens Surface | Vertical and Horizontal Polarization | 30 MHz to 1 GHz | A Cable Driven by a Network Analyzer | Less than 5 dB | [13] |
| Equivalent Circuit Method | Lumped Parameters | Vertical Polarization | 10 MHz to 400 MHz | A Switching Power System | 5 dB (<200 MHz) 15 dB (>200 MHz) | [14] |
| Equivalent Circuit Method | Lumped Parameters | Vertical Polarization | 150 kHz to 30 MHz | A Real Electrical Driven System | Less than 3 dB | [15] |
| MoM | Geometrical Parameters and Voltage Source | Vertical and Horizontal Polarization | 150 KHz to 1 GHz | A Designed Radiator Driven by a Network Analyzer | Less than 6 dB | [18] |

# 1 Radiation Estimations on Automotive Component Level

In the radiation estimation for automotive electrical and electronic components by the ALSE method, the attached cable bundle is often the dominant radiator due to its long structure. Wires with length in the order of wavelength are effective emitting antennas. The conducted EMI energy, in the form of flowing current on the wire, is generated from various automotive devices. Therefore, this chapter firstly discusses the main types of automotive electromagnetic interference, then provides an overview of the ALSE test method for the radiated emissions on component level, and finally concludes the general modeling methods for basic radiators.

## 1.1 Automotive Electromagnetic Interferences

The automotive cable harnesses links a variety of electrical loads and electronic controller units in the vehicle. These loads and units can be basically categorized into four types: powertrain such as the electronic ignition control; driving safety such as the airbag release control; driving comfort such as the heater and air-conditioner; communication such as the radio system [1], as shown in Figure 1.1.
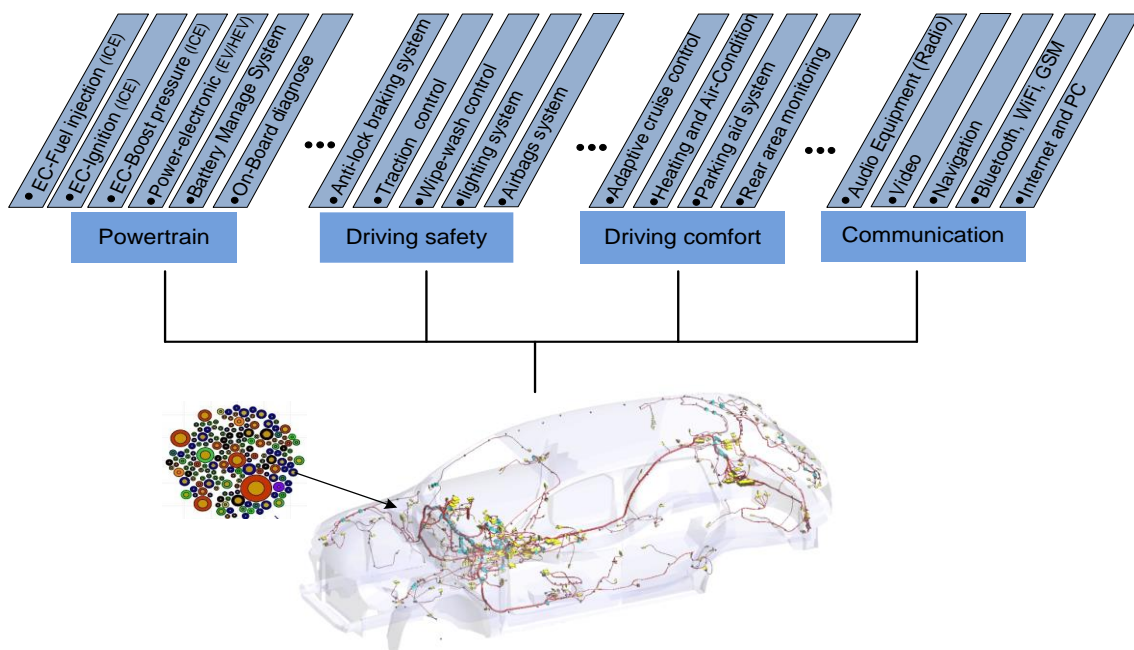


**Figure 1.1** Automotive harness network with the different electrical loads [1], [20]
(EC: Electronic Control; IEC: Internal Combustion Engine; EV: Electrical Vehicle; HEV: Hybrid Electrical Vehicle)

These components guarantee normal vehicle functions, but they also produce unwanted electromagnetic interference. According to CISPR 25 [9], the interference noises can be divided into two main types: Broadband (BB) noise and Narrowband (NB) noise. The spark ignition system in internal combustion is representative of a BB noise source [21]. Electrical motors are another common BB noise source in a vehicle, especially the brush-motor. Silicon controlled rectifier devices truncate the sine wave at certain points to be a portion of a square wave with harmonic contents, which can be also viewed as a BB noise source. BB noise is characterized by continuous frequency spectrum distribution, and usually produces a solid band of emissions in observed frequency range. In contrast, the nature of NB emissions is that the noise amplitude is concentrated at specific frequencies. Microprocessors, power transistors, Pulse Width Modulation (PWM), switching transistors and digital logic are typical NB emission sources in a vehicle [22]. Figure 1.2 presents the typical spectrum characteristics of BB noise and NB noise [1].
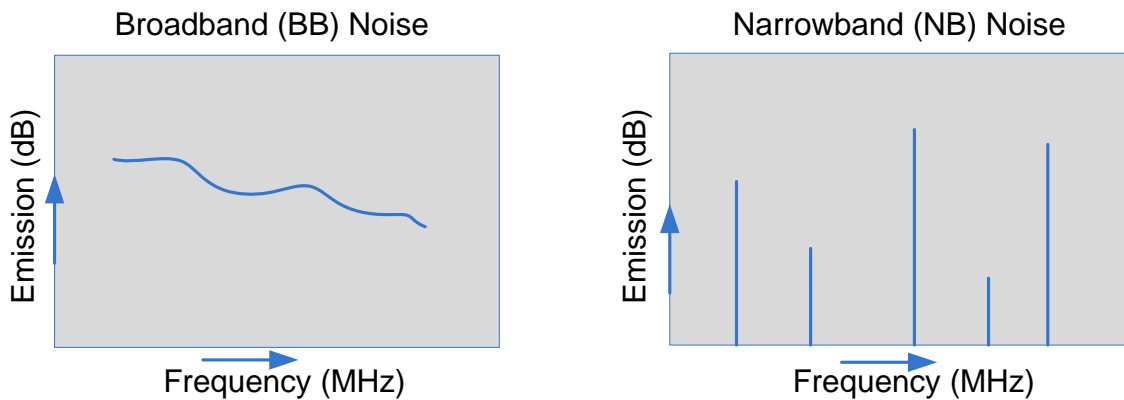


**Figure 1.2** Typical spectrum characteristics of the broadband noise and the narrowband noise [1]

The broadband or narrowband noise originates from electrical or electronic components, and is conducted through the attached cables. These cables act as antennas, emitting unwanted radiated emissions, which may interfere with frequency bands reserved for automotive functions such as the radio system. Figure 1.3 presents the basic frequency bands utilized by the broadcast and mobile service in a vehicle environment, according to CISPR 25 [9]. Typical broadband noise from ignition sparks may reduce the Signal-to-Noise Ratio (SNR) and the sensitivity of FM radio. Narrowband harmonics of PWM [23] or disturbances from a bus system [24]-[25] may interfere with the AM or FM radio band, and degrade audio quality. Sometimes the VHF communication system in a transport truck cannot be utilized due to the broadband and narrowband emissions [22]. Therefore, compliance with regulations and measures to address these noise sources during a new device development are of great significant.
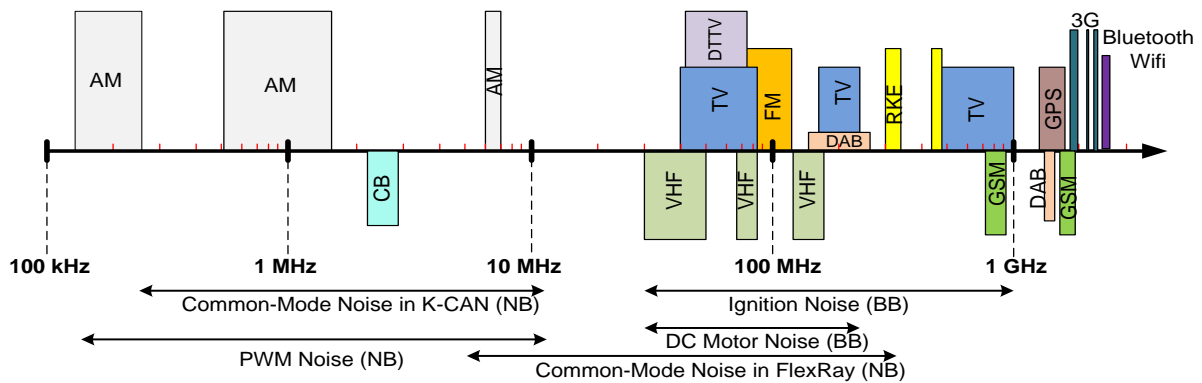
**AM:** Amplitude Modulation; **CB:** Citizens Band; **VHF:** Very High Frequency; **DAB:** Digital Audio Broadcasting; **VHF:** Very High Frequency; **TV:** Television; **DTTV:** Digital Terrestrial Television; **RKE:** Remote Keyless Entry; **GPS:** Global Positioning System; **GSM:** Global System mobile; **3G:** Third Generation

**Figure 1.3** Frequency bands for broadcast and mobile services in a vehicle environment

# 1.2 ALSE Measurement Method for Radiated Emissions

In order to estimate electromagnetic disturbances mentioned above, many countries have issued the regulations about the radiated emissions of automotive components [26]. CISPR 25 is widely referred by these regulations in the transport industry. Similar test standards are also required in other application areas, for example, the military equipment test standards: MIT-STD-461E/MIT-STD-461F [27]-[28]. In addition to governmental regulations, vehicle manufacturers themselves usually establish more strict radiated emissions requirements to select the components [29], for example DC-brush-motors, electrical motors and some active electronic modules. Therefore, effective radiation compliance estimation and EMI control design in a product development are greatly significant for manufactures.

Since the ALSE method provides best correlation to device emissions in a complete vehicle, this method is adopted by CISPR 25 and other standards as a full-compliance test approach to estimate radiated emissions from automotive components. ALSE specifies the test environment of an anechoic chamber, the test configuration, the test receiving equipments, and the arrangement of EUT, harness, and load simulator. An active Rod antenna with high impedance pre-amplifier shall be used to measure the vertical electric field from 150 kHz to 30 MHz, as shown in Figure 1.4. A wideband antenna has better test efficiency, and it is used to measure radiated emissions in both vertical and horizontal polarization from 30 MHz to 1 GHz. For example a Biconical antenna is applied from 30 MHz to 200 MHz and a log-periodic antenna from 200 MHz to 1 GHz, as shown in Figure 1.5. A compact Bilog antenna [26], which can cover the whole frequency range from 30 MHz to 1 GHz, can also be used in the radiated emission test.

7
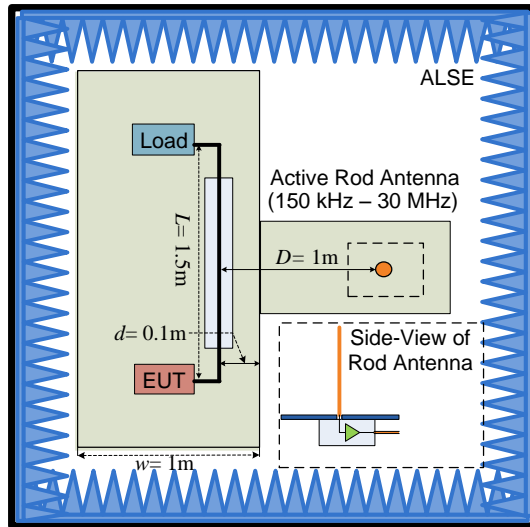
**Figure 1.4** Basic radiation test set-up for automotive components – active Rod antenna (150 kHz to 30 MHz)
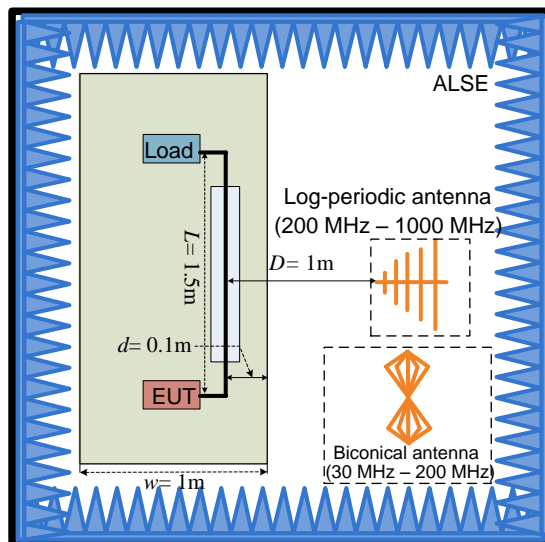


**Figure 1.5** Basic radiation test set-up for automotive components – Biconical antenna (30 MHz to 200 MHz) or – Log periodic antenna (200 MHz to 1 GHz)

In ALSE method the reference point of the receiving antenna is located about 1 meter from the cable center ($D$ = 1 m as denoted in Figure 1.4 and Figure 1.5). Within this distance, the configuration under test shows complex radiation characteristics at different frequencies. For simplification the electromagnetic field around a radiating object can be divided into near field and far field. Near-field behavior dominates close to the radiating object but decay rapidly as distance increases from the object. Far-field behavior dominates at greater distances. However, the boundary between the near-field region and the far-field region changes with different radiating structures. For example, [30] defines a far-field region when the distance is larger than $3\lambda$ for a wire-antenna and $2S^2/\lambda$ for an

aperture-antenna. Here $S$ is the largest dimension of the radiator and $\lambda$ is the wavelength of electromagnetic wave. For an electromagnetically short dipole [31], the near-field is defined as the region within a radius $r << \lambda/2\pi$, while the far-field is defined as the region for which $r >> \lambda/2\pi$. The region within a radius $r > \lambda/2\pi$ is defined as intermediate region or transition zone. And from the radiation expression of an electric dipole [32], the electric field includes three parts as shown in (1.1): a radiation erm $f_R(1/r)$ which ominates the far-field region, an induction term $f_I(1/r^2)$ which dominates the radiative near-field region and transition zone, and an electrostatic field term $f_E(1/r^3)$ which dominates the reactive near-field region:

$$E = f_R(1/r) + f_I(1/r^2) + f_E(1/r^3) \qquad (1.1)$$

Here $r$ indicates the distance from the observation point to the electric-dipole.

According to the field region division from a short dipole antenna, for the frequency band measurement from 150 kHz to 30 MHz ($D \leq 0.63 \cdot \lambda_{30MHz}/2\pi$), the active Rod antenna is located in the reactive near-field zone which is dominated by the electrostatic field term $f_E(1/r^3)$ [33]. In this reactive zone of the radiating structure, the field measurement is influenced by the reactive and coupling effects with nearby conductors. Moreover, the absorber does not work well at low frequencies. This might be one reason that electric field measurement by active Rod antenna below 30 MHz often suffers from relatively lower accuracy and repeatability. Due to the self-capacitance and self-inductance of the under tested radiating object, resonance effect is often a problem in active Rod antenna test [34]. Measures have been proposed to suppress this resonance effect, through improving the connection condition between the metallic table and the chamber wall [35], and modifying the counterpoise grounding or the height of active Rod antenna [36]. For the frequency band measurement from 30 MHz to 200 MHz ($0.63 \cdot \lambda_{30MHz}/2\pi \leq D \leq 4.2 \cdot \lambda_{200MHz}/2\pi$), the Biconical antenna is located in the radiative near-field and transition zone which is mainly dominated by the induction term $f_I(1/r^2)$ [32], if $3\lambda$ is assumed as the boundary from transition zone to far-field region. In the radiative near-field, the "re-radiating" effect induced by the nearby conductor and the coupling effect between the transmitter and the receiver, both can affect the output power of transmitter and the validity of the antenna factor [37]. For the frequency band measurements from 200 MHz to 1GHz ($4.2 \cdot \lambda_{200MHz}/2\pi \leq D \leq 21 \cdot \lambda_{1GHz}/2\pi$), the Log-periodic antenna is mainly located in the transition zone, if $3\lambda$ is assumed as the boundary from transition zone to far-field region. In the transition zone, there exist common effects from both the near-field and far-field components, so that the Log-periodic antenna measurement is also not free from the coupling effects in this frequency range.

The complex test environment will influence the test accuracy in radiation estimation [38]-[39]. There are three typical measurement error sources. Firstly, the

anechoic chamber brings uncertainty due to slots in the floor or door and reflections from the non-perfect absorber walls. Therefore, to guarantee the test reliability by ALSE method a couple of validation methods for the anechoic chamber are proposed in [18], [40]. Secondly, the receiving antenna in the ALSE method is often calibrated under far-field condition to get the antenna factor. However in a real test configuration, the antenna test is often influenced by the near-field effects, so that the antenna factor provided by the manufacturers is not valid considering this condition [41]. Thirdly, uncertainties due to test connection cables and equipments often reduce the output voltage accuracy of antenna. For this reason, tolerances for uncertainties in the EMC test procedure are regulated in [42].

Compared with the above technical points, the economic cost of radiation estimation by ALSE test method is a more critical issue for the equipment manufacturers. The high-cost anechoic chamber is space-consuming, which prevents it from being widely established by many manufacturers. During a new product development, especially when a device repeatedly fails to meet specifications, ALSE measurements can become a reason for high development-costs. Therefore, alternative test methods are often desirable, showing high correlation to the full-compliance ALSE method.

# 1.3  Modeling Methods for Radiated Emissions

In a product development process, simulation methods often help the designer to better understand the sources of system interference, to achieve higher EMI reductions, and further reduce the time-to-market through fast product optimization and iterations. Compared with the challenges of complex full-vehicle radiation modeling, radiation modeling from component test set-ups as shown in Figure 1.4 and Figure 1.5 is much simpler. This configuration mainly consists of cable bundle, EUT and load simulator, test antenna, metallic ground plate, and anechoic chamber. The cable bundle, which is the main radiator, can be modeled using transmission line theory or full-wave numeric algorithms. The EMI behaviors from the EUT can be simulated through circuit simulators [25] or measured through direct measurements. The metallic ground plate, the receiving antenna and the anechoic chamber are the main influence factors to radiation characteristics of the cable bundle. Ground plate can be modeled by simple radiation models [44], but the complex antenna and chamber models need more accurate full-wave numeric algorithms [18], [35].

## 1.3.1  Transmission Line Models

Wire attached to the EUT often dominates the radiation, especially when the wire length is in the same order of wavelength. As the main radiation source, the current distribution flowing through the wire can be simulated using transmission line

theory, which is a classical method in electrical engineering to describe the voltage and current wave propagating along the axis of a Transverse Electromagnetic (TEM) field guiding structure, as shown in Figure 1.6.
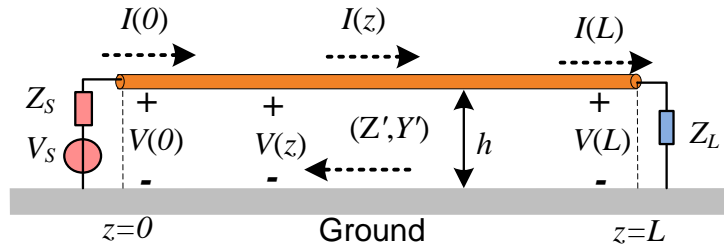


**Figure 1.6** Voltage and current on a single wire parallel to a ground

The voltage and current distributions as shown in Figure 1.6 on a two-wire transmission line structure (ground acts as the return path) are governed by the telegrapher equations [45]-[48]:

$$\frac{\partial V(z)}{\partial z} + Z'I(z) = 0 \tag{1.2}$$

$$\frac{\partial I(z)}{\partial z} + Y'V(z) = 0 \tag{1.3}$$

Here $Z'$ and $Y'$ are the per-unit-length impedance and admittance of transmission line, and are defined by (1.4) and (1.5) respectively. Quantities $L'$, $R'$, $C'$ and $G'$ are the per-unit-length inductance, resistance, capacitance and conductance respectively, representing geometry and material properties of transmission line structure.

$$Z' = R' + j\omega L' \tag{1.4}$$

$$Y' = G' + j\omega C' \tag{1.5}$$

In order to calculate the current and voltage at the terminals, a two-port network is adopted to represent a transmission line of length $L$, as shown in Figure 1.7:



**Figure 1.7** Representation of two-wire transmission line as a two-port network [48]

One of the most useful forms of two-port parameters for a line is the chain-parameter matrix $\Phi$ $(L)$ representation [30]. It can relate the terminal voltages and currents according to:
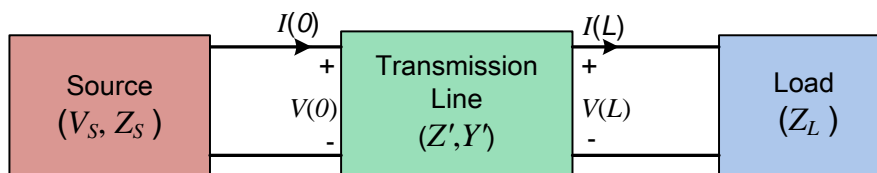
$$
\begin{bmatrix} V(L) \\ I(L) \end{bmatrix} = \begin{bmatrix} \cosh(\gamma L) & -Z_C \sinh(\gamma L) \\ -\dfrac{\sinh(\gamma L)}{Z_C} & \cosh(\gamma L) \end{bmatrix} \begin{bmatrix} V(0) \\ I(0) \end{bmatrix}
$$

$$
= \begin{bmatrix} \Phi(L) \end{bmatrix} \begin{bmatrix} V(0) \\ I(0) \end{bmatrix}
$$

(1.6)

In (1.6) $\gamma$ and $Z_C$ represent the transmission line propagation constant and the characteristic impedance, which are defined by the functions of per-unit-length parameters:

$$
\gamma = \sqrt{Z'Y'} \qquad Z_C = \sqrt{Z'/Y'}
$$

(1.7)

If the source and load terminals can be represented by the equivalent models in Figure 1.6, the terminal voltages $V(0)$, $V(L)$ and currents $I(0)$, $I(L)$ can be calculated, through combining the above two-port relationship in (1.6) and the terminal boundary conditions (1.8) and (1.9) [48]:

$$
V(0) = V_S - Z_S I(0)
$$

(1.8)

$$
V(L) = Z_L I(L)
$$

(1.9)

The current distributions on the transmission line are more important for radiation prediction. Instead of directly solving the differential equations (1.2) and (1.3) [47], another solution is to divide the long line into a cascade of sections, where each section is an individual two-port network representation. The overall chain-parameter matrix $\Phi$ $(L)$ is the product of the chain-parameter matrices $\Phi_i(\Delta z_i)$ of each individual section [48]:

$$
\Phi(L) = \Phi_1(\Delta z_1) \times \cdots \times \Phi_i(\Delta z_i) \times \cdots \Phi_n(\Delta z_n)
$$

(1.10)

The voltage and current at node $z_i$ can be derived from the previous node $z_{i-1}$:

$$
\begin{bmatrix} V_i(z_i) \\ I_i(z_i) \end{bmatrix} = \begin{bmatrix} \Phi_i(\Delta z_i) \end{bmatrix} \begin{bmatrix} V_{i-1}(z_{i-1}) \\ I_{i-1}(z_{i-1}) \end{bmatrix}
$$

(1.11)

By obtaining the voltage and current at the start or end points of the overall transmission line from (1.6) - (1.9), the quantities at each interior node can be calculated. This cascaded approximation is especially useful for non-uniform transmission lines, where the per-unit-length parameters vary along the line axis.

However, an automotive cable bundle usually comprises many of wires. Therefore, a Multiconductor Transmission Line (MTL) model can be used to describe voltages and currents propagating along wires in cable bundle. Figure 1.8 shows a cable bundle parallel to a ground plane.
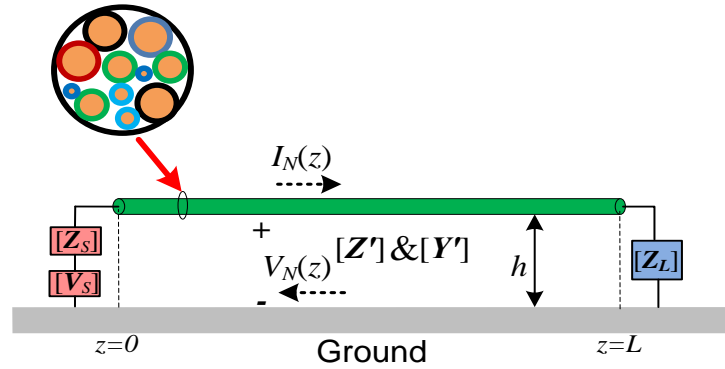


**Figure 1.8** Voltages and currents on a cable bundle parallel to a ground plane

Similar to the two-wire transmission line the voltage and current wave behavior in each wire in the $(N+1)$-wire MTL can be described by telegrapher equations (1.2) and (1.3). However, the voltage and current quantities become $N$-dimensional vectors $[V(z)]$ and $[I(z)]$; the geometry and material properties of MTL become a $N{\times}N$-dimensional per-unit-length impedance matrix $[Z']$ and an admittance matrix $[Y']$. Due to the coupling effects between wires of MTL, the voltage and current at each wire depend on the other wires. Taking the terminal boundary conditions into consideration, a generalized network representation for MTL can be drawn, as shown in Figure 1.9:
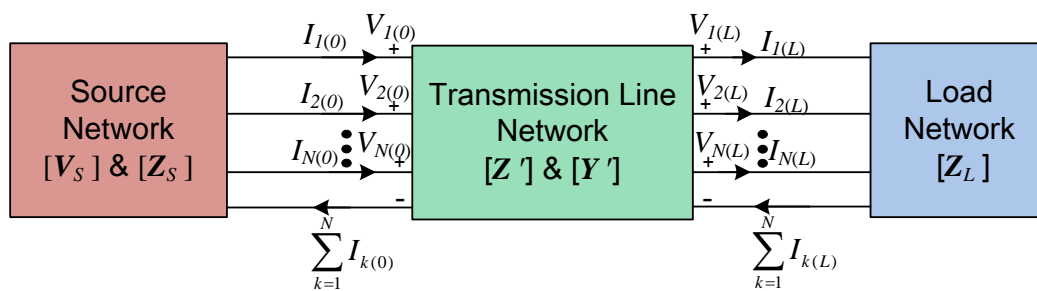


**Figure 1.9** Representation of multiconductor transmission line as a two-port network [48]

If the source and load networks are linear, these linear combinations of terminal voltage and current for each wire can be represented by the equivalent model in Figure 1.6 [48]. But the $[V_S]$ is $N$-dimensional vector which contains the sources in the source network. $[Z_S]$ and $[Z_L]$ are as $N{\times}N$-dimensional matrices which contain the impedances in the source and load network. Furthermore, chain-parameter matrix can be extended to represent $(N+1)$-wire MTL network using similar expressions:

$$\begin{bmatrix} \boldsymbol{V}(L) \\ \boldsymbol{I}(L) \end{bmatrix} = \begin{bmatrix} \cosh(\sqrt{\boldsymbol{Z}'\boldsymbol{Y}'}L) & -\boldsymbol{Z}_C \sinh(\sqrt{\boldsymbol{Y}'\boldsymbol{Z}'}L) \\ -\boldsymbol{Y}_C \sinh(\sqrt{\boldsymbol{Z}'\boldsymbol{Y}'}L) & \cosh(\sqrt{\boldsymbol{Y}'\boldsymbol{Z}'}L) \end{bmatrix} \begin{bmatrix} \boldsymbol{V}(0) \\ \boldsymbol{I}(0) \end{bmatrix}$$

$$= \begin{bmatrix} \hat{\boldsymbol{\Phi}}(L) \end{bmatrix} \begin{bmatrix} \boldsymbol{V}(0) \\ \boldsymbol{I}(0) \end{bmatrix}$$

(1.12)

In an ordinary $(N+1)$-wire MTL, the per-unit-parameter matrices $[\boldsymbol{Z}']$ and $[\boldsymbol{Y}']$ do not commute, i.e. $[\boldsymbol{Z}'][\boldsymbol{Y}'] \neq [\boldsymbol{Y}'][\boldsymbol{Z}']$, so the proper order of multiplication in (1.12) must be treated cautiously. Moreover the characteristic impedance $[\boldsymbol{Z}_C]$ and admittance matrices $[\boldsymbol{Y}_C]$ can be derived trough diagonalization of product matrices $[\boldsymbol{Z}'][\boldsymbol{Y}']$ and $[\boldsymbol{Y}'][\boldsymbol{Z}']$ using $[\boldsymbol{T}_v]$ and $[\boldsymbol{T}_i]$ matrices [47]-[48]:

$$[\boldsymbol{\gamma}^2] = [\boldsymbol{T}_v]^{-1}([\boldsymbol{Z}'][\boldsymbol{Y}'])[\boldsymbol{T}_v] = [\boldsymbol{T}_i]^{-1}([\boldsymbol{Y}'][\boldsymbol{Z}'])[\boldsymbol{T}_i]$$

(1.13)

$$[\boldsymbol{Z}_C] = [\boldsymbol{Z}'][\boldsymbol{T}_i][\boldsymbol{\gamma}]^{-1}[\boldsymbol{T}_i]^{-1} \qquad [\boldsymbol{Y}_C] = [\boldsymbol{Y}'][\boldsymbol{T}_v][\boldsymbol{\gamma}]^{-1}[\boldsymbol{T}_v]^{-1}$$

(1.14)

Where $[\boldsymbol{T}_v]$ and $[\boldsymbol{T}_i]$ are formed by the eigenvectors of the product matrices $[\boldsymbol{Z}'][\boldsymbol{Y}']$ and $[\boldsymbol{Y}'][\boldsymbol{Z}']$ respectively. Based on chain-parameter matrix in (1.12) and the Thevenin equivalent models for source and load networks [48], vectors of voltages $[\boldsymbol{V}(0)]$, $[\boldsymbol{V}(L)]$ and currents $[\boldsymbol{I}(0)]$, $[\boldsymbol{I}(L)]$ at the terminals can be calculated. When the terminal voltages and currents are known, the voltages and currents at the interior nodes of wires in the MTL can be derived through the same procedure as for a two-wire transmission line. However, the voltage and current expressions in (1.11) will extend to $N$-dimensional vectors. The common-mode current, which is the main contributor to radiation, can be obtained through summing the currents of each wire of the MTL.

Two-wire transmission line or $(N+1)$-wire MTL models are based on transmission line theory. However, the limitations of these classical models need to be understood before utilization. Firstly, transmission line theory is based on an assumption: the electromagnetic field surrounding the guiding structure is of the TEM or quasi-TEM type; and the total current flowing through cross-section is equal to zero. When the cross-section dimensions of the guiding structure are much less than the smallest wavelength of the considered signal, the transverse electromagnetic field dominates the overall field and other modes of electromagnetic fields attenuate rapidly along the guiding structure [45]. Secondly, the current will produce antenna-mode radiation, particularly at high frequencies and when the line is strongly curved or bent. However, the classical transmission line theory does not consider the antenna-mode radiation losses [46]. Thirdly, real automotive cable bundles are more complex than the uniform transmission line models described above. Due to variations of the wire cross-section dimensions or the wire positions along the axis of a cable bundle, stochastic behavior of voltage and current waves could be observed [19]. This is

caused by changing per-unit-length parameters $L'$, $R'$, $C'$ and $G'$ in (1.4) and (1.5), which are functions of position and will turn the equations (1.2) and (1.3) into non-constant coefficient differential equations. Except for some very special cases [49], it is very difficult to solve these differential equations. One solution is to break the overall line into a set of discrete uniform sections characterized by chain-parameter matrices. However, this approximation neglects any interaction between each uniform section because of the fringing of the field at the junctions [48].

## 1.3.2  Radiation Models of Dipoles

Electric-dipole is applied in radiation modeling as the elementary radiator [50]-[51], as shown in Figure 1.10:
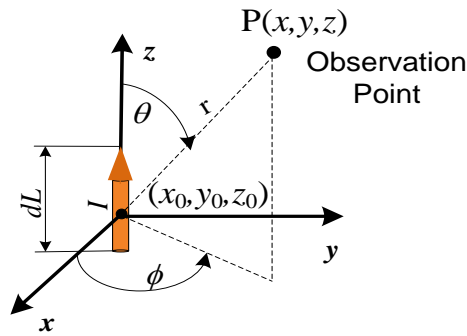


**Figure 1.10**  An electric dipole model in Cartesian coordinate

Electric dipole is based on the assumption of an infinitesimal short current path with current $I$ along a conductor of length $dL$. (1.15) – (1.20) are expressions for fields from a single electric dipole in Cartesian coordinates. Here $(x_0,\ y_0,\ z_0)$ is the coordination of dipole center, $\eta_0$ is the wave impedance in vacuum ($\eta_0 = \sqrt{\mu_0/\varepsilon_0}$), $\mu_0$ is the permeability of vacuum, $\varepsilon_0$ is the dielectric constant of vacuum, $\beta_0$ is the wave propagation phase constant in vacuum ($\beta_0 = \omega\sqrt{\mu_0\varepsilon_0}$), and $\omega$ is the angular frequency. $P(x,\ y,\ z)$ is the field observation point.

$$H_x = \frac{-IdL\cdot(y-y_0)}{4\pi r}\beta_0^2(j\frac{1}{\beta_0 r}+\frac{1}{\beta_0^2 r^2})e^{-j\beta_0 r} \tag{1.15}$$

$$H_y = \frac{IdL\cdot(x-x_0)}{4\pi r}\beta_0^2(j\frac{1}{\beta_0 r}+\frac{1}{\beta_0^2 r^2})e^{-j\beta_0 r} \tag{1.16}$$

$$H_z = 0 \tag{1.17}$$

$$E_x = \frac{IdL \cdot (z - z_0)(x - x_0)}{4\pi r^2} \eta_0 \beta_0^2 (j\frac{1}{\beta_0 r} + \frac{3}{\beta_0^2 r^2} - j\frac{3}{\beta_0^3 r^3})e^{-j\beta_0 r} \tag{1.18}$$

$$E_y = \frac{IdL \cdot (z - z_0)(y - y_0)}{4\pi r^2} \eta_0 \beta_0^2 (j\frac{1}{\beta_0 r} + \frac{3}{\beta_0^2 r^2} - j\frac{3}{\beta_0^3 r^3})e^{-j\beta_0 r} \tag{1.19}$$

$$
\begin{aligned}
E_z &= \frac{IdL \cdot (z - z_0)^2}{4\pi r^2} \eta_0 \beta_0^2 (j\frac{1}{\beta_0 r} + \frac{3}{\beta_0^2 r^2} - j\frac{3}{\beta_0^3 r^3})e^{-j\beta_0 r} \\
&\quad - \frac{IdL}{4\pi} \eta_0 \beta_0^2 (j\frac{1}{\beta_0 r} + \frac{1}{\beta_0^2 r^2} - j\frac{1}{\beta_0^3 r^3})e^{-j\beta_0 r}
\end{aligned}
\tag{1.20}
$$

Mirror theory can take ground reflections into account when the ground is an infinite perfect conductive plane. As illustrated in Figure 1.11, the mirror current for a horizontal current at height $h$ above ground is the inverse-directional current at height $h$ beneath the ground; while for a vertical current, the mirror current is the identical-directional current beneath the ground.
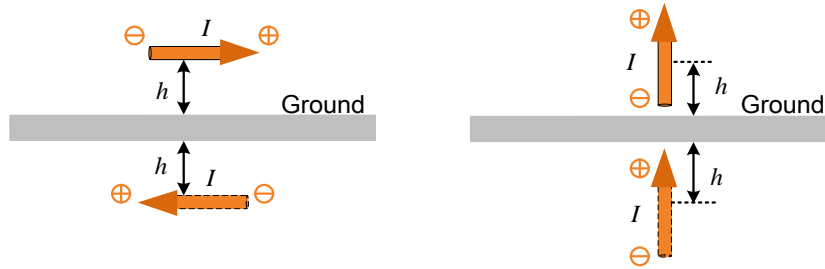


**Figure 1.11** Mirrors of currents above an infinite ground plane [30]

In the case of a cable bundle above a metallic table, the mirror theory is limited in accuracy due to the reflections from the table edges. An available analytic function (1.21) - (1.23) can approximately calculate the edge currents on a finite ground plate as shown in Figure 1.12 [52]. This eddy currents approximation is convenient to simplify the complexity of radiation model due to the finite ground plate.

A more general and accurate radiation model for a finite ground plate uses the physic optics approximation method, which is based on the equivalence theorem [53]. As shown in Figure 1.13, this method replaces the Perfect Electric Conductor (PEC) by equivalent surface currents. These equivalent surface currents on the truncated structure are assumed to be currents on the infinite structure but are restricted within the actual volume of the finite structure. Using this assumption, the equivalent surface current $J(s)$ is given by (1.23). Here $H^{\text{inf}}(s)$ means the magnetic field on the

infinite structure due to the radiation source, i.e. the radiated magnetic field from the radiator when the PEC ground is assumed to be infinite.
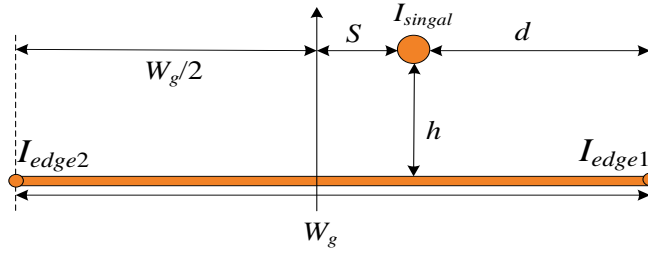


**Figure 1.12** Edge currents on a finite ground plane [52]

$$I_{edge1} = \frac{I_{signal}}{\pi} \left[ \frac{\pi}{2} - \arctan\left( \frac{w_g - 2S}{2h} \right) \right] \tag{1.21}$$

$$I_{edge2} = \frac{I_{signal}}{\pi} \left[ \frac{\pi}{2} - \arctan\left( \frac{w_g + 2S}{2h} \right) \right] \tag{1.22}$$
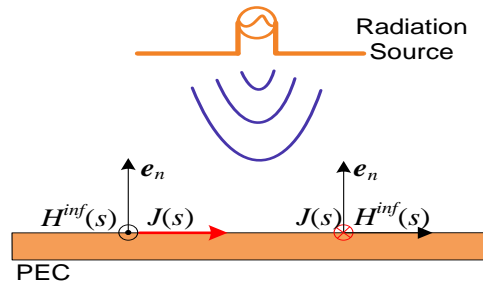


**Figure 1.13** Surface current representations for a finite ground plane [53]

$$\boldsymbol{J}(s) = \boldsymbol{e}_n \times \boldsymbol{H}^{\mathrm{inf}}(s) \tag{1.23}$$

## 1.3.3  Numeric Approaches

Due to the limitations of the models described above, more complex radiation structures require the usage of full-wave numeric simulation methods. Moment Method (MoM) is a famous frequency domain numeric method. The principle of MoM is to solve the Electric Field Integration Equation (EFIE) [54]-[55], which can describe the scattering or radiation problem of an arbitrary-shaped perfect conductor. In order to explain this numeric algorithm, we only consider a simple radiation problem from a thin wire. For calculating the spatial radiation from the wire, the accurate current distribution on the wire is needed. When the radius of the wire is neglected, the EFIF can be simplified as *pocklington's* integral equation [47]:

17

$$\int_{-L/2}^{L/2} I(z')(\frac{\partial^2}{\partial z^2} + \beta_0^2) \frac{e^{-j\beta_0\sqrt{(z-z')^2}}}{4\pi\sqrt{(z-z')^2}} dz' = j\omega\varepsilon_0 E_z(z) \quad (1.24)$$

Here $z$ represents any wire position and the current flowing direction; $E_z$ on the right side represents boundary conditions for the problem: $E_z = 0$ on the surface of the wire, $E_z = V_s \cdot \delta(z\text{-}z_s)$ at the source feed point $z_s$; $\beta_0$ is the propagation phase constant in the free space; $L$ is the wire length. The unknown current $I(z)$ at any wire position $z$ can be approximated by a finite set of complete basis functions $f_n(z)$ multiplying unknown current coefficients $I_n$:

$$I(z) = \sum_{n=1}^{N} I_n f_n(z) \quad (1.25)$$

Where $N$ is the number of basis function, and the unknown coefficients $I_n$ need to be determined. Substituting (1.25) into $I(z')$ in (1.24) will give:

$$\sum_{n=1}^{N} I_n G_n(z) \approx E_z(z) \quad (1.26)$$

$$G_n(z) = \int_{-L/2}^{L/2} f_n(z') \frac{1}{j\omega\varepsilon_0} (\frac{\partial^2}{\partial z^2} + \beta_0^2) \frac{e^{-j\beta_0\sqrt{(z-z')^2}}}{4\pi\sqrt{(z-z')^2}} dz' \quad (1.27)$$

In order to enforce the boundary condition, a set of orthogonal testing functions $w_m$ ($m = 1, 2,…, N$) are needed through forming the inner product on the both sides of (1.26):

$$\sum_{n=1}^{N} I_n \langle w_m, G_n(z)\rangle = \langle w_m, E_z(z)\rangle, \quad m=1, 2, … , N \quad (1.28)$$

Consequently, we have $N$ equations which can be expressed by a matrix form:

$$[\mathbf{Z}][\mathbf{I}] = [\mathbf{V}] \quad (1.29)$$

Each element of [**Z**] and [**V**] defined as $Z_{mn} = \langle w_m, G_n(z)\rangle$ and $V_m = \langle w_m, E_Z(z)\rangle$. Since the number of the basis function $f_n$ is equal to the number of the testing function $w_m$, the desired current coefficients $I_n$ of [**I**] can be calculated by the matrix inversion.

$$[\mathbf{I}] = [\mathbf{Z}]^{-1}[\mathbf{V}] \quad (1.30)$$

Typical basis functions for $f_n$ are rectangular, triangular, sinusoidal and *spline* functions. When the testing function of $w_m$ is defined to be same as basis function of $f_n$, this method is known as the Galerkin's method [55]. When the current coefficients $I_n$ are obtained, current $I(z)$ at any position $z$ on the thin wire can be calculated by (1.25). After all the currents on the thin wire are available, the electric field at any

spatial position can be calculated through the integration of each current element radiation [47]:

$$E_\theta = \frac{j\beta_0 Z_0}{4\pi} \int_{-L/2}^{L/2} \frac{I(z)sin\theta e^{-j\beta_0 r}}{r} dz \qquad (1.31)$$

Where $r$ and $\theta$ are the position functions related to current position $z$, $Z_0$ is wave impedance.

Other methods in frequency domain are the Finite Element Method (FEM), which is also a powerful and versatile numerical technique to solve different problems involving complex geometries and inhomogeneous media [56], and the Boundary Element Method (BEM) using discretization of boundary elements is often applied to the low frequency EMC problems [57]. Time domain methods are also widely applied in electromagnetic field simulation. Finite Integration Technique (FIT) [58] is a time domain method, which includes numerical spatial and time discretization schemes to solve transient electromagnetic field problems. FDTD [59] is another grid-based differential time-domain numerical modeling method. Unlike the mathematic discretization scheme of FIT and FDTD, Transmission-Line-Method (TLM) is a physical discretization approach using a continuous system of lumped elements to represent the field [60]. Due to real-world complexities of EMC problems, it is possible to combine different methods, which can embrace various advantages from different modeling approaches. For example, MoM/MTL is a hybrid approach to model the cable harness in a vehicle or other large-size configuration [61]-[62]. Additionally, a hybrid technique of TLM and Time-Domain Integral Equation (TDIE) has been developed to model a vehicle body shell and antenna [63]. However, it is still a challenge to apply highly accurate full-wave algorithms to model radiation from a cable configuration according to ALSE method. Complex cable bundle compositions, various disturbance sources, environmental influence factors, and test uncertainties have to be considered. Therefore, measurement based prediction models are more promising and preferable for practical applications.

## 1.4  Chapter Conclusion

This chapter has presented some important EMI disturbances in automotive systems, which can be classified in broadband (BB) and narrowband (NB) noise. Communication frequency bands in a vehicle environment interfered by this noise have been discussed. In order to protect on-board receiving antennas from EMI sources, regulations are issued which often refer to the standard CISPR 25. In this standard, ALSE test method or so-called antenna method is one of several methods proposed for EMI investigation. ALSE method specifies that special EMC antennas are applied to measure radiation from electrical or electronic components, which are

attached by a wire or cable bundle above a finite metal plate in an anechoic chamber. Theoretically, the active Rod antenna from 150 kHz to 30 MHz and the Biconical antenna from 30 MHz to 200 MHz are located in the near-field zone and the transition zone from the radiating structure, based on the radiation regions from an ideal short electric dipole. The log-periodic antenna used from 200 MHz to 1 GHz is located across the transition zone to the far-field zone. Different field characteristics in different zones have been discussed in this chapter. Compared with direct radiation estimation by the ASLE test method, simulation methods embrace unique advantages especially in an early-stage of a product development. In this chapter, two-wire and MTL models based on transmission line theory are introduced to simulate the current distribution. Also the limitations of transmission line theory are concluded. Furthermore, basic radiation models including electric dipole, mirror theory, edge currents, and surface current approximation model are presented. Additionally, this chapter has discussed typical full-wave numeric algorithms in frequency domain and time domain, which can model the complex radiating structures more accurately.

Direct ALSE test method can provide full-compliance radiation estimation, and show the best correlation to device radiation in a complete vehicle. Also it is widely accepted by standards. However, this method usually needs an expensive test site, which will increase the test cost in a new product development. Another tradeoff might be radiating peripheral systems superimposing the radiation from EUT to be measured in this method. Simulation approaches, as a low-cost scenario in the device radiation estimation, often gain the advantages of optimizing the device EMC performance and reducing the device time-to-market. However, only dependence on the simulation models, even the robust full-wave numeric algorithms, is not possible to obtain accurate results. Modeling the complex cable bundle, the EMI behaviors of various EUTs and Loads, and the real ALSE test environment is a challenge for simulation approaches. For these reasons, a compromise scenario is preferable. Since common-mode currents on cable bundles often dominate the radiations in the ALSE configuration, radiation prediction method with cable current measurements is a promising solution. Besides the cable currents can be easily measured, another advantage of this solution is completely free from the complex modeling of cable bundles, EUTs and loads. To achieve comparable radiation results with the ALSE test method, this current measurement solution have to consider three problems: accurate acquisition of cable common-mode current, flexible common-mode radiation model for a cable bundle, and available correction factors to real ALSE test environment. In next chapter the current acquisition methods and the phase defect problem will be firstly solved using current scan methods.

# 2 Current Scan Methods

Radiated emissions from cable bundles are strongly correlated to the common-mode current distribution on the bundle [6], [30], [47], [48], [64]. To describe the common-mode current measurement method, this chapter firstly introduces an equivalent circuit model using MTL mode theory. As the critical radiation source, amplitude and phase data of common-mode current are both indispensable to final field prediction. Therefore, current scan methods in frequency and time domain are proposed in this chapter, to acquire common-mode current spatial distribution on cable bundles. Phase information is difficult to obtain directly from frequency-domain current measurements. To solve this problem, a novel phase retrieval algorithm only based on the current amplitude is proposed. Compared with the retrieved phase in frequency-domain measurement, phase distribution can be directly obtained from time-domain current data using FFT. Another concern is the current acquisition limit due to the equipment sensitivity. This issue is also investigated considering the sensitivity of an oscilloscope in time-domain measurement and an EMI receiver in frequency-domain measurement.

## 2.1 Current Scanning System

For obtaining the common-mode currents at different positions along a cable bundle effectively, a measurement system is designed as shown in Figure 2.1, which mainly comprises of a current probe, a stepper motor, measurement equipment, and MATLAB based position control and data-processing program. In frequency-domain scanning, a spectrum analyzer or an EMI receiver is required to obtain current amplitude data. The deficient phase is retrieved based on the measured amplitude data. In the time-domain scanning, a multi-channel oscilloscope is required to get the time-domain current data and reference signal simultaneously.
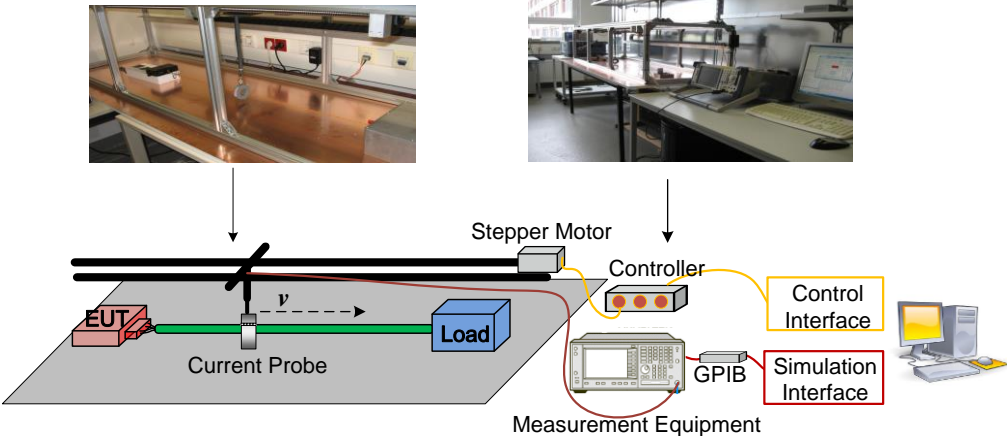


**Figure 2.1** Scanning system for the common-mode current measurements on a cable bundle

Scanning the current distribution can be seen as a special near-field scanning, but it is much simpler compared to the near-field scanning over a complex electronic PCB (Printed Circuit Board). Firstly, the current distribution along a cable bundle is one-dimensional spatially, rather than two- or three-dimensional as in near-field scanning. The common-mode current data can be acquired simply by scanning along the axial direction of the cable bundle. Secondly, less scan positions would be advantageous for the measurement efficiency. Since a typical cable set-up is 1.5 to 2 m long, the interval between two points less than 0.1 times of minimum wavelength in considered frequency range can achieve accurate current distribution, for example 3 cm interval with respect to 1 GHz. Additionally, the cable current is measured by the current probe of FCC FC-65 in this thesis, which has a flat transfer impedance of 0 dBΩ ($\pm$2 dB) over the frequency range from 1 MHz to 1 GHz. Depending on the transfer impedance, the desired cable current amplitude can be transferred to an output voltage at the current probe. This output voltage is actually induced by the alternating magnetic field from the cable current. In the current measurement on a cable bundle, only the common-mode current can be acquired due to the superposition of same directional magnetic fields; the differential-mode currents are zero due to the counteraction of opposite directional magnetic fields.

## 2.2  Common-Mode Current Model of Cable Bundles

According to mode theory for MTL [48], a MTL can be decoupled into a set of single transmission lines with different properties (propagation constant and characteristic impedance). Figure 1.9 shows a two-port network model with $N$ wires of length $L$ characterized by a per-unit-length impedance matrix $[Z']$ and an admittance matrix $[Y']$. If the current return path is included as depicted in Figure 1.8, the MTL forms an $(N+1)$-wire transmission line system. The actual line current $[I]$ and voltage $[V]$ can be expressed by modal quantities $[i_m]$ and $[v_m]$ by implementing the mode analysis method and using the decoupling transformations:

$$[I] = [T_i][i_m] \quad [V] = [T_v][v_m] \tag{2.1}$$

Where $[T_i]$ and $[T_v]$ are formed by the eigenvectors of the product matrices $[Y'][Z']$ and $[Z'][Y']$ defined in (1.13). These decoupling modal quantities travel along the cable bundle with different propagation constants $[\gamma_m]$ and characteristic impedances $[Z_{Cm}]$, which are in the form of diagonal matrices; and each element in these matrices corresponds to an Eigen-mode [47]. In these modes, the common-mode component mainly propagates between the cable bundle and return ground where air space has lower dielectric constant. And the propagation speed is close to the velocity of light due to the large distance of the cable bundle to the ground. Compared to common-

mode, other differential-mode mainly propagates among the wires in the cable bundle, of which velocities are reduced by the insulation material ($\varepsilon_r > 1$) [65].

If a cable bundle consists of tightly packed insulated wires, it is reasonable to neglect the contribution of differential-mode currents to the radiated emissions. Especially in configuration of ALSE method, where the antenna distance is far larger than the cross-sectional diameter of the cable bundle, therefore, the cable bundle can be simplified to a single wire with only a common-mode current flowing as shown in Figure 2.2 [66]. A similar common-mode model for a cable bundle is also presented in [67] to predict susceptibility of a cable bundle system.
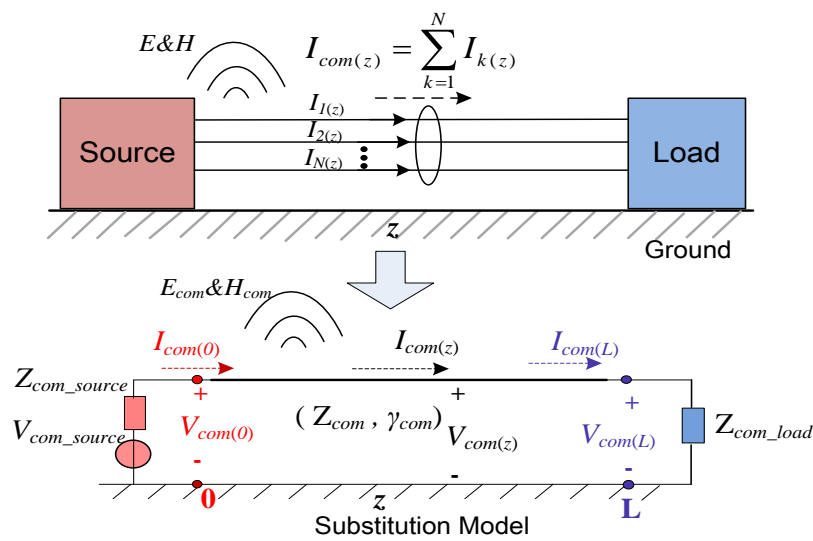


**Figure 2.2** A cable bundle and its substitution model for the common-mode current path

As showed in the simplified model for the common-mode current path above, this model can be further described by the common-mode quantities: transmission line parameters $Z_{com}$ and $\gamma_{com}$, source and load equivalent impedances $Z_{com\_source}$ and $Z_{com\_load}$, voltage source $V_{com\_source}$, and the current/voltage distribution $V_{com(z)}$ and $I_{com(z)}$. To obtain the common-mod current distribution, which is directly related to radiated emissions, different scenarios based on the simplified model shown above are possible. The work [68] calculates the current distribution on a simple wire structure based on transmission line model, in which $Z_{com}$ is calculated by analytic expressions and the terminal impedances ($Z_{com\_source}$ and $Z_{com\_load}$) are obtained through measurements. And then it uses the calculated currents to simulate the radiated emissions. The work [16] simulates the wire current and the resulted radiation from a DC/DC converter system through a FDTD model, in which current source $I_{com(0)}$ is impressed by the extern EMI current measurement from the converter. The work [69] simplifies the cable bundle by a single wire in complex system for the radiation calculation, in which EUT model is generated by the component measurements

23

($V_{com\_source}$ and $Z_{com\_source}$). In this thesis, direct measurement of the common-mode current distribution ($I_{com(z)}$) on a cable bundle is used to estimate the radiation emissions. Compared with other common-mode quantities, the common-mode current $I_{com(z)}$ is much easier to acquire. In addition, direct common-mode current measurements are completely free from the complex modeling of the cable bundle, EUTs and loads.

## 2.3  Common-Mode Current Measurements on Cable Bundles

For the radiation prediction common-mode current amplitude and phase are both indispensable. Time-domain current measurement using an oscilloscope and applying the FFT [70] can provide the necessary amplitude and phase. But due to limited dynamic range of time domain measurements and internal disturbance of oscilloscopes, frequency-domain measurement may be more accurate. For the commonly available frequency-domain measurement equipment, however, the phase information is often hard to acquire. Therefore, this section proposes different solutions for this deficient phase problem. Figure 2.3 depicts the basic configuration for a current scan in frequency and time domain. Current probe measures the common-mode currents at different positions $P_1$ to $P_N$ along the cable bundle. In the frequency domain only the current amplitude is acquired by an EMI receiver (R&S ESPI3). In the time domain the current and reference signal are both measured by a multi-channel oscilloscope (LeCroy Wavepro7200A). This reference signal provides the reference phase $\varphi_0$ for the desired phase distribution calculation. Also the phase shifts $\Delta\varphi_r$ and $\Delta\varphi_c$ due to the coaxial cables from probes connected to the oscilloscope must be considered.
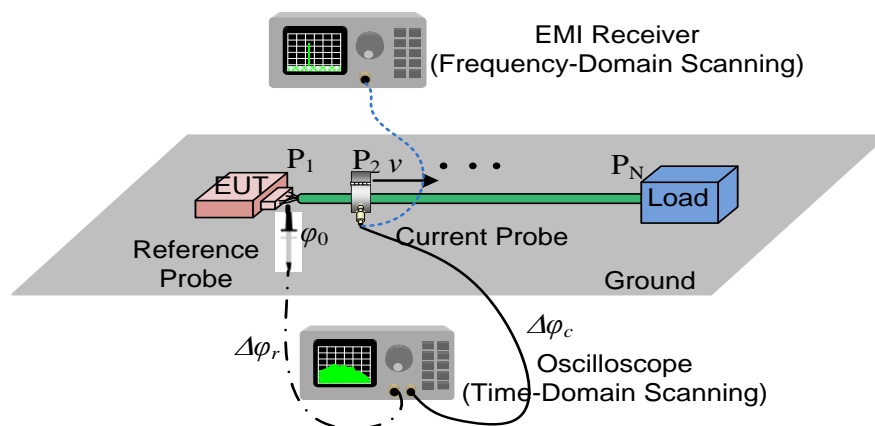


**Figure 2.3** Basic configuration of the current scan methods in frequency- and time-domain

24

## 2.3.1 Retrieval of the Current Phase Distribution in Frequency Domain

For obtaining phase information in frequency domain, direct phase measurement methods in frequency domain by a network analyzer and a spectrum analyzer have been applied to the near field scanning [51]. Phase measurement by a network analyzer requires a rigorous external reference signal to ensure the correct phase lock. The reference signal must have specific amplitudes and frequencies defined by the user. Moreover, it should not have large spurs and sidebands. Achieving these requirements is often difficult in a general EMI test, when the near-field distribution is characterized by wide frequency bands and various amplitudes. Phase measurement by a spectrum analyzer finds the phase information by doing several measurements with a defined phase shift, but the long measurement duration is not considered. Another method or so called phase-less technique is to retrieve the field phase distribution based on optimization algorithms, only from the knowledge of near-field amplitude data around antennas under test [71]. However, the near-field mathematic expressions from antennas are high-order and non-linear so that it is difficult to find optimization solutions. Moreover, multi-measurements are too time-consuming.

Compared with complex near-field scanning, common-mode current phase distribution on a cable bundle is much more regular. To avoid the difficulties of direct phase measurement, a novel phase retrieval algorithm is developed based on the equivalent common-mode circuit as depicted in Figure 2.2. According to transmission line theory, the common-mode current distribution can be expressed by functions of the propagation constant $\gamma_{com}$ and the load reflection factor $\Gamma_2$ [72]:

$$I_{com(z)} = \left( \frac{e^{\gamma_{com}(L-z)}}{1-\Gamma_2} \right) \left( 1 - \Gamma_2 e^{-2\gamma_{com}(L-z)} \right) I_{com(L)} \tag{2.2}$$

where $\Gamma_2$ and $\gamma_{com}$ can be also defined by transmission line parameters as:

$$\gamma_{com} = \alpha + j\beta \tag{2.3}$$

$$\Gamma_2 = \frac{Z_{com\_load} - Z_{com}}{Z_{com\_load} + Z_{com}} = A + jB \tag{2.4}$$

As depicted in Figure 2.2, the $Z_{com\_load}$ and $Z_{com}$ are the equivalent common-mode load impedance and characteristic impedance of the cable bundle, respectively. If the transmission line parameters $A$, $B$, $\alpha$, and $\beta$ are found, the phase can be determined by (2.2). As an inverse problem, these unknown parameters have to be searched only based on the current amplitude measurements through appropriate fitting algorithms.

1)  Objective function about the phase retrieval problem

To search transmission line parameters, we define (2.2) with a quadratic normalized function:

$$F(z) = \left| \frac{I_{com(z)}}{I_{com(L)}} \right|^2 = \left| \left( \frac{e^{\gamma_{com}(L-z)}}{1-\Gamma_2} \right) \left( 1 - \Gamma_2 e^{-2\gamma_{com}(L-z)} \right) \right|^2 \tag{2.5}$$

Substituting (2.3) and (2.4) into (2.5), $F(z)$ can also be expressed with respect to $A$, $B$, $\alpha$, and $\beta$:

$$F(z) = \frac{e^{-2\alpha(z-L)}}{(1-A)^2+B^2} \left\{ \left[ 1 - Ae^{2\alpha(z-L)}\cos(2(z-L)\beta) + Be^{2\alpha(z-L)}\sin(2(z-L)\beta) \right]^2 \right. $$
$$\left. + \left[ Ae^{2\alpha(z-L)}\sin(2(z-L)\beta) + Be^{2\alpha(x-L)}\cos(2(z-L)\beta) \right]^2 \right\} \tag{2.6}$$

$F(z)$ is a nonlinear function, where the position coordinate along the cable bundle $z$ is known, but transmission line parameters $A$, $B$, $\alpha$, and $\beta$ have to be found. From measured amplitude data at scanning points, more equations than unknowns $A$, $B$, $\alpha$, and $\beta$ can be formulated. For this over-determined equation system, a feasible solution set has to be found. Therefore, this system requires a suitable optimization method to search for the best approximating solution for the unknowns. In this work, the *Trust-Region-Reflective* iterative algorithm (TRR) [73] is employed. This algorithm is able to find transmission line parameters $A$, $B$, $\alpha$, and $\beta$ so that the sum of squares of the deviation $S$ is minimum, for a given set of measurements points $F_{meas}(z)$. The objective function $S$ can be expressed by:

$$S = min \left\| F(A, B, \alpha, \beta, z) - F_{meas}(z) \right\|_2^2$$
$$= \sum_{i=0}^{m} [F(A, B, \alpha, \beta, z_i) - F_{meas}(z_i)]^2 \tag{2.7}$$

2)  Boundary condition for parameters in the optimization algorithm

In order to find the optimization parameters $A$, $B$, $\alpha$, and $\beta$ with high reliability, integrating appropriate boundary conditions into the TRR algorithm is necessary. The characteristic impedance $Z_{com}$, which is mainly determined by the common-mode per-unit-length capacitance and inductance of the cable bundle, can be approximated by a real constant at each frequency point. Therefore, the load reflection coefficient $\Gamma_2$ in (2.4) can be rewritten as:

$$\Gamma_2 = \frac{Z_{com\_load} - Z_{com}}{Z_{com\_load} + Z_{com}} = \frac{[\mathrm{Re}(Z_{com\_load}) - Z_{com}] + j[Imag(Z_{com\_load})]}{[\mathrm{Re}(Z_{com\_load}) + Z_{com}] + j[Imag(Z_{com\_load})]}$$
$$= A + jB \tag{2.8}$$

Due to the amplitude of $\Gamma_2$ bounded in [-1, 1], the boundaries of its real and imaginary parts are given by:

$$limA = [-1,1]$$
$$limB = [-1,1]$$
(2.9)

Further the propagation constant $\gamma_{com}$ in (2.3) can also be approximately expressed by [74]:

$$\gamma_{com} = \alpha + j\beta = \frac{R_{DC}}{2Z_{com}} + j\frac{\omega}{v_{com}}$$
(2.10)

Where $\omega$ is the angular frequency, $v_{com}$ is the common-mode propagation velocity, and $R_{DC}$ is the equivalent DC (Direct Current) resistance of the cable bundle. An accurate resistance formulation should consider the skin effect, however, the attenuation has nearly no influence on the phase accuracy but introduces additional computation time. For this reason, more accurate formulations for attenuation are not taken into account here. Therefore, the boundaries for $\gamma_{com}$ can be derived as follows:

$$lim\alpha = [0,0.1]$$
$$lim\beta = [\frac{\omega}{v_0/\sqrt{\varepsilon_r}},\frac{\omega}{v_0}], \ \omega = 2\pi f$$
(2.11)

The upper boundary of $\alpha$ is reasonable, because in typical applications $R_{DC}$ is usually much smaller than $Z_{com}$. $v_{com}$ is bounded by the velocity of light in vacuum $v_0$ and in the the commonly used cable insulation material with $\varepsilon_r \approx 2.3$, i.e. $v_{com\text{-}min} = v_0/\sqrt{\varepsilon_r}$ .

   3) Initial parameters $A_0$, $B_0$, $\alpha_0$, and $\beta_0$

   A key problem in an optimization algorithm is the local minimum phenomenon, i.e. a point where the function value is smaller than or equal to the values at nearby points but greater than more distant points. However, a reliable solution for an inverse problem needs to find for a reliable global minimum point. The initial parameter point ($A_0$, $B_0$, $\alpha_0$, and $\beta_0$) plays a significant role in finding the minimum parameters. A multi-start point algorithm [73] can be used, which generates random initial points in boundaries and solves the objective function at each initial point. Finally, it compares local minimum values at different initial points, to achieve the most promising parameters for a global minimum point search. Compared with general TRR, it will cost more computation time due to more iterative loops.

   After the parameters $A$, $B$, $\alpha$, and $\beta$ at each frequency are found, the relative phase distribution of the common-mode current on the cable bundle can be retrieved using ($I_{com}(L)$ gives reference phase here):

$$phase\left[\frac{I_{com(x)}}{I_{com(L)}}\right] = phase\left[\left(\frac{e^{\gamma_{com}(L-x)}}{1-\Gamma_2}\right)\left(1-\Gamma_2 e^{-2\gamma_{com}(L-x)}\right)\right] \tag{2.12}$$

If the common-mode characteristic impedance $Z_{com}$ is known, the equivalent load impedance $Z_{com\_load}$ can be obtained by (2.13), in which the load reflection coefficient $\Gamma_2$ is calculated from the fitting algorithm. Another solution is according to the maximum and minimal positions of common-mode current amplitude distribution [75]. Equation (2.14) can directly calculate the load impedance by features of the current amplitude distribution. In this equation, $m$ is the ratio of the amplitude minimum to the maximum. $L_{min}$ is the distance of the nearest amplitude minimum to the end of cable bundle.

$$Z_{com\_load} = Z_{com}\frac{1+\Gamma_2}{1-\Gamma_2} \tag{2.13}$$

$$Z_{com\_load} = Z_{com}\frac{1/m - j\tan(\beta L_{min})}{1 - j(1/m)\tan(\beta L_{min})}, m = \frac{\min(I_{com}(z))}{\max(I_{com}(z))} \tag{2.14}$$

## 2.3.2 Reconstruction of the Current Phase Distribution in Time Domain

Current scanned by an oscilloscope in the time domain can directly provide the desired amplitude and phase data based on FFT. A reference signal is needed to calculate the relative phase distribution at different cable positions. Current at a fixed cable position or a fixed external signal can be defined as the reference signal. For example the voltage signal at the cable start position acts as the reference signal, as shown in Figure 2.3. It is connected to the first channel of oscilloscope. The current probe is connected to the second channel for scanning the currents at different cable positions. The relative phase can be calculated according to (2.15). Here $\varphi_N$ is the phase at the $N$th position, $\varphi_0$ is the phase from the reference signal, $\Delta\varphi_r$ and $\Delta\varphi_C$ are the phase shifts caused by the coaxial cables from the reference probe and current probe connected to the oscilloscope, respectively. The coaxial cable phase shifts can be removed by normalizing the phase at each position to the cable end position according to (2.16).

$$\begin{aligned} P_1 &: [\varphi_1 + \Delta\varphi_c] - [\varphi_0 + \Delta\varphi_r] = [\varphi_1 - \varphi_0] + [\Delta\varphi_c - \Delta\varphi_r] \\ P_2 &: [\varphi_2 + \Delta\varphi_c] - [\varphi_0 + \Delta\varphi_r] = [\varphi_2 - \varphi_0] + [\Delta\varphi_c - \Delta\varphi_r] \\ &\quad\quad\quad\vdots \quad\quad\quad\quad\quad\quad\quad\quad\quad\quad\quad \vdots \\ P_N &: [\varphi_N + \Delta\varphi_c] - [\varphi_0 + \Delta\varphi_r] = [\varphi_N - \varphi_0] + [\Delta\varphi_c - \Delta\varphi_r] \end{aligned} \tag{2.15}$$

$$P_1 - P_N : \varphi_1' = [\varphi_1 - \varphi_N]$$
$$P_2 - P_N : \varphi_2' = [\varphi_2 - \varphi_N]$$
$$\vdots$$
$$P_N - P_N : \varphi_N' = 0$$

(2.16)

### 2.3.3 Accuracy of Current Scan Methods

In order to verify the current scan methods in the frequency- and time-domain, a 1.5 m single wire terminated with a 50 Ω load is driven by a Vector Network Analyzer (VNA, Agilent E5071B). Height of the wire above the ground plane is 5 cm. The wire characteristic impedance is about $Z_{com}$ = 270 Ω, and the propagation velocity ($2\pi f/\beta$) is about $v_{com}$ = 2.91·10$^8$ m/s [25]. According to the known transmission line parameters, a transmission line model for this wire can be established [47] to simulate the current distribution. Additionally, the measurement is also implemented. The current scanning is performed each 6 cm along the wire. The measured current phase from the VNA is used to verify the retrieved phase based on the amplitude measurements. For the time-domain investigation, this wire is driven by a battery supplied signal generator (Signal-Forge 1020), with a sinusoid signal of 10 dBm power at frequencies under consideration. The voltage at the wire start position provides the reference phase for the measurement of current phase distribution. Figure 2.4 depicts the basic verification configuration：
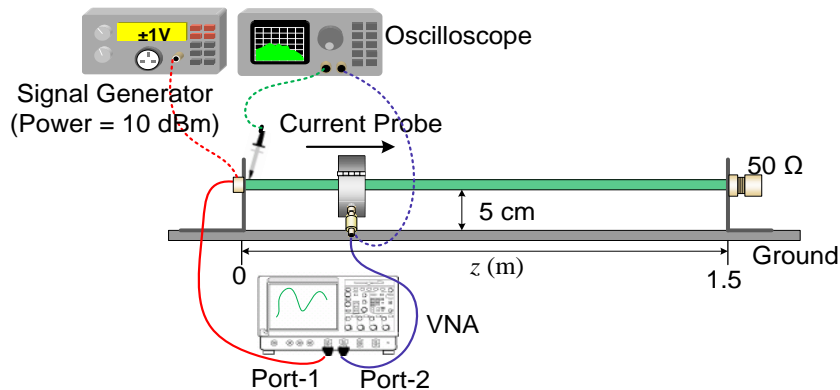


**Figure 2.4** Current measurements by a vector network analyzer or an oscilloscope

1) Simulation based robustness investigation

When the common-mode transmission line parameters $A$, $B$, $\alpha$, and $\beta$ of the cable bundle are found, the phase distribution can be retrieved according to (2.12). In order to validate this phase retrieval algorithm, the wire mentioned above is simulated first. Resistance loss is ignored ($\alpha \approx 0$). It is driven by a voltage source $V_S$ =

29

1 V with 50 Ω impedance from 1 MHz to 1 GHz. Current amplitude and phase distributions on the entire wire can be calculated using [47]:

$$I(z) = \frac{e^{-j\beta z} - \Gamma_2 e^{j\beta(z-2L)}}{2Z_{com}(1-\Gamma_1\Gamma_2 e^{-j2\beta L})} \left[(1-\Gamma_1)V_S\right] \qquad (2.17)$$

$\Gamma_1$ and $\Gamma_2$ are the source and load reflection factors, respectively. Based on the calculated current amplitude data, the retrieved current distribution using the proposed retrieval algorithm nearly coincides to the results from transmission line theory, as shown in Figure 2.5. Additionally, the transmission parameters are retrieved successfully above 25 MHz, as shown in Figure 2.6. The load impedance $Z_{com\_load}$ can be calculated according to the retrieved $\Gamma_2$ in (2.13), or the relationships of current amplitude maximum and minimum defined in (2.14). But it is note that the wire characteristic impedance $Z_{com}$ must be known in both two equations.
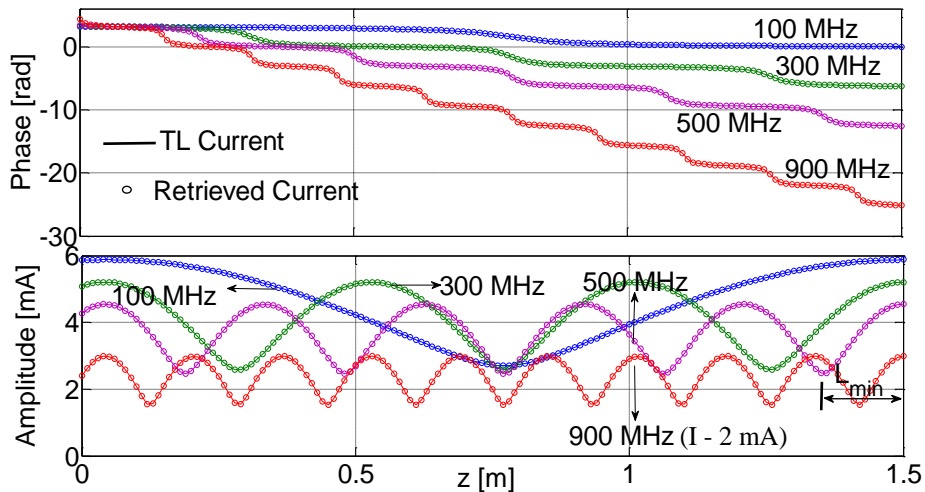


**Figure 2.5** Retrieved current distribution based on the current amplitude data from transmission line (TL) theory; $L_{min}$ means the current nearest minimum to the wire end which is used by (2.14)
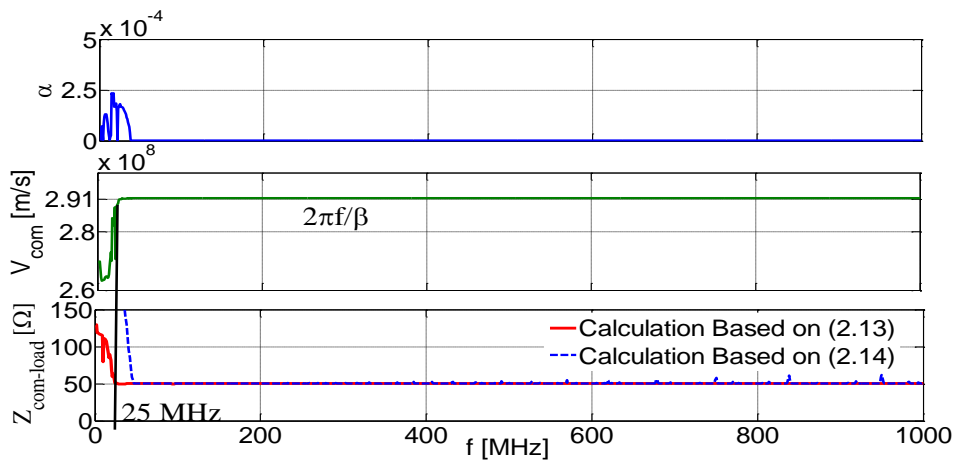


**Figure 2.6** Retrieved transmission line parameters based on the current amplitude data from transmission line theory

2)  Measurement based robustness investigation

According to (2.5), the normalized quadratic function $\boldsymbol{F}(z)$ of the current amplitude distribution from the measurement, the retrieved amplitude and the FFT at 100 MHz, 500 MHz and 900 MHz are compared in Figure 2.7. It can be seen that there is a good match of the amplitude distribution; but the curves about current distributions at 900 MHz from the retrieved or the FFT shows certain deviations. Both of the phase distributions, which are retrieved in frequency domain and reconstructed by FFT from time domain data, nearly coincide to the measured phase from the VNA at different frequencies, as shown in Figure 2.8.
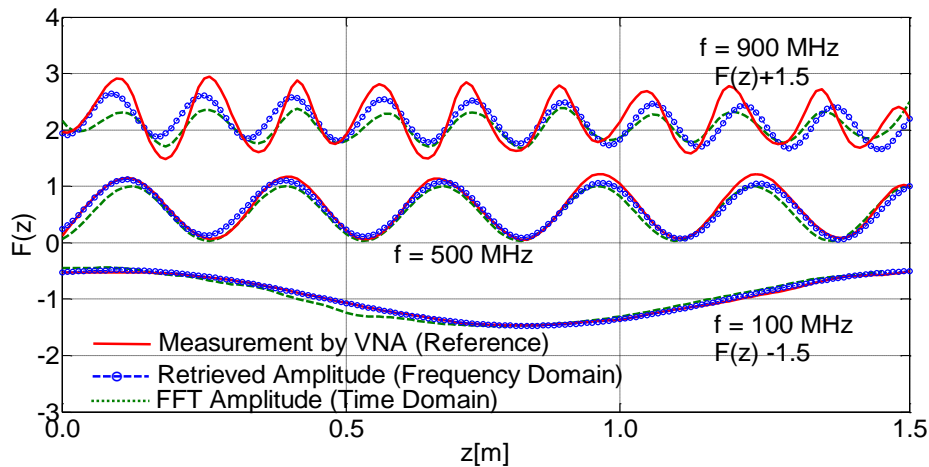


**Figure 2.7** Normalized quadratic distributions of current amplitude along the wire at 100 MHz, 500 MHz and 900 MHz from the VNA measurement, the retrieved in frequency domain and the FFT in time domain
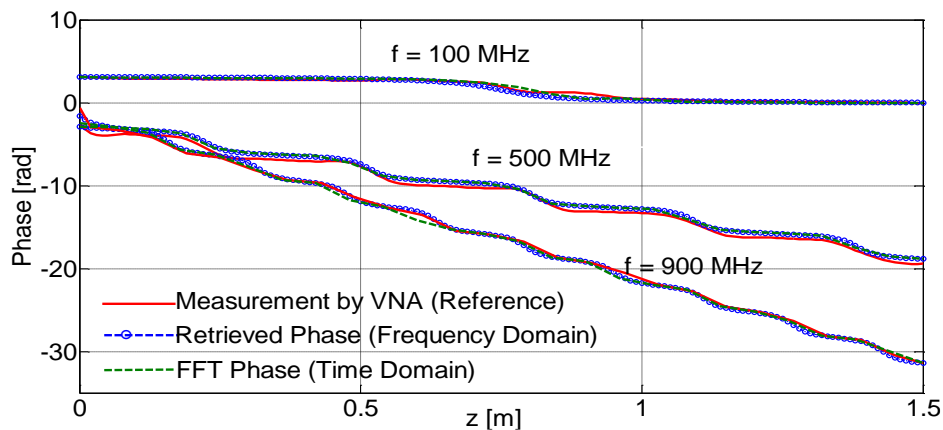


**Figure 2.8** Current phase distributions along the wire at 100 MHz, 500 MHz and 900 MHz from the VNA measurement, the retrieved in frequency domain and the FFT in time domain

Current phase distribution in the frequency domain is calculated according to (2.12), based on the retrieved transmission line parameters $A$, $B$, $\alpha$, and $\beta$. Figure 2.9 compares these retrieved parameters to the reference values. Some deviations can be observed. In the simulation verification above, the accurate retrieved transmission

31

line parameters mainly are caused by the current amplitude data from (2.17), which strictly complies with transmission line theory. However, in the current measurements on the wire, the retrieved transmission line parameters are more mathematical fitting parameters, and they might not reflect the physical case. Due to the existence of measurement errors, TRR iterative algorithm often force the parameters $A$, $B$, $\alpha$, and $\beta$ to reach the condition of objective function defined in (2.7), at the expense of sacrificing their physical meanings. However the assumption, that the common-mode current on the cable bundle complies with transmission line theory, often gives reliable results for the current phase distribution as shown in Figure 2.8. Additionally, load impedance $Z_{com\_load}$ calculated from (2.14), which describes the relationship of measured current maximum and minimum relationship, also shows deviations, especially at high frequencies as in Figure 2.9. Similarly with the retrieved parameters, the calculation accuracy by (2.14) also depends on the current amplitude distribution, which should strictly comply with transmission line theory. However, measurement errors at amplitude maximums and minimums, and the position deviations of $L_{min}$ can both lead to calculation inaccuracy.
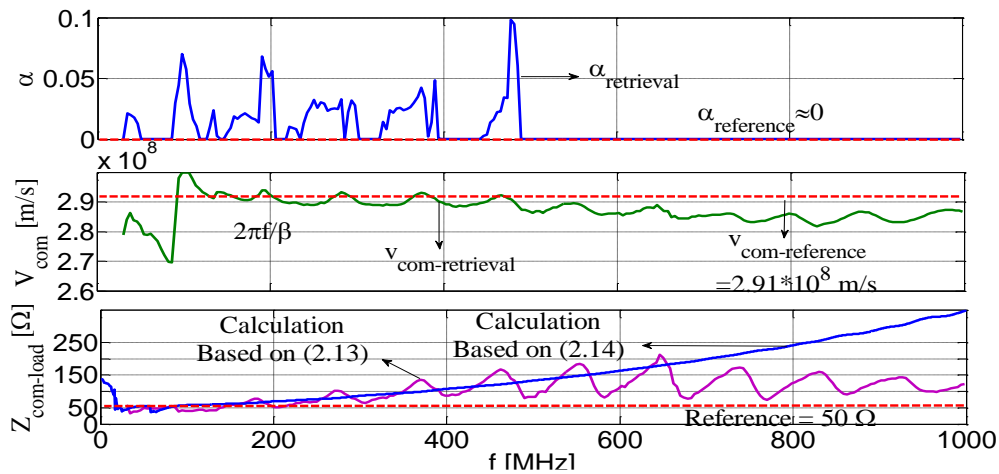


**Figure 2.9** Retrieved transmission line parameters based on the current amplitude data from the EMI receiver measurements

# 2.4  Dynamic Range of Current Scan Methods

Accurate current amplitude and phase distributions are both necessary to guarantee the success in final radiation prediction. In real EMC test set-up, the common-mode currents on the cable bundle can be very weak to cause the capture problem by the measurement equipment, but it may result in a serious radiated emission. Therefore, this section investigates the measurable current limits due to the sensitivity from the EMI receiver or oscilloscope. Furthermore, some factors influencing the current acquisition accuracy during the scanning procedure will be discussed.

## 2.4.1 Measurement Limits Due to Equipment Sensitivities

In the frequency-domain scan method, the accuracy of current amplitude measurements is critical to the retrieved phase and the final radiation prediction. Figure 2.10 shows the minimum measurable amplitude limits and noises floor from the referred EMI receiver with typical settings. A sinusoid voltage wave at 100 MHz is used as an example here. When the receiver chooses average detector, the band width (BW) is 9 KHz, 0 dB RF-attenuation, and 5 ms measure time (MT), the noise floor can reach -13 dBμV and the measurable amplitude limit can reach -10 dBμV. The corresponding current amplitude limit can be calculated from the voltage amplitude limit (dB) minus the transfer impedance (dB) of the current probe. The current measurement system in Figure 2.4 is used to investigate the influence of a weak signal on the current scan accuracy. The transfer impedance of the used current probe is 0 dBΩ. EMI receiver is applied to measure the current amplitude, and then the current phase is retrieved by the proposed algorithm. Settings of the receiver with average detector are 9 KHz BW, 5ms MT, 0 dB attenuation. Figure 2.11 shows the measured current amplitude and the retrieved phase distribution on the wire at 100 MHz. Curve denoted with TL Model means the simulation result from transmission line model. When the source power is reduced to -80 dBm, the current data at positions between 0.5 m and 1 m are lost due to the amplitude below -10 dBμA limit. Based on the incomplete current amplitude information, corresponding phase distribution cannot be computed.

In the time-domain scan method, current amplitude and phase are both transformed from the measured time-domain data via FFT. To investigate the limits due to the sensitivity of the referred oscilloscope, a sinusoid voltage wave at 100 MHz is also used as an example here. The total oscilloscope sample time is 550 μs, and the sampling interval is 0.5 ns. As can be seen in Figure 2.12, the single sweep by the oscilloscope presents a higher noise floor (18 dBμV) compared with the EMI receiver (-13 dBμV). Additionally, the minimum measurable amplitude limit is about 25 dBμV. Averaged sweeps can reduce the noise floor significantly in the time domain. Noise floor of 200 averaged sweeps by oscilloscope can reach -6 dBμV. However, due to the vertical sensitivity limits of a referred 8-bit oscilloscope ($2/2^8$ mV or 17.9 dBμV), only 20 dBμV steps can be recorded successfully. The wire in Figure 2.4 is again fed with different power levels to investigate the influence of weak signals on the current acquisition in time domain. Figure 2.13 shows current amplitude and phase distribution measured by the oscilloscope with a single sweep. When the power is reduced to -36 dBm, the measured current amplitude and the phase distribution shows instability, although the amplitude at most positions are higher than the sensitivity limit. At amplitudes higher than 30.6 dBμA (12.6 dB higher than the noise floor), stable amplitude and phase acquisition performance is

achieved. Compared with single sweep, averaging the sweeps by the oscilloscope can extend the measurable amplitude limit down to 20 dBµA, as shown in Figure 2.14.
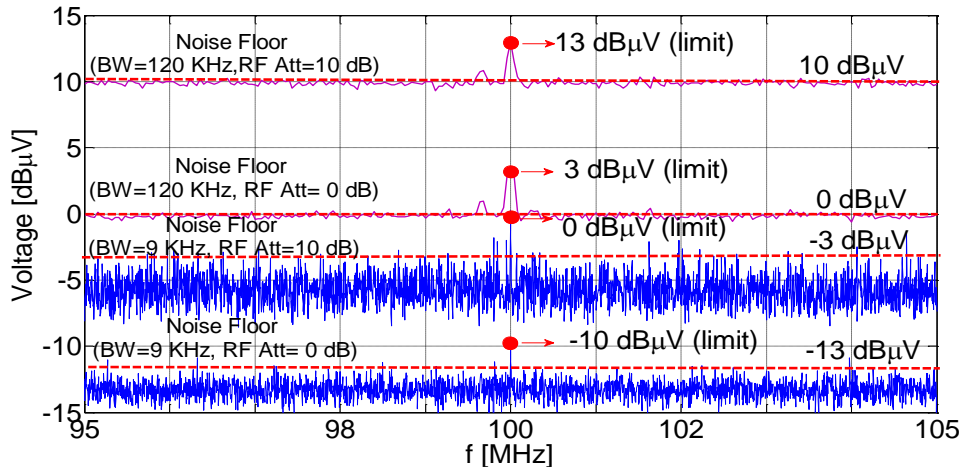


**Figure 2.10** Measurable amplitude limit and noise floor at 100 MHz from the EMI receiver
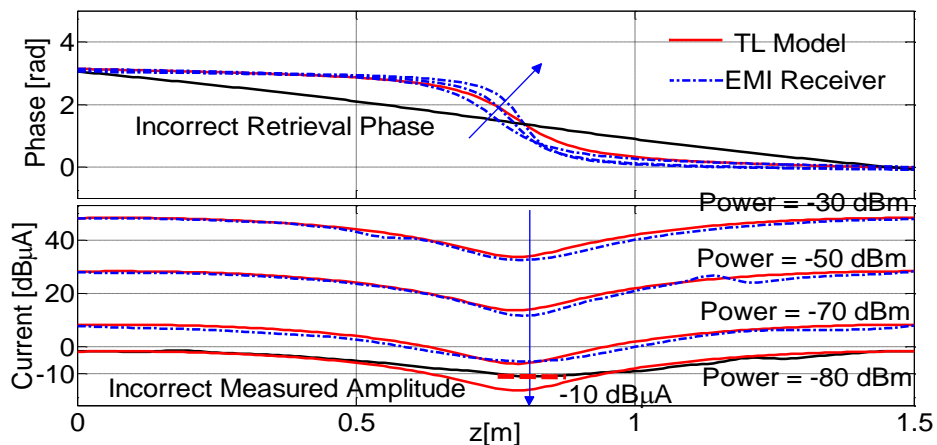


**Figure 2.11** Measured current amplitude and retrieved phase distribution at 100 MHz from the EMI receiver when the wire is fed by different power levels
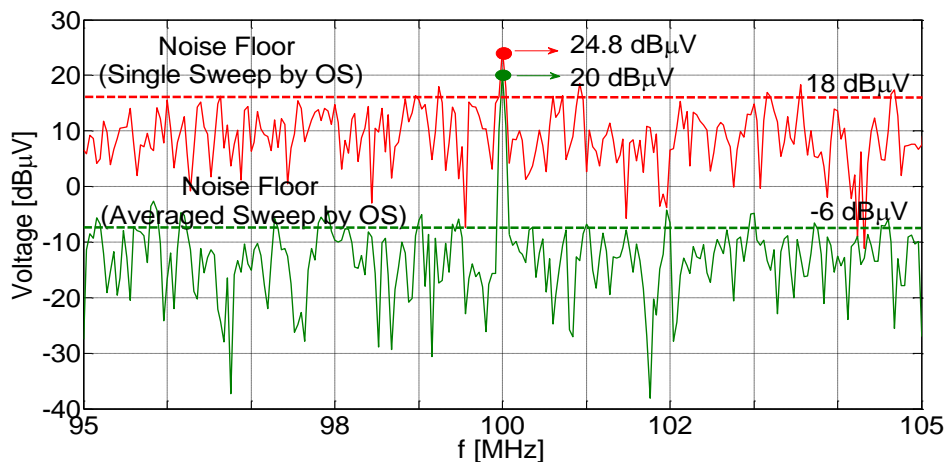


**Figure 2.12** Measurable amplitude limit and noise floor at 100 MHz from the oscilloscope (OS) with single sweep and averaged sweep
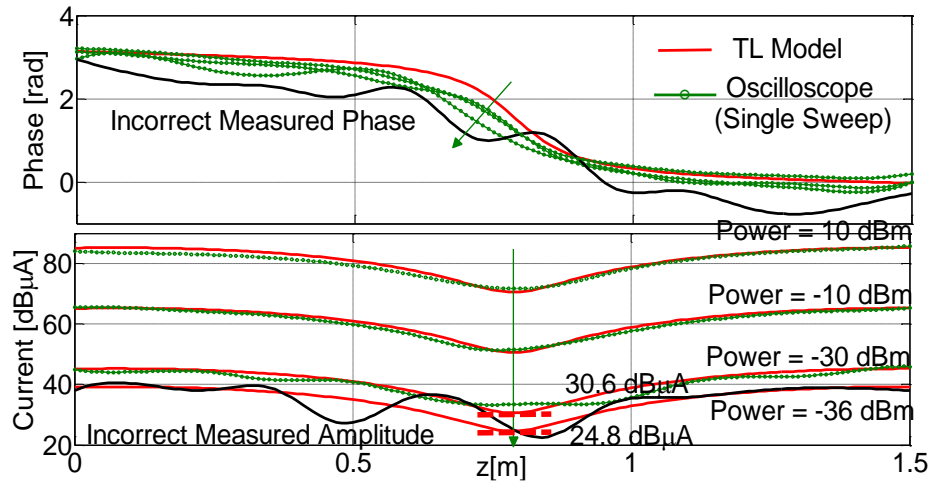
34

**Figure 2.13** Measured current amplitude and phase distribution at 100 MHz from the oscilloscope with single sweep when the wire is fed by different power levels
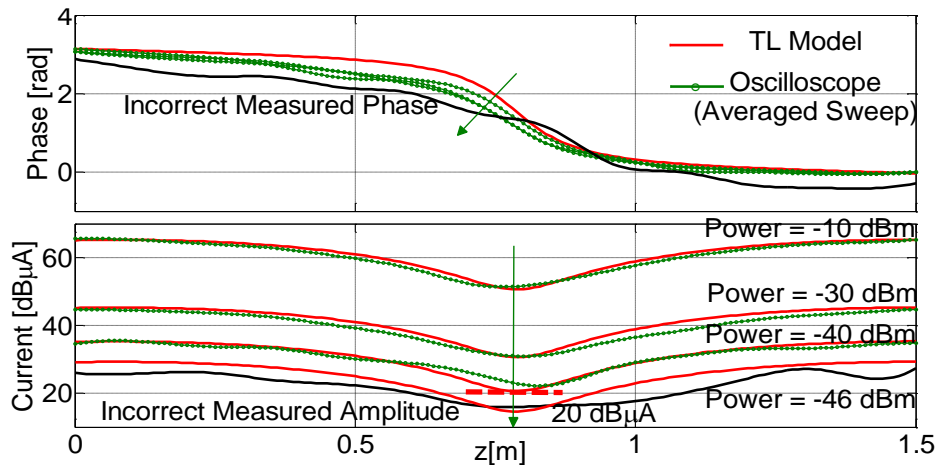


**Figure 2.14** Measured current amplitude and phase distribution at 100 MHz from the oscilloscope with averaged sweep when the cable is fed by different power levels

Triggering signal is also critical in the whole current scanning process, to guarantee a stable triggering of the oscilloscope. A reference signal with higher amplitude is often used to trigger the oscilloscope. When the wire is fed by a power of -40 dBm, the simulated current (TL model) at the wire center is about 20.6 dBµA. However, when the trigger voltage is 50 dBµV recorded by the first channel of the oscilloscope, the weak current recorded by the oscilloscope second channel is nearly lost. When the trigger voltage level rises to 60 dBµV, the recorded current amplitude can reach 17.8 dBµA, as shown in Figure 2.15. In practice, the trigger signal might be too weak to the triggering failure. Therefore, a direct voltage measurement close to the clock on the PCB under test might be necessary (only one clock signal assumed here) for the stable trigger events.
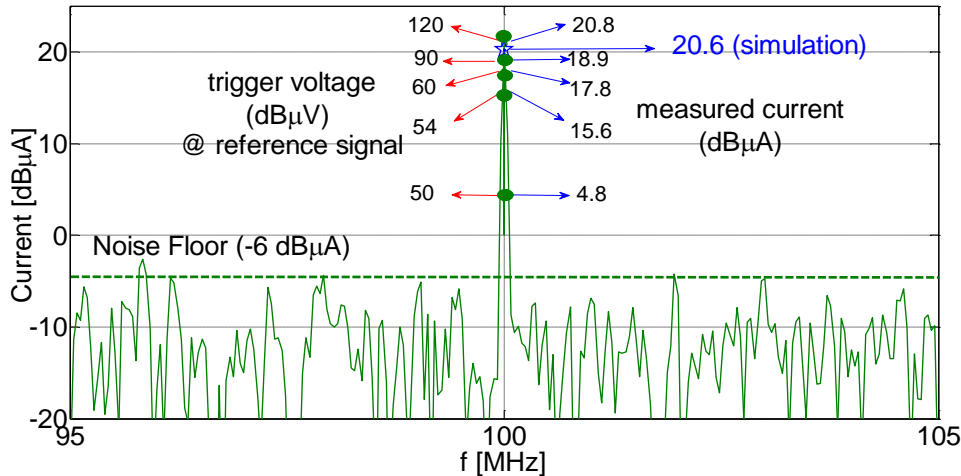
**Figure 2.15** Measured current amplitude from the oscilloscope with averaged sweeps when the trigger signal with different voltage levels

The minimum measurable current limits discussed above are caused by the sensitivity of receiving equipments. Also, the measureable current limit is dependent upon the sensitivity of the current probe, which is a function of transfer impedance. The transfer impedance is defined as the ratio of probe output voltage to the current on the wire under test. Therefore, the current probe with high transfer impedance can improve the current measurement limit effectively. Additionally, a low noise pre-amplifier can also improve the current measurement limit.

## 2.4.2 Further Considerations in Current Scan Processes

To acquire the current data as accurate as possible, other possible influencing factors in the process shall be considered. Firstly, some common factors in both frequency- and time- domain current scan methods need to be considered:

*a*) Choice of a proper RF current probe: When choosing a current probe, several electrical and mechanical features should be considered including operation bandwidth, transfer impedance, sensitivity, and physical dimensions.

*b*) Scanning position error: The designed scan system as shown in Figure 2.1 can improve the scanning efficiency and avoid human errors. However, the current probe thickness (for example 1.7 cm for the used FC-65 current probe) might induce position error at high frequencies.

c) Loss of connected coaxial cable: Characterization of the coaxial cable and correction of the measured current data are needed.

*d*) Random ambient noise: Usually it is necessary to pre-scan the system under test without a driven source to detect potential ambient noise.

Secondly, there are some considerations when implementing the current scan method in the frequency domain by a spectrum analyzer or EMI receiver:

a) Selection of detectors when using an EMI receiver: When the predicted radiated emissions based on current measurements are compared with real ALSE test results, the detector type (for example the "Average" or "Peak") in the current measurements should be the same as the type in antenna measurements.

b) Selection of trace functions when using a spectrum analyzer: In order to ensure the capture of all expected events, we can enable "Max hold" function to perform a minimum of three sweeps while the EUT operating cycle executes [9].

c) Minimum measureable limit: Before the scanning, figure out the minimum measureable amplitude limit and noise floor from the equipments is necessary.

Thirdly, in the implementation of current scan method in the time domain by an oscilloscope, the distortions of the spectrum due to FFT should be concerned [76]:

a) Edge discontinuities: If the signal contains discontinuities at its edges, pseudo-frequencies will appear in the spectral domain, which will distort the real spectrum.

b) Picket fence effect: When the clock or its harmonic frequency is halfway between two discrete frequencies of FFT, the computed amplitude in the spectrum can be several decibels lower.

c) FFT-windowing: Appropriate window function can improve the filter response shape, noise bandwidth as well as side lobe levels, for example Gaussian window-function.

d) Minimum measureable limit: Average sweep can reduce noise floor effectively to improve measurement dynamic. However, it is also limited by amplitude sensitivity of the oscilloscope. Moreover non-stationary components may be submerged with averaged sweeping [77].

## 2.5  Chapter Conclusion

Common-mode current measurement on a cable bundle is a primary and critical step for the radiation prediction. For this purpose, two current scan methods have been developed based on the common-mode model of a cable bundle. One method is to scan common-mode current amplitude data in the frequency domain using an EMI receiver or a spectrum analyzer. The needed phase information is retrieved by an optimization algorithm, only based on the amplitude information. TRR algorithm is used as the optimization algorithm to search for the transmission line parameters, and then required phase distribution can be calculated based on transmission line model. The frequency-domain scan method has great measurement dynamics, for example the noise floor of -13 dBμV and the measureable amplitude limit of -10 dBμV with respect to the referenced EMI receiver (R&S ESPI3), of which the setting is 9 kHz BW and 5 ms MT, and 0 dB RF-attenuation. The time-domain method acquires the amplitude and phase information by an oscilloscope via FFT. In this

scan method, an additional signal is required to provide a reference phase. However, this method suffers from lower measurement dynamics, for example the noise floor of 18 dBµV and the measurable amplitude limit of 25 dBµV for a typical setting of the oscilloscope under investigation (LeCroy Wavepro7200A). Averaging the time-domain sweeps can reduce noise floor effectively down to -6 dBµV, but the measurable amplitude limit is about 20 dBµV due to the sensitivity limit of the oscilloscope. A sufficient trigger voltage level is another demand to ensure the reliable data acquisition.

The processes of current acquisition by the two methods can be summarized by Figure 2.16. After acquiring the common-mode current amplitude and phase distribution on a cable bundle, appropriate and flexible radiation models for the cable bundle are required for the final field prediction. Therefore, next chapter deals with the choice of appropriate radiation models for cable bundles.
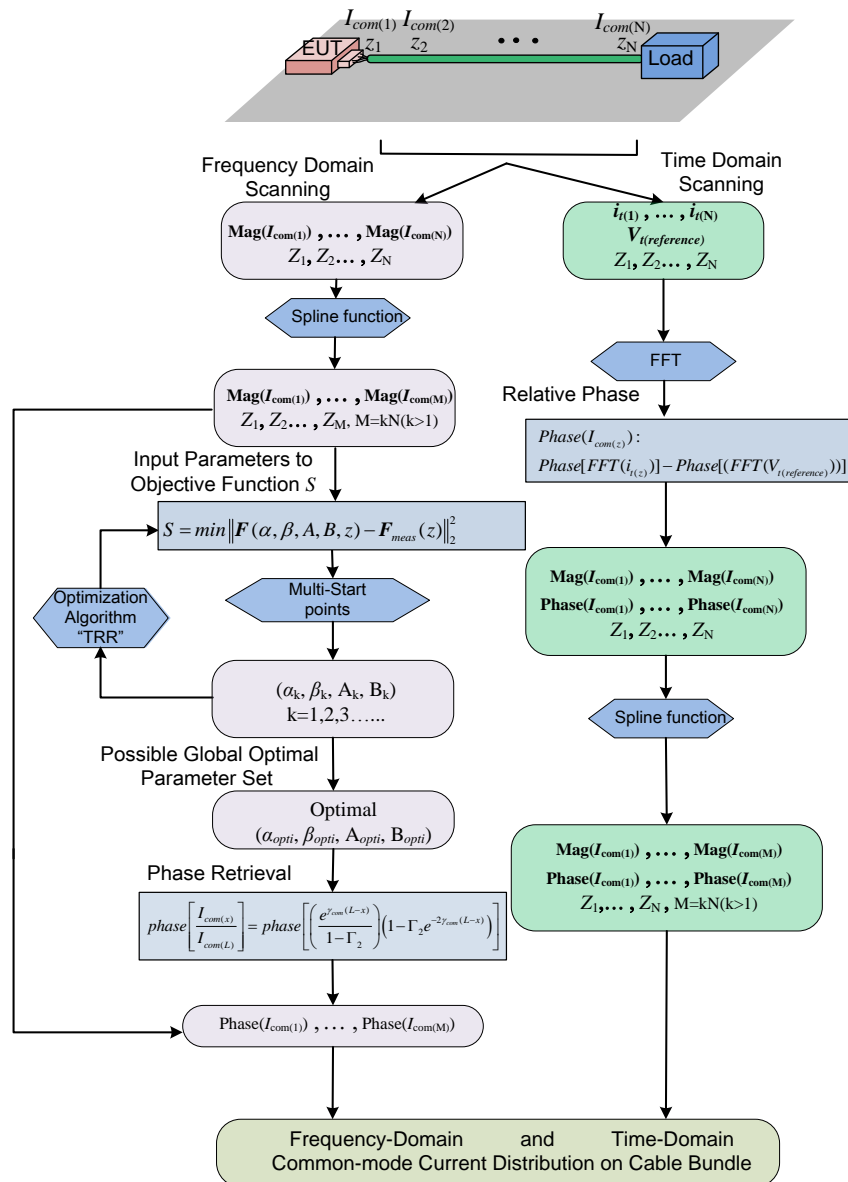


**Figure 2.16** Process illustration of the current scan methods in frequency- and time-domain

# 3 Modeling Radiation of Cable Bundles

As discussed in the chapter before, the common-mode current distribution on a cable bundle can be the main reason for radiated emissions. After acquiring the common-mode current, an appropriate radiation model is needed. In this chapter, electric-dipole based radiation model for a cable bundle is discussed, based on the simplified common-mode current path as depicted in Figure 2.2. The current return path is treated as ideal infinite ground plane, and mirror theory is used for simplification in the preliminary procedure. Proposed current scan methods in last chapter approximate the common-mode current path by a single wire. The equivalence of this simplification in the common-mode radiation estimation will be investigated in this chapter. Furthermore the radiation from differential-mode currents, which are not measured by the current probe, is also discussed through simulations. Next, the errors in the radiation estimation due to the model approximation and the current acquisition accuracy are also analyzed. Finally, limitations and capabilities are discussed by predicting radiated fields from several cable structures in a wide frequency range between 1MHz and 1 GHz.

## 3.1  Multi-Dipole Radiation Model

In Figure 2.2 the common-mode current path of the cable bundle is substituted by a single wire. In order to calculate the radiation due to this common-mode current, the wire can be discretized as a set of electric dipoles as shown in Figure 3.1. The infinite ground can be represented by corresponding mirror images based on mirror theory, which is illustrated in Figure 1.11. All electric dipoles form an antenna array to determine the radiation characteristic of the radiating structure together. In this antenna array, two different dipole structures can be distinguished due to their current flowing directions. One is the dipole with horizontal current parallel to the ground plane; the other is the dipole with vertical current perpendicular to the ground plane. For each electric dipole, the analytic expressions of (1.15) - (1.20), given in Cartesian coordination in Figure 1.10, can calculate the electromagnetic fields. The total radiated emission is the sum of all the contributions from the wire current and its mirror current. In order to verify the multi-dipole radiation model, a MoM model for the wire configuration shown in Figure 3.1 is also constructed, in which the wire is driven by a 1 V (peak value) sinusoidal voltage source with 50 Ω impedance from 1 MHz to 1 GHz. In the radiation calculation by proposed multi-dipole model, the wire current distribution is exported from MoM simulation. The field observation point as denoted in Figure 3.1 is 1 m distant to the wire center, which is also typical antenna distance in ASLE method. Figure 3.2 depicts the total vertical and horizontal electric fields at

the observation point, from the multi-dipole model and the MoM model. Additionally, the field components due to the vertical and horizontal currents are also compared, which are calculated by the multi-dipole model respectively.
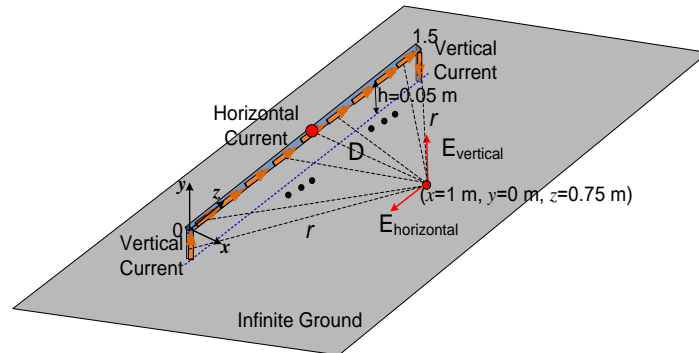


**Figure 3.1** Multi-dipole radiation model for a single wire above an infinite ground plane
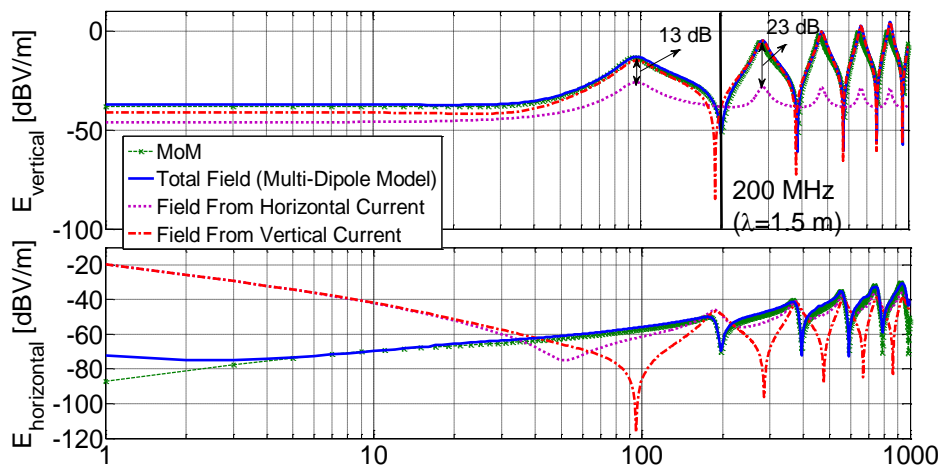


**Figure 3.2** Vertical and horizontal field due to the different current components on the wire from 1 MHz to 1 GHz

It can be seen that the calculated vertical and horizontal field from the multi-dipole model can match well with the fields from the MoM model from 1 MHz to 1 GHz. Vertical current elements and their mirror currents dominate the total vertical field above 200 MHz. The difference between fields from the vertical and horizontal current elements tends to increase as the frequency rises, for example the difference is 13 dB at the first radiation peak but 23 dB at the second peak. This means the contribution of horizontal current on the wire to vertical field calculation can be ignored above 200 MHz. This is a useful conclusion when the geometrical arrangement of the wire configuration and the field observation point are as shown in Figure 3.1. Conversely, the horizontal field at the observation point is contributed

40

from both the vertical and horizontal current elements. These two currents result in the same field magnitude levels at the peaks.

## 3.2 Common- and Differential-Mode Radiation of Cable Bundles

As analyzed in previous chapter, currents travelling along a cable bundle can be decoupled into different modes [65]. The propagation of each mode is characterized by different propagation constants and characteristic. In these modes, the common-mode current travels in the propagation channel between the ground and all wires together. This current component is considered as a main reason for the radiated emissions [47]. The differential-mode currents flowing through the wires, which are assumed to contribute less to radiated emissions, due to the counteraction by the nearby flowing return currents. Using the currents on two wires as illustration, the common-mode current is defined as half of the sum of wire currents, and the differential-mode current is defined as half of the difference of wire currents [30], as depicted in Figure 3.3. In the field estimation, when the distance $S$ between the two wires is much smaller than the field point distance $D$ ($S << D$), the total field can be approximated by the field only due to the common-mode current according to (3.1). Here, $E_1$ represents the electric field at the observation point due to the current $I_1$, which is a function of the distance $D$; $E_2$ represents the electric field due to the $I_2$, which is a function of the distance $D\text{-}S$. When $S$ is negligible compared to $D$, $E_1$ and $E_2$ can be approximated by the same expression $E$. Under this assumption, the two wires can be approximated by a single wire with only common-mode current flowing to calculate the radiated emission. However, in the concerned wire configuration as shown in Figure 3.1, the field point distance $D$ is about 1 m away from the wire, so that the distance of two wires $S$ needs a quantized investigation to ensure the accuracy of common-mode radiation model.
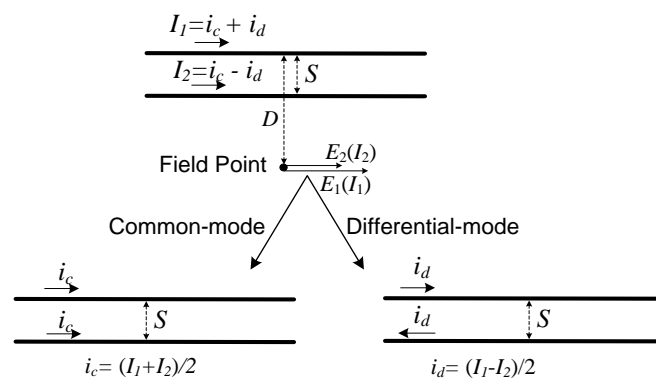


**Figure 3.3** Two wire currents are decoupled to common- and differential-mode currents [30]

$$
\begin{aligned}
E_{total} &= E_1(I_1) + E_2(I_2) \\
&= E_1(i_c + i_d) + E_2(i_c - i_d) \\
&= E_1(i_c) + E_1(i_d) + E_2(i_c) + E_2(-i_d) \\
&= \underbrace{\left(E_1(i_c) + E_2(i_c)\right)}_{E_{com}} + \underbrace{\left(E_1(i_d) + E_2(-i_d)\right)}_{E_{diff}} \\
&\approx \underbrace{\left(E\ (i_c + i_c)\right) + \left(E\ (i_d - i_d)\right)}_{S \ll D,\, E_1 \approx E_2 \approx E} \\
&= E(I_{com})
\end{aligned}
\tag{3.1}
$$

A real cable bundle might possess a cross-sectional diameter in the order of centimeters. In the ALSE method, the field point (antenna reference point) is 1 m distant to the cable center. In this section, the radiation deviation induced by a wire position offset is investigated. For simplification, the two wire currents from Figure 3.3 are used to investigate the question, but external return ground of the common-mode current is also considered here, as shown in Figure 3.4. Two wire currents are also from the above MoM simulation in Figure 3.1. The height of the center wire is 0.05 m above the ground, and the field point is 1 m distant to its center. Radiation is calculated based on the multi-dipole model. In cross-sectional view, the wire at the center position is denoted in red, which is assumed to be the position of the equivalent common-mode current path for a cable bundle. The other wire with current in the same direction has a position offset of $\Delta x$ or $\Delta y$ in the $x$- or $y$-direction with respect to the center wire. Figure 3.5 shows the common-mode radiation field due to the $y$-directional offset of one wire from the center wire. The curve with a red solid line is the radiated field amplitude at the field point when the offset wire coincides with the reference wire. It can be seen that the vertical and horizontal field deviations tend to be larger when the position offset increases. In the vertical and horizontal field, a position offset of less than 1 cm induces maximum 0.8 dB error. The radiated field is much less sensitive to the $x$-directional position offset, compared with the $y$-directional offset. A position offset of less than 5 cm only induces less than 0.7 dB error in the vertical field and 0.63 dB error in the horizontal field.
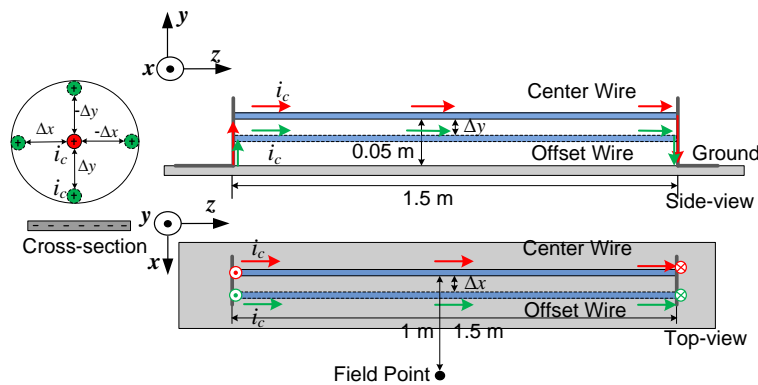


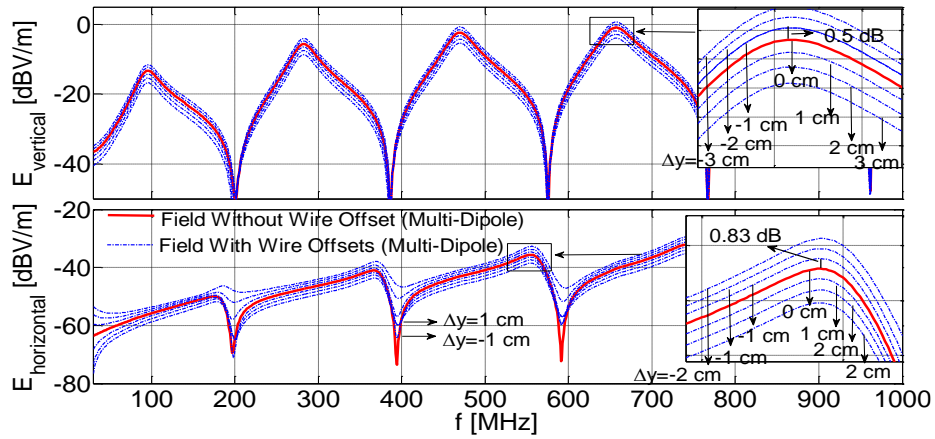**Figure 3.4** Common-mode currents distribution on two single wires with the different arrangements

**Figure 3.5** Common-mode field due to a *y*-directional offset of one wire
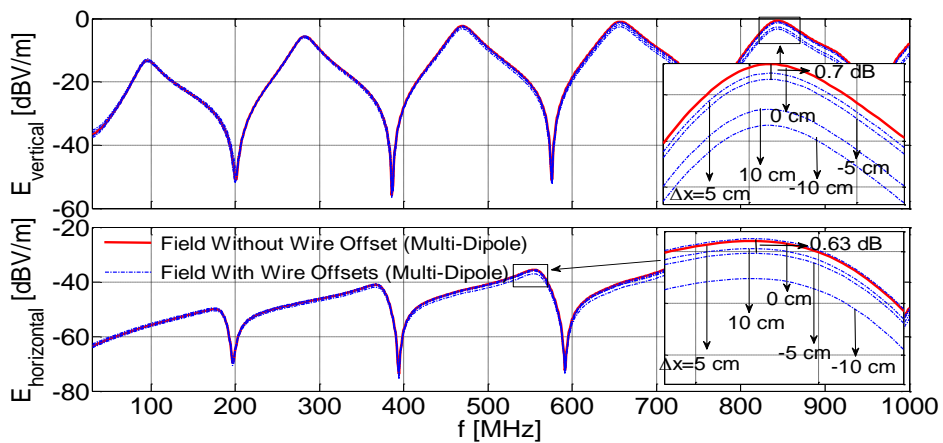


**Figure 3.6** Common-mode field due to an *x*-directional offset of one wire

Figure 3.7 depicts a differential-mode current on the two wires with different positions. As assumed above, the wire shown in red in the cross-sectional view occupies the center position. The other wire with current in the opposite direction has a position offset of Δ*x* or Δ*y* in the *x*- or *y*-direction with respect to the center wire.
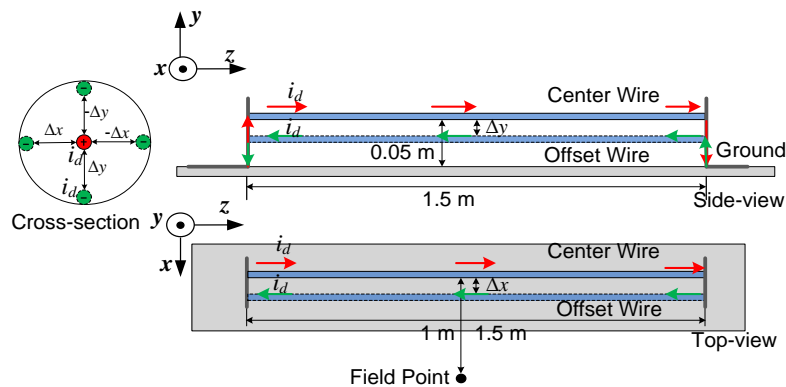


**Figure 3.7** Differential-mode currents distribution on two single wires with the different arrangements

43

In the $y$-direction as shown in the side-view in Figure 3.7, the differential-mode current pair composes a current loop of 1.5 m length and $\Delta y$ width, which is perpendicular to the ground plane. The field observation point is also 1 m distant to the center wire. Similarly with the wire structure in Figure 3.1 in consideration of the mirror return current, the vertical field from the current loop is the main radiation component which is dominated by the two vertical currents on the lines of $\Delta y$ length. The horizontal field from the current loop is nearly zero at the field observation point [30]. The vertical field from the vertical currents on the lines of $\Delta y$ length can be illustrated by Figure 3.8:
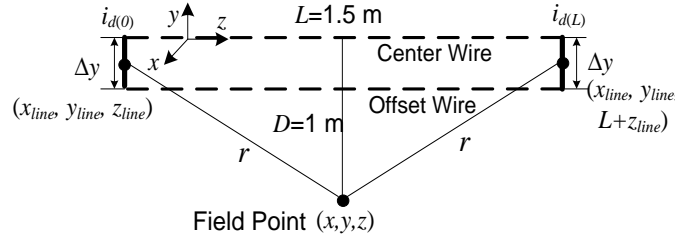


**Figure 3.8** Radiated Field at the observation point from vertical currents on the lines of $\Delta y$ length in the current loop perpendicular to the ground

Based on the electric field expression from a single dipole (1.20), vertical electric field ($y$-direction in the coordinate refers to Figure 3.8) from the two lines of $\Delta y$ length can be calculated by:

$$
\begin{aligned}
E_{vertical} &= E_{vertical}(i_{d(0)}) + E_{vertical}(i_{d(L)}) \\
&= \frac{(i_{d(0)} + i_{d(L)}) \cdot \Delta y \cdot (y - y_{line})^2}{4\pi r^2} M_1(r) e^{-j\beta_0 r} - \frac{(i_{d(0)} + i_{d(L)}) \cdot \Delta y}{4\pi} M_2(r) e^{-j\beta_0 r} \\
&= \frac{(i_{d(0)} + i_{d(L)}) \cdot e^{-j\beta_0 r} \cdot \Delta y^3}{\pi r^2} M_1(r) - \frac{(i_{d(0)} + i_{d(L)}) \cdot e^{-j\beta_0 r} \cdot \Delta y}{4\pi} M_2(r) \\
&\approx -\frac{(i_{d(0)} + i_{d(L)}) \cdot e^{-j\beta_0 r} \cdot \Delta y}{4\pi} M_2(r) \quad (\Delta y \leq 3 \text{ cm}, \ y - y_{line} = \frac{\Delta y}{2})
\end{aligned}
$$

$$(3.2)$$

Where

$$
M_1(r) = \eta_0 \beta_0^2 (j \frac{1}{\beta_0 r} + \frac{3}{\beta_0^2 r^2} - j \frac{3}{\beta_0^3 r^3})
$$

$$
M_2(r) = \eta_0 \beta_0^2 (j \frac{1}{\beta_0 r} + \frac{1}{\beta_0^2 r^2} - j \frac{1}{\beta_0^3 r^3})
$$

$$(3.3)$$

Here $y_{line}$ is the center coordinates of the vertical lines with $\Delta y$ length; $y$ is field observation point in the $y$ direction; and $r$ is the distance from the observation point to both vertical lines. If the offset in the $y$ direction is $\Delta y \leq 3$ cm ($\Delta y / \lambda_{min} \leq 0.1$, $\lambda_{min}$ is the wavelength at 1 GHz), the current amplitude and phase on the start and end vertical lines $i_{d(0)}$ and $i_{d(L)}$ are nearly constants, i.e. these two vertical lines can be seen as

short single dipoles. Additionally, the distance $r$ is also approximated to be a constant, when $\Delta y$ has a small change. Therefore, the vertical field due to the differential-current loop perpendicular to the ground plane is a linear function with respect to $\Delta y$ according to (3.2). Compared with common-mode radiation of $\Delta y = 1$ cm in Figure 3.5, the differential-mode vertical field of $\Delta y = 1$ cm is about 26 dB lower, as depicted in Figure 3.9. Since the common-mode current and its mirror current consist of a similar current loop with 1.5 m length and $\Delta y = 10$ cm width, this vertical field is 20 dB higher than the differential-mode radiation of $\Delta y = 1$ cm width. The additional "6 dB" results from the superposition of two wire currents in the common-mode radiation calculation, where one wire current has the same amplitude as the current in differential-mode radiation calculation.
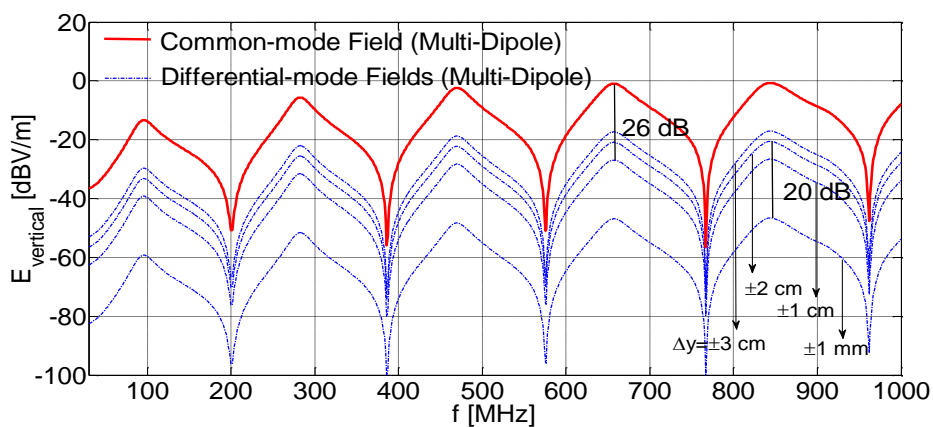


**Figure 3.9** Differential-mode field in vertical direction for the different $y$-directional offset distances

In the $x$-direction as shown in the top-view of Figure 3.7, the differential-mode currents in the offset wire and the center wire are parallel to the ground plane. When the coupling between the two wires is much larger than the coupling between wires and the ground, their return currents on the common ground can cancel each other out. In this case, the ground plays no role in the radiation estimation. One wire can be seen as the current return path of the other wire. According to [78], the wire spacing $\Delta x$ must be smaller than $h/2$ ($h$ is 5 cm, the height of the center wire above the ground), so that the ground influence can be ignored. Under this condition, the differential-mode radiation in this scenario is only due to two 1.5 m length wires with $\Delta x$ spacing in a plane parallel to the ground plane. The radiation can be obtained by the sum of the field from each dipole pair on the horizontal lines. When $\Delta x << r$ (the distance from field point to the center of the dipole), the field can be calculated according to the illustration as shown in Figure 3.10 [30].

As shown in the field expression (1.19), if the field observation point and the dipole pair are on the same $xz$-plane (i.e. $y = y_{line}$ in Figure 3.10), the vertical electric field ($y$-direction) from each dipole will be zero. The horizontal electric field ($z$-

direction) can be calculated from (3.4) to (3.7) based on (1.20). $M_1(r)$ and $M_2(r)$ are defined by (3.3). It can be seen that the field expression is a linear function of wire spacing $\Delta x$. Also, the total field is linearity with $\Delta x$, as it is the sum of the field contributions from each dipole pair with different position $z$ and angle $\alpha$.

$$
\begin{aligned}
E_{horizontal}(i_{d(z)}) &= \frac{i_{d(z)} \cdot dz \cdot (z - z_{line})^2}{4\pi r_1^2} M_1(r_1)e^{-j\beta_0 r_1} - \frac{i_{d(z)} \cdot dz}{4\pi} M_2(r_2)e^{-j\beta_0 r_1} \\
&\approx \frac{i_{d(z)} \cdot dz \cdot (z - z_{line})^2}{4\pi r^2} M_1(r)e^{-j\beta_0(r + \frac{\Delta x}{2}\cos\alpha)} \\
&\quad - \frac{i_{d(z)} \cdot dz}{4\pi} \eta_0 \beta_0^2 M_2(r)e^{-j\beta_0(r + \frac{\Delta x}{2}\cos\alpha)}
\end{aligned}
\tag{3.4}
$$

$$
\begin{aligned}
E_{horizontal}(-i_{d(z)}) &= \frac{-i_{d(z)} \cdot dz \cdot (z - z_{line})^2}{4\pi r_2^2} M_1(r_2)e^{-j\beta_0 r_2} + \frac{i_{d(z)} \cdot dz}{4\pi} M_2(r_2)e^{-j\beta_0 r_2} \\
&\approx -\frac{i_{d(z)} \cdot dz \cdot (z - z_{line})^2}{4\pi r^2} M_1(r)e^{-j\beta_0(r - \frac{\Delta x}{2}\cos\alpha)} \\
&\quad + \frac{i_{d(z)} \cdot dz}{4\pi} M_2(r)e^{-j\beta_0(r - \frac{\Delta x}{2}\cos\alpha)}
\end{aligned}
\tag{3.5}
$$

$$
\begin{aligned}
E_{horizontal} &= E_{horizontal}(i_{d(z)}) + E_{horizontal}(-i_{d(z)}) \\
&= \frac{i_{d(z)} \cdot dz \cdot (z - z_{line})^2}{4\pi r^2} M_1(r)e^{-j\beta_0 r} (e^{-j\beta_0 \frac{\Delta x}{2}\cos\alpha} - e^{j\beta_0 \frac{\Delta x}{2}\cos\alpha}) \\
&\quad + \frac{i_{d(z)} \cdot dz}{4\pi} M_2(r)e^{-j\beta_0 r} (e^{j\beta_0 \frac{\Delta x}{2}\cos\alpha} - e^{-j\beta_0 \frac{\Delta x}{2}\cos\alpha})
\end{aligned}
\tag{3.6}
$$

Since $e^{jA} - e^{-jA} = 2j \cdot \sin A$, and $\sin A \approx A$ ($A \ll 1$), (3.6) can be simplified to the expression below, as given in [30]:

$$
\begin{aligned}
E_{horizontal} &= E_{horizontal}(i_{d(z)}) + E_{horizontal}(-i_{d(z)}) \\
&= \frac{i_{d(z)} \cdot dz \cdot (z - z_{line})^2 \cdot (-j\beta_0)}{4\pi r^2} M_1(r)e^{-j\beta_0 r} (\Delta x \cos\alpha) \\
&\quad + \frac{i_{d(z)} \cdot dz \cdot (j\beta_0)}{4\pi} M_2(r)e^{-j\beta_0 r} (\Delta x \cos\alpha) \\
&= F(z) \cdot (\Delta x \cos\alpha)
\end{aligned}
\tag{3.7}
$$

Figure 3.11 depicts the horizontal field at the field observation point from the horizontal lines with differential-mode currents. The field from the two wires when wire spacing $\Delta x = 1$ cm is 20 dB higher than the field when $\Delta x = 1$ mm. Compared with common-mode radiation results as shown in Figure 3.6 when $\Delta x = 1$ cm and the ground is infinite, this differential-mode horizontal field at the similar radiated level. However, when the ground is finite in the ALSE method, the common-mode radiation

level will be increased by about 20 dB in horizontal direction, as depicted in Figure 3.11. The reason for the increase is due to the surface currents on the finite ground, which are induced by the common-mode currents. As the compensation of the differential-mode currents on the ground, the finite ground nearly has no influence on differential-mode radiation.
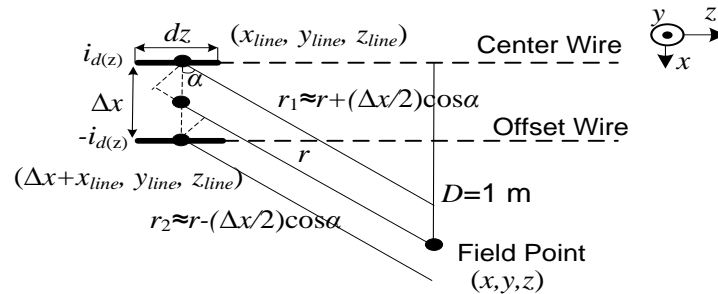


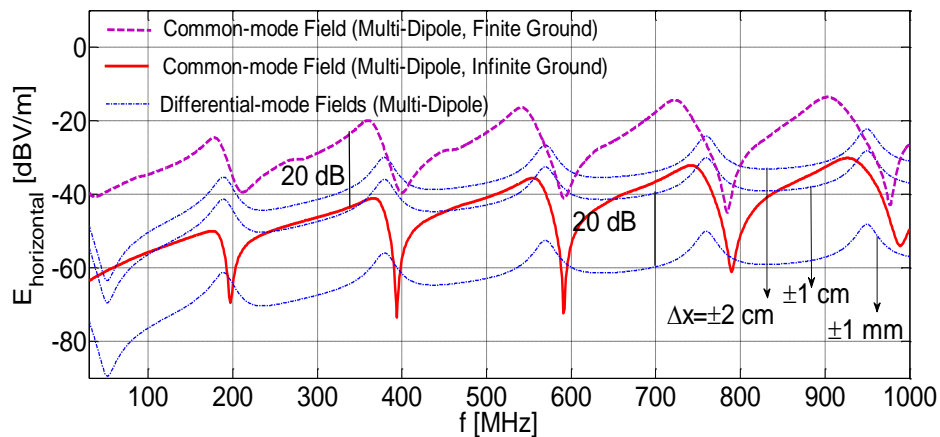**Figure 3.10** Radiated Field at the observation point from two wires at a parallel plane



**Figure 3.11** Differential-mode field in horizontal direction due to $x$-directional wire offset

From the analysis above, in the scenario of common-mode radiation, a $y$-directional wire offset of 1 cm induces less than 1 dB deviation in radiated field at the field observation point. An $x$-direction wire offset of 5 cm induces less than 1 dB deviation. In the scenario of differential-mode radiation, the resulted vertical field at the field observation point is mainly due to the currents which are perpendicular to the ground plane. This field is nearly a linear function of the position offset $\Delta y$ (the width of the current loop). Additionally, the common-mode radiation is about 26 dB higher than the differential-mode radiation in vertical direction when $\Delta y$ = 1 cm. The resulted horizontal field at the field observation point is mainly due to two currents parallel to the ground. This field is nearly a linear function of the position offset $\Delta x$ (the spacing between the two wires). Additionally, if the used ground is finite in the ALSE method, the common-mode radiation level is about 20 dB higher than the differential-mode radiation level in horizontal direction when $\Delta x$ = 1 cm. Even though

a real cable bundle has a more complex composition, the two-wire scenarios above depicted in Figure 3.4 and Figure 3.7 can represent the basic common- and differential-mode scenarios. Therefore, the axial center of the cable bundle is sufficiently accurate to simplify the equivalent common-mode path in the radiation model, if the cross-sectional radius of the cable bundle is less than 1 cm. Within this distance, the differential-mode radiation can be ignored, compared with common-mode radiation.

## 3.3 Common-Mode Radiation Prediction Based on Current Scan Methods

As discussed above, it is reasonable only to consider the common-mode radiation if the cross-sectional radius of a cable bundle is less than 1 cm. Within this range, the common-mode current path can be modeled as a single wire. Prediction of the common-mode radiation from a cable bundle can be realized using a multi-dipole radiation model. The multi-dipole model divides the common-mode current path into a set of short segments, as shown in Figure 3.12. Each segment can be treated as an electric dipole with the current amplitude and phase from measurements and post processing of measurement data. The return current is modeled by mirror currents. The total electromagnetic field can be calculated as the sum of all fields from each electric-dipole and its mirror image. However, as explained before there are additional necessary considerations in the radiation prediction, for example the determination of common-mode currents at the vertical segments and the current measurement sensitivity due to the equipments.
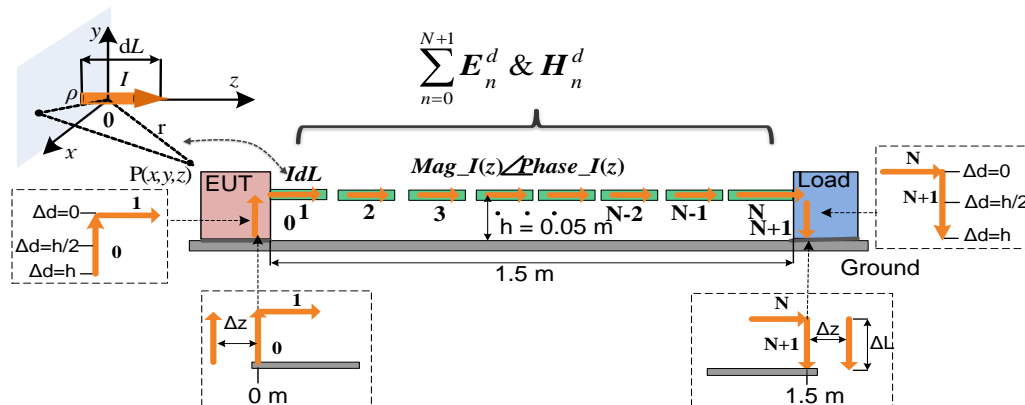


**Figure 3.12** Multi-dipole radiation model for a cable bundle

### 3.3.1 Vertical Current Approximations in Radiation Model

The common-mode currents at the $0$th or $(N+1)$th vertical segments as depicted in Figure 3.12 are difficult to determine through direct measurements. One simple solution is to approximate these two segment currents by the currents measured at

the first and $N$th wire segments respectively. However, adding these two vertical segments means an extra length of transmission line, which would induce deviations especially at high frequencies [79]. The other more accurate solution is to extrapolate these two segment currents if the common-mode transmission line parameters of the cable bundle are known.

For analysis of vertical segment currents, the same wire structure in Figure 3.1 is referred here. Figure 3.13 shows current amplitudes from 1 MHz to 1 GHz on the load vertical segment center ($\Delta d = h/2$) in Figure 3.12, which are calculated from MoM and the extrapolated approximations using a transmission line model. Compared with MoM, the vertical current approximated by $N$th segment current ($\Delta d = 0$) possesses apparent error above 600 MHz, but the extrapolated approximation at the vertical segment center ($\Delta d = h/2$ or $h$) can improve its accuracy significantly. Figure 3.14 shows the vertical and horizontal fields at the field observation point, when the currents on the vertical segments are approximated by different solutions. The current extrapolated at the vertical segment center ($\Delta d = h/2$) can achieve the best accuracy in both the vertical and horizontal field. The currents approximated by the first and $N$th element currents ($\Delta d = 0$) mainly induce deviation in the vertical field above 600 MHz, but they have nearly no influence in the horizontal field except at the resonance minimum around 850 MHz and 950 MHz. This rule is also applicable to different source or load impedances. When implementing the proposed current scan methods to predict the common-mode radiation, the extrapolated approximation for vertical segment currents can be easily achieved in the frequency-domain scan method, due to the retrieved transmission line parameters by the optimization algorithm. Even if the vertical segment currents have to be approximated by the first and $N$th segment currents in the time-domain scan method due to the lack of transmission line parameters, this approximation can give also good field accuracy, with exception of the vertical fields above 600 MHz.
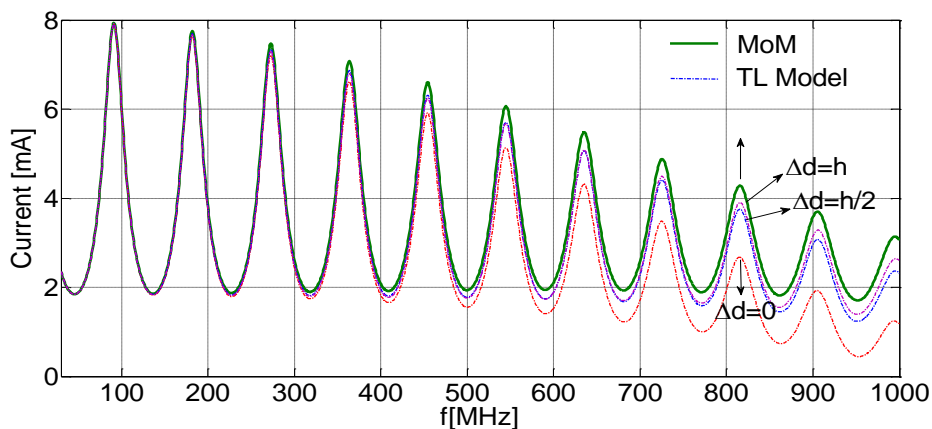


**Figure 3.13** Vertical current on the load terminal from the MoM and the extrapolated approximation based on transmission line (TL) model
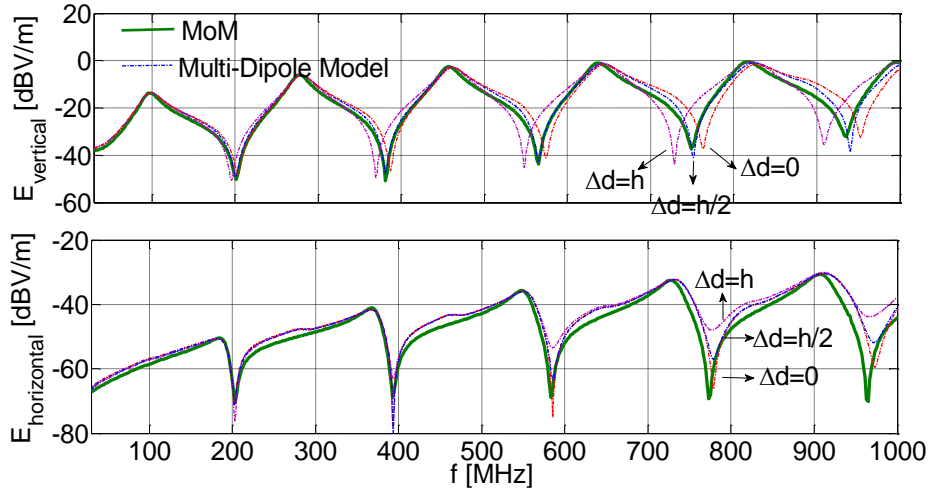
**Figure 3.14** Radiated fields at the field point based on the MoM and the multi-dipole model with different approximated vertical currents on the source and load terminals

## 3.3.2 Influence of Vertical Current on the Radiation Prediction Quality

As analyzed above, currents at vertical segments in the wire configuration (Figure 3.1) are significant to the vertical and horizontal field at the observation point. In the proposed multi-dipole radiation model shown in Figure 3.12, EUT and load component are modeled by simple $0$th and $(N+1)$th vertical segments of 5 cm length, respectively. Each segment is treated as an electric dipole in the radiation calculation. However, if taking into account the real size of components, some considerations for this simplification are necessary. First consideration is the length of these two segments. Figure 3.15 shows the radiated fields at the field observation point when the vertical segments with different lengths ($\Delta L = 5$ cm as reference). It can be seen that the vertical field at peaks is increased by 1.6 dB or reduced by 2 dB when the vertical segment length $\Delta L$ adds or subtracts 1 cm. Moreover, the changes of $\Delta L$ within 2 cm induce less than 1 dB error at the horizontal field peaks; whereas it has a big influence on the resonance minimums of the horizontal field.

The other consideration is the position offset $\Delta z$ of the vertical segments. In modeling of a cable bundle, the $0$th and $(N+1)$th vertical segments are located on $z = 0$ and $z = 1.5$, to represent the EUT and load components. However, the real vertical currents are more complex than the modeling by single vertical current elements; and they might exist on the different positons on the components. Different positions of vertical current paths might influence the radiation levels. Therefore, the position offsets in $z$-direction of $0$th or $(N+1)$th vertical segments in Figure 3.12 are investigated here. Figure 3.16 shows the radiated fields at the field observation point when the $0$th or $(N+1)$th vertical segments at different positions on the ground. It can be seen that position offset $\Delta z$ nearly has no influence on the vertical and horizontal

field peaks. However, for the most resonance minimums of vertical field, the position offset $\Delta z$ from $(N+1)$th vertical segment, which represents the load component, will shift them to higher frequencies and increase their magnitudes. For example, positon offset $\Delta z$ of 1 cm can shift resonance minimum from 575 MHz to 579 MHz, and it increases the magnitude by about 13 dB. Conversely, position offset $\Delta z$ from $0$th vertical segment, which represents the EUT component, will shift the most resonance minimums to lower frequencies. For the most resonance minimums of horizontal field, both position offsets $\Delta z$ from $0$th and $(N+1)$th vertical segment will shift them to lower frequencies, but change the magnitudes very little. For example, positon offset $\Delta z$ of 1 cm can shift resonance minimum from 591 MHz to 588 MHz.
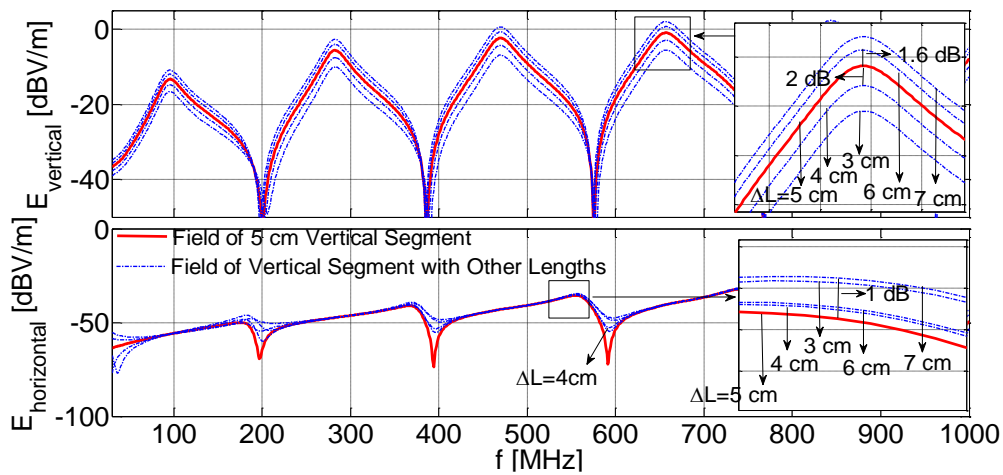


**Figure 3.15** Radiated fields at the field point when the vertical segments with different lengths and the fields are calculated based on multi-dipole model
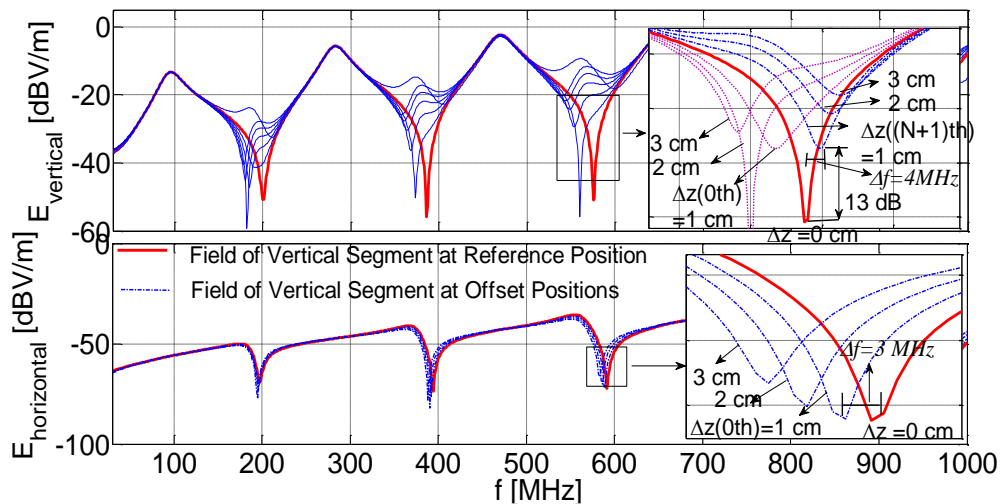


**Figure 3.16** Radiated fields at the field point when the vertical segments at different positions and the fields are calculated based on multi-dipole model

51

### 3.3.3  Influence of Current Accuracy on the Radiation Prediction Quality

In the previous chapter, the minimum current amplitudes has been investigated that can be measured by equipments, as shown in Figure 2.10 for the used EMI receiver and Figure 2.12 for the used oscilloscope. In reality, the common-mode current flowing along a cable bundle can be a standing wave with different amplitudes at different cable positions because of terminal reflections. When the wire in Figure 2.4 is driven by a 1 V voltage source and terminated by a load of 0 Ω or 50 Ω, the current amplitude distributions at 100 MHz are shown in Figure 3.17. The SWR (Standing Wave Ratio) is defined here as the maximum amplitude minus the minimum at the adjacent node in decibels. It can be seen that the SWR may be greatly different, for example 15 dB SWR at the 50 Ω load but 46 dB SWR at the 0 Ω load.
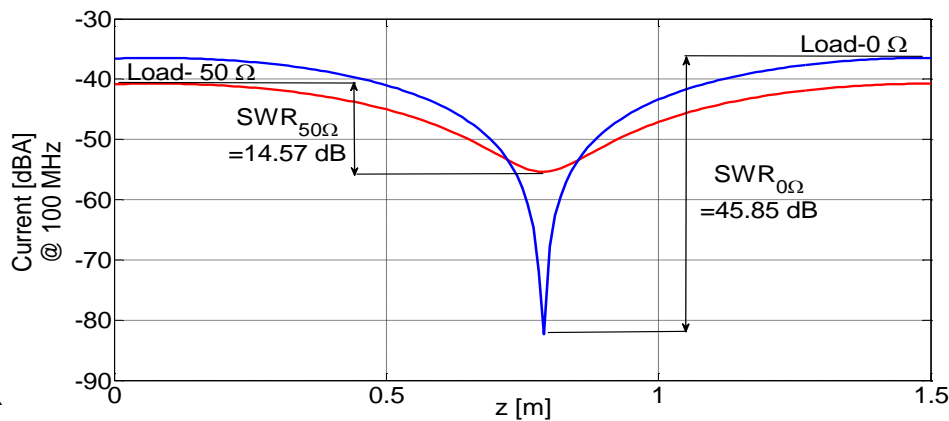


**Figure 3.17** Different SWRs at 100 MHz when a wire is terminated by a 0 Ω and 50 Ω load

A highly dynamic amplitude range of the standing wave is a challenge to the current acquisition in a real current measurement; because even the maximum current amplitude is often only in the order of dBμA in an EMC test. Missing the current amplitudes around minimum value in the current standing wave is possible. The current amplitudes around the minimum might be below the measurement sensitivity limit. To investigate this problem, the amplitude effective factor $k$ is defined as:

$$k = \frac{I_{read\_min}(dB) - I_{Min}(dB)}{SWR(dB)} \quad (I_{Max} \geq I_{read\_min} \geq I_{Min})$$

(3.8)

$$SWR = I_{Max}(dB) - I_{Min}(dB)$$

52

Here $I_{Max}$ and $I_{Min}$ represent the real maximum and minimum current amplitude on the wire. $I_{read\_min}$ represents observed readings from the receiving equipments, which might be pseudo-amplitude or noise. The wire terminated with a 50 Ω load terminal is used for illustration. Figure 3.18 (upper) and Figure 3.19 (upper) show the current amplitude distribution with different effective factors from 0.2 to 0.6. The larger is the $k$, the more real current amplitudes will be missing. When the current is measured by an EMI receiver in the frequency domain, these real missing current amplitudes are often substituted by the noise floor, as the measurement sensitivity is only 2 or 3 dB higher than the noise floor. When the current is measured by an oscilloscope, these real current amplitudes are often substituted by the pseudo-amplitude and -phase data from FFT of time-domain data. To obtain these missing real amplitudes, two possible solutions are proposed: The first solution is to retrieve the missing current data based on the equivalent transmission line parameters, which are from the retrieval algorithm discussed in last chapter. However, the lack of too many real amplitudes leads to the reduced accuracy of the retrieved amplitude and phase distribution, for example $k = 0.6$ in Figure 3.18. The second solution is to reconstruct the missing current data based on correct current records on other positions through an interpolation function, such as *Spline* function which possesses a sufficiently high degree of smoothness, as shown in Figure 3.19 .
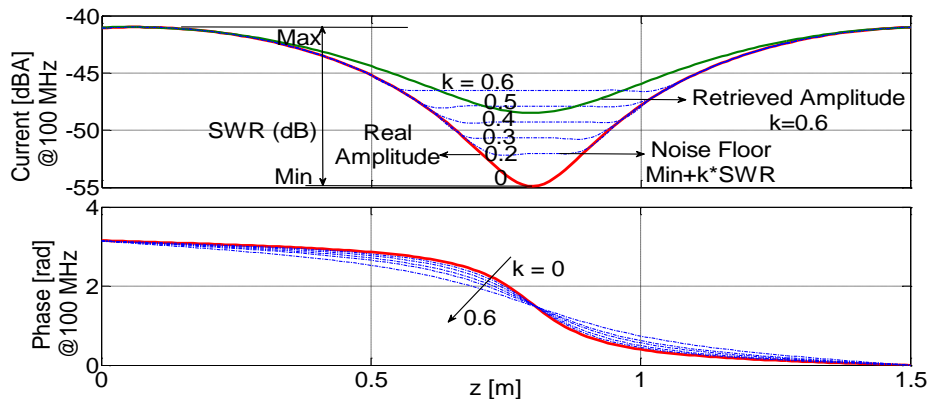


**Figure 3.18** Retrieved current amplitude and phase with different amplitude effective factors based on transmission line model
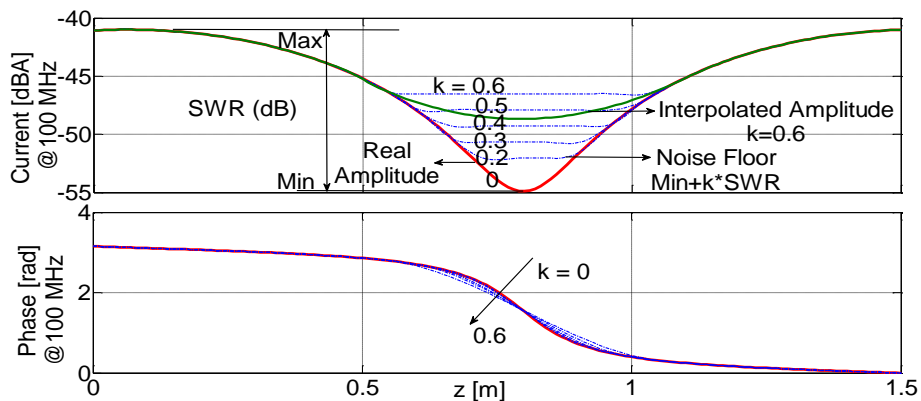


**Figure 3.19** Interpolated current amplitude and phase with different amplitude effective factors based on a *spline* interpolation function

The impact on radiation field prediction due to the missing current data around the minimum values in the standing waves is further investigated. The wire radiation configuration refers to Figure 3.1. Figure 3.20 shows the vertical and horizontal field when the amplitude effective factor $k$ is between 0.2 and 0.6, based on the retrieved current data from a transmission line model. It can be seen that the maximum field error is below 2 dB in vertical field at 180 MHz and 2.5 dB in the horizontal field when $k \leq 0.3$ at 100 MHz. Figure 3.21 shows the vertical and horizontal field when the amplitude effective factor $k$ is between 0.2 and 0.6, based on the interpolated current data. It can be seen that the maximum field error is below 1 dB in vertical field up to 1 GHz and 2.5 dB in horizontal field below 600 MHz when $k \leq 0.3$. But the horizontal field from 600 MHz to 1 GHz can almost not be estimated using the interpolated amplitude and phase information when $k > 0.3$.

As well as the 50 Ω load case, the load cases of short and open are also analyzed. These simulation results show that the vertical fields are less sensitive to the missing data around the minimum value in the standing waves. In the retrieval solution based on transmission line model, the predicted field error mainly originates from the retrieved phase error due to the incomplete amplitude distribution. In the interpolation solution based on a *spline* function, the predicted horizontal field often has a big deviation, which mainly originates from the reconstruction failure when much current data are missing. In a real cable bundle, the common-mode current standing wave distribution may be caused by superposition of many complex terminals. If the minimum current amplitude is higher than the sensitivity limits from receiving equipments, there is no influence on the proposed current scan methods. If the minimum current amplitude is lower than sensitivity limit 0.3·SWR (dB) or more, the radiation prediction cannot be successful at some frequencies due to the wrong current amplitude and phase data, even if the missing data are re-calculated by the proposed retrieval solution based on transmission line model or interpolation solution.
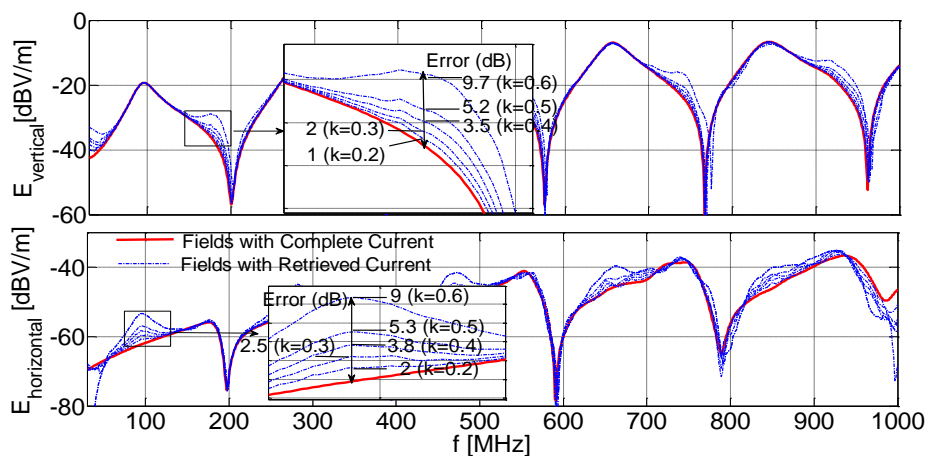


**Figure 3.20** Radiated fields based on the retrieved current with different amplitude effective factors, and fields are calculated based on multi-dipole model
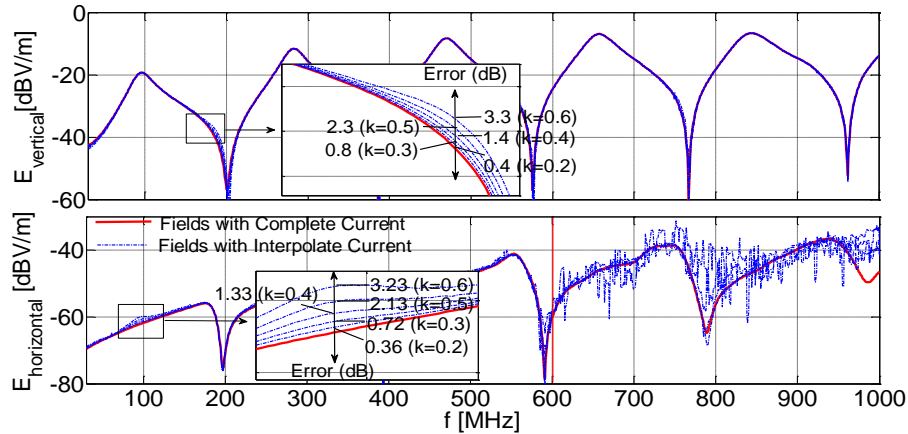
54

**Figure 3.21** Radiated fields based on the interpolate current with different amplitude effective factors, and fields are calculated based on multi-dipole model

# 3.4 Application and Validation Using Infinite Ground

In order to testify the common-mode current scan methods and the multi-dipole radiation model for a cable bundle, several cable structures are constructed: a twisted-pair cable driven by a common- and differential-mode voltage, and a more complex cable bundle with seven wires which terminated by random resistors. For the measurement of the vertical electric field, a 20 cm short rod antenna is attached directly to a metallic plate. In the radiation estimation from the cable bundles, the metallic plate is treated as an ideal infinite ground for simplification, which can be modeled by the mirror theory.

## 3.4.1 Twisted-Pair Cable Driven by a Common-Mode Voltage

The radiation test set-up of a twisted-pair cable is shown in Figure 3.22. The cable is driven by a VNA and terminated by a common-mode 50 Ω load. A MoM model for this configuration is also constructed to obtain $S_{21}$, which is calculated from the antenna voltage $V_{ant}$ and source voltage $V_S$.
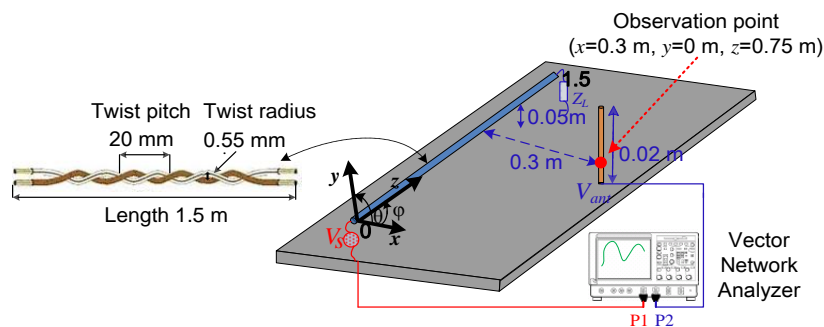


**Figure 3.22** Radiation test from a twisted-pair cable driven by a common-mode voltage

55

Figure 3.23 shows the results of S$_{21}$ by measurement and MoM. The two curves match very well from 10 MHz up to 1 GHz. The measurement curve below 10 MHz includes obvious noise data due to the weak capacitive coupling at low frequencies between the cable and the rod antenna.
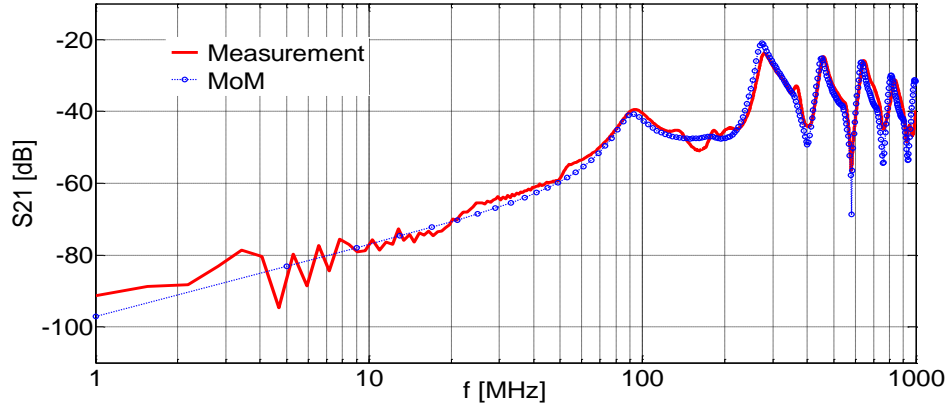


**Figure 3.23** S21 of measurement and simulation for the short rod antenna test configuration

An RF current probe is used to scan the common-mode currents at cable position $z$ = [0:0.06:1.5], and then the *spline* function is employed to interpolate the measured data at $z$ = [0:0.01:1.5]. Common-mode current amplitude and phase along the twisted-pair cable also can be measured with VNA, which can be applied to validate the retrieved phase. Electric field in the $y$-direction (vertical polarization) at the observation point is calculated. Figure 3.24 shows the electric field from 30 MHz to 1 GHz by measurement, MoM and the proposed current scan method. Here the measured $E_{y\_meas}$ is calculated as:

$$E_{y\_meas} = V_{ant\_meas} \cdot AF_{MoM}$$

$$V_{ant\_meas} = \frac{S21_{meas} \cdot V_S}{2} \quad (V_S = 1)$$

(3.9)

Antenna factor of the short rod antenna $AF_{MoM}$ is calculated using the simulated results from a verified MoM model according to the configuration shown in Figure 3.22. $V_{ant\_meas}$ is the received voltage of the short rod antenna, calculated from the measured S21$_{meas}$. The predicted field based on the proposed current scan method in frequency domain match well with the measurement and the MoM data from 30 MHz to 1 GHz. Figure 3.25 depicts a comparison of the methods at low frequencies (1 MHz – 30 MHz). In this frequency range, the proposed current scan method fails to predict the electric field due to deviation of the retrieved phase, which can be traced to the sensitivity of multi-dipole radiation model to phase deviation at low frequencies. For example, the retrieved phase distribution based on the measured current amplitude Mag(I$_{Meas}$) and simulated current amplitude Mag(I$_{MoM}$) at 1 MHz and 10

MHz presents small errors, as shown in Figure 3.26. However, these small errors can lead to great deviations in the electric field calculation. In Figure 3.25, the electric field at 1 MHz calculated from phase retrieved by Mag($I_{MoM}$) matches the measured field very well, while the calculated field from phase retrieved by Mag($I_{Meas}$) has high deviation of 25 dB. When the current amplitude and phase are both measured from the VNA denoted by 'Mag($I_{Meas}$) and Phase($I_{Meas}$)', the calculated electric field by multi-dipole method is very similar to the measured antenna field from 1 MHz to 30 MHz.

It can be concluded from the analysis above that the multiple-dipole radiation model with retrieved current phase can reach good accuracy in the radiation prediction from 30 MHz to 1 GHz. Whereas below 30 MHz, a small deviation in the retrieved phase may lead to a failure in the radiated field prediction. Furthermore, the lower the frequency is, the bigger is the field deviation. This problem is mainly from the high sensitivity of proposed multi-dipole model to the inaccuracy phase distribution at low frequencies.



**Figure 3.24** Electric field at the observation point from the antenna measurement, MoM and multi-dipole radiation model with retrieved current phase from 30 MHz to 1 GHz
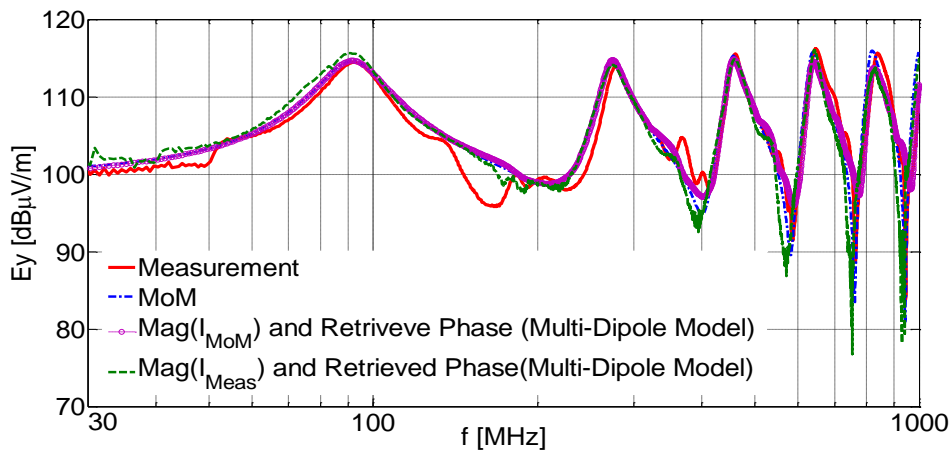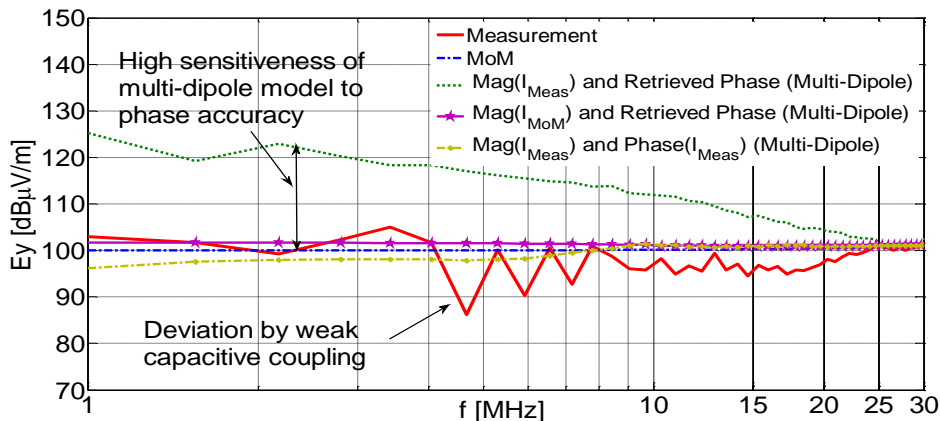


**Figure 3.25** Electric field at the observation point from the antenna measurement, MoM and multi-dipole radiation model with retrieved current phase from 1 MHz to 30 MHz
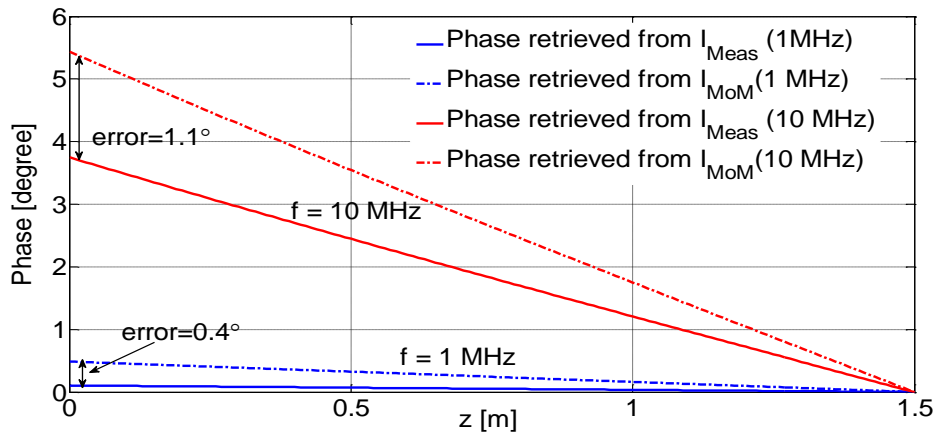
**Figure 3.26** Retrieved current phase distribution along the cable based on MoM and measured current amplitude at 1 MHz and 10 MHz

## 3.4.2 Twisted-Pair Cable Driven by a Differential Voltage Pair

In order to verify both frequency- and time-domain current scan methods, we further investigate the radiation from a twisted-pair cable through measuring the received voltage on the rod antenna as shown in Figure 3.22 . The twisted-pair cable is fed by a differential voltage pair from a 2-port signal generator (Tektronix AFG 3252). Differential voltage sources $V_p$ and $V_m$ are pulses with frequency 40 MHz and peak-peak value of 5 V. The asymmetric delay time ($V_m$ to $V_p$) 5 ns adds a common-mode voltage $V_{com}$ ($V_p + V_m$), as shown in Figure 3.27 (lower). In order to create a more realistic case with asymmetrical resistances, the wires are terminated by 50 Ω and "open", as depicted in Figure 3.27 (upper).
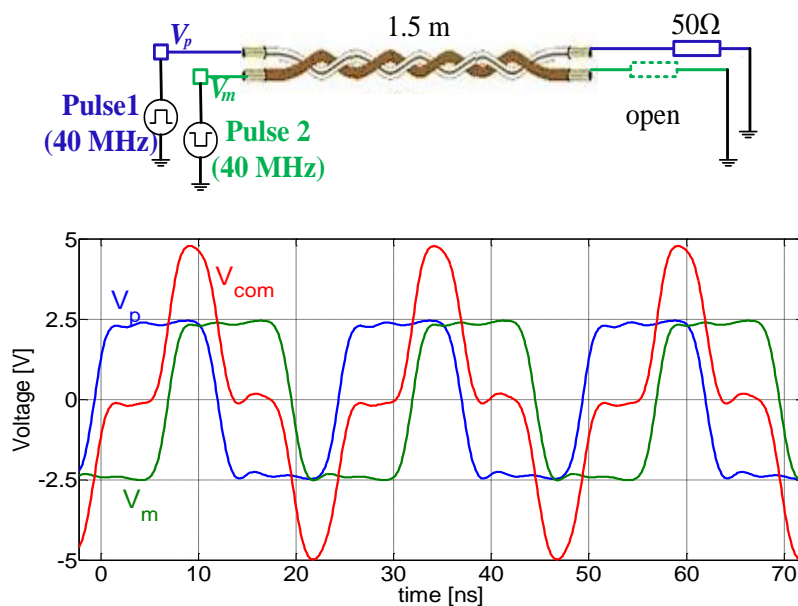


**Figure 3.27** Twisted-pair cable driven by a differential voltage pair

Current amplitudes are scanned with F-65 current probe with the referred EMI receiver (average detector, 120 kHz BW and 5 ms MT) or the referred oscilloscope (550 μs sample time and 0.5 ns interval time); and then phase information at each frequency is calculated using proposed phase retrieval method or FFT. Finally, the electric field at the observation point is calculated. In the time domain scanning, single sweep and averaged sweep of the oscilloscope are both used to acquire current distribution. Figure 3.28 presents the current amplitude and phase distribution on the cable acquired by the EMI receiver and the oscilloscope at different frequencies, for example the distributions at 40 MHz, 200 MHz, 240 MHz and 320 MHz. Based on the acquired current distributions, Figure 3.29 shows the electric field in the *y*-direction from the antenna measurement and the simulations at the main radiation peaks. Figure 3.30 depicts a comparison of the predicted field when the current is acquired by the oscilloscope with single sweep and averaged sweep.

Figure 3.31 shows the calculated deviation at the radiated peaks from the frequency- and time-domain current scan methods, compared with the direct antenna measurement. Main radiation frequency peaks include 10 harmonics and several non-harmonics (50 MHz, 110 MHz, 130 MHz, 210 MHz and 290 MHz), which may result from the signal generator control circuit. Compared with the antenna measurement, the calculated deviations at these peaks based on frequency-domain current scan method by the EMI receiver are less than 4 dB. Only peak at 400 MHz has a deviation of 5 dB. In contrast, the deviations using the time-domain current scan method by the oscilloscope are less than 6.5 dB in the single sweep. But non-harmonic of 290 MHz cannot be recorded successfully. Additionally, compared with the single sweep of oscilloscope as shown in Figure 3.30, the averaged sweep can reduce the noise floor by 20 dB and more, and gives nearly the same predicted field value when amplitude is high. However, the peaks at non-harmonics at 50 MHz, 110 MHz, 130 MHz, and 210 MHz are much lower because of the averaging function [77].
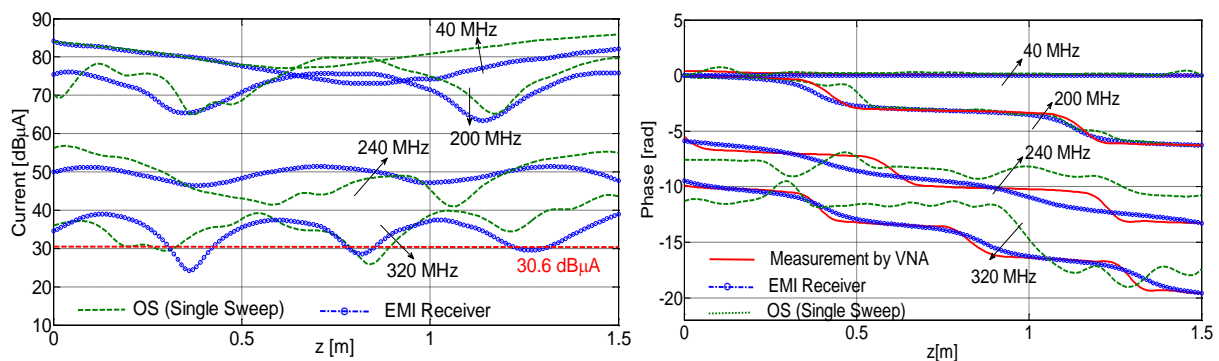


**Figure 3.28** Current distributions scanned by the EMI receiver and oscilloscope (OS)
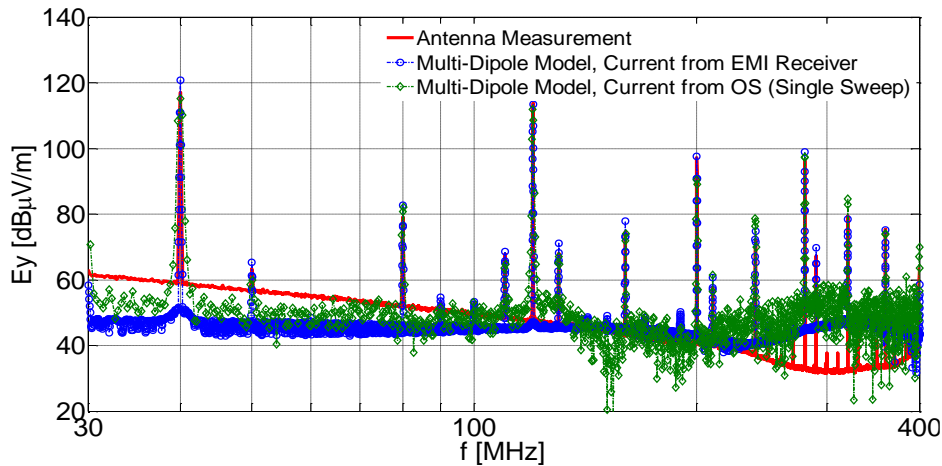
**Figure 3.29** Electric field from the antenna measurement and the multi-dipole radiation model based on cable current scanned by the EMI receiver and the oscilloscope (OS) with single sweep

Several reasons could lead to these deviations. First of all, common factors are the deviation of transfer impedance from the RF current probe ($\pm 2$ dB deviation), and the rod antenna factor $AF_{MoM}$ defined in (3.9) from the MoM model. Secondly, compared with the frequency-domain scan method, time-domain scan method is more sensitive to small signals, especially for the phase measurement. For example, in Figure 3.28 the current amplitude and phase distributions at 240 MHz and 320 MHz show more instabilities compared with the current at 40 MHz and 200 MHz, because the amplitude becomes smaller when the frequency rises. The weak current amplitude at 320 MHz is close to the measurement limit from the oscilloscope (30.6 dBμA). This instable current distribution acquired by the oscilloscope leads to a relatively larger 5 dB error in the final radiation prediction, compared with the case when the current is acquired by the EMI receiver.
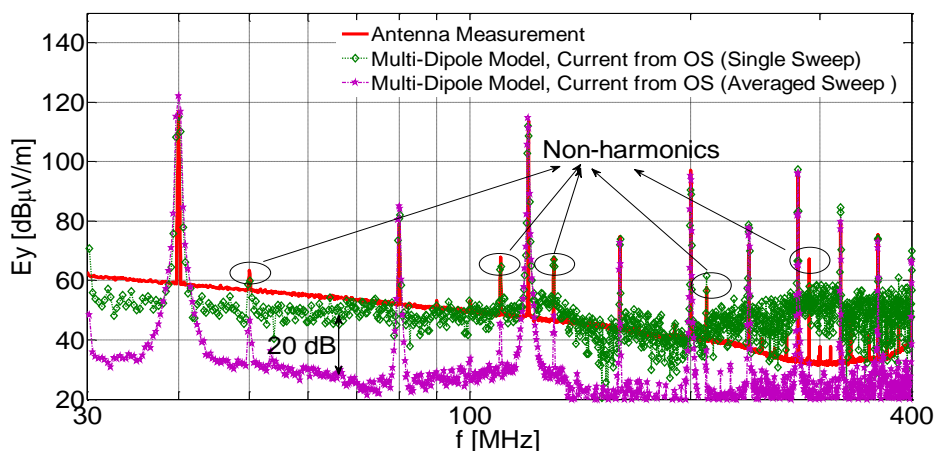


**Figure 3.30** Electric field from the antenna measurement and the multi-dipole radiation model based on cable current scanned by the oscilloscope (OS) with single sweep and averaged sweep
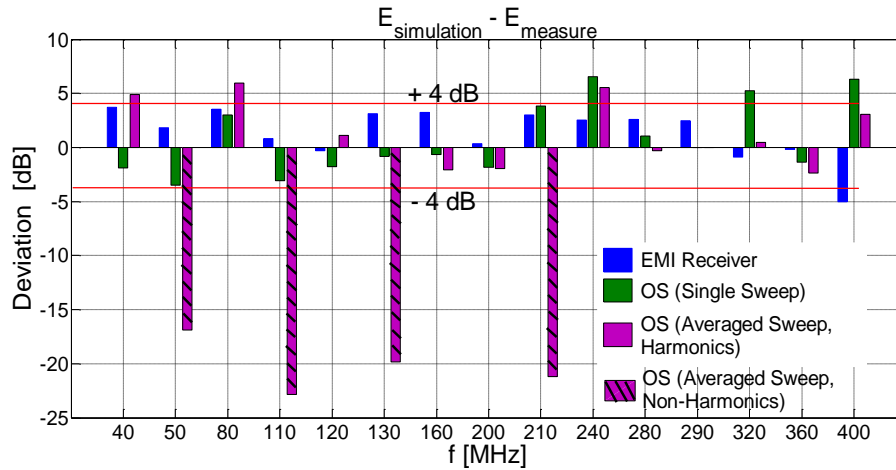
**Figure 3.31** Deviations of calculated field at the main 14-frequency peaks based on the current scanned by the EMI receiver and the oscilloscope (OS) compared with the antenna measurement

## 3.4.3  Cable Bundle with Seven Wires

The proposed current scan methods in frequency- and time-domain are also applied to a more complex cable bundle with seven wires. Simulation and test configuration is similar to the shown twisted-pair cable case above (Figure 3.22). However, the twisted-pair cable is replaced by a cable bundle with seven wires, which are terminated by resistors randomly, as summarized in Table 3.1:

**Table 3.1** Terminals of the cable bundle in the source and load box

|  | Source Box | Load Box |
|---|---|---|
| Cable 1 to GND | Feeding(50 Ω) | 50 Ω or "open" |
| Cable  2 to GND | 47 Ω | 100 Ω |
| Cable  3 to GND | 100 Ω | 47 Ω |
| Cable  4 to GND | 10 Ω | 15 kΩ |
| Cable  5 to GND | 15 kΩ | 10 Ω |
| Cable  6 to GND | 47 Ω | 100 kΩ |
| Cable  7 to GND | 1 kΩ | 47 Ω |

The real parasitic capacitances and inductances of these resistors are not considered in simulation. The fed cable is driven by port 1 of VNA; and the RF current probe is connected to port 2 to measure the common-mode current amplitude and phase distribution. Two cases of terminals attached to the fed cable are investigated: a 50 Ω-resistance and an "open" respectively. A corresponding MoM model is also constructed. In the MoM model, the cable bundle is divided into 100 segments, and the common-mode current on each segment is the sum of currents at the seven wires in this segment. Based on the common-mode current amplitude from the MoM data, current phase on each segment can be retrieved accurately by the proposed algorithm. Furthermore, using the current amplitude and phase, the electric fields can be simulated by the multiple-dipole model and mirror theory. Figure 3.32 shows the electric field in the *y*-direction at the observation point. Compared with MoM, it is obvious that the proposed current phase retrieval method with multi-dipole method can predict the radiated field accurately.
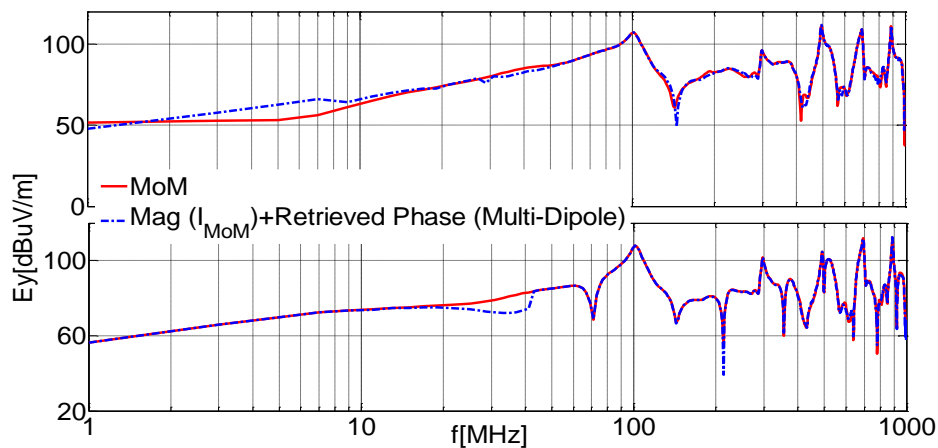


**Figure 3.32** Electric field at the observation point by the MoM and the multi-dipole model with retrieval phase from 1 MHz to 1 GHz, when the fed cable with loads of a 50 Ω (upper) and "open" (lower)

As well as the phase is retrieved based on the common-mode current amplitude of MoM data, we also calculate the phase from the measured current amplitude data. Figure 3.33 shows the electric field at the observation point when the fed cable terminated by a 50 Ω and an "open" loads. The solid curve is the field calculated straightforwardly by the measured current amplitude from the VNA. And the dashed curve is the electric field calculated by the measured current amplitude and the retrieved phase based on the amplitude measurements. As mentioned above, the discussed low frequency problem from retrieved phase can also be observed here; especially below 4 MHz in the case of the 50 Ω load (Figure 3.33 (upper)). This error is due to the high sensitivity of the multiple-dipole radiation model to the phase deviation, which means a small deviation of the retrieved phase might lead to a big

deviation in the final electric field calculation. Furthermore, a field difference can be observed between the electric field calculated by the MoM current (Figure 3.32) and by the measured current in Figure 3.33. This difference can be ascribed to the fact that the experimental terminal box comprises of a parasitic capacitance and inductance, which is far more complex than the pure resistance of Table 3.1 adopted in the MoM Model. However, it does not influence the accuracy of the proposed phase retrieval method; because one advantage of this method is that it does not require the terminal information.
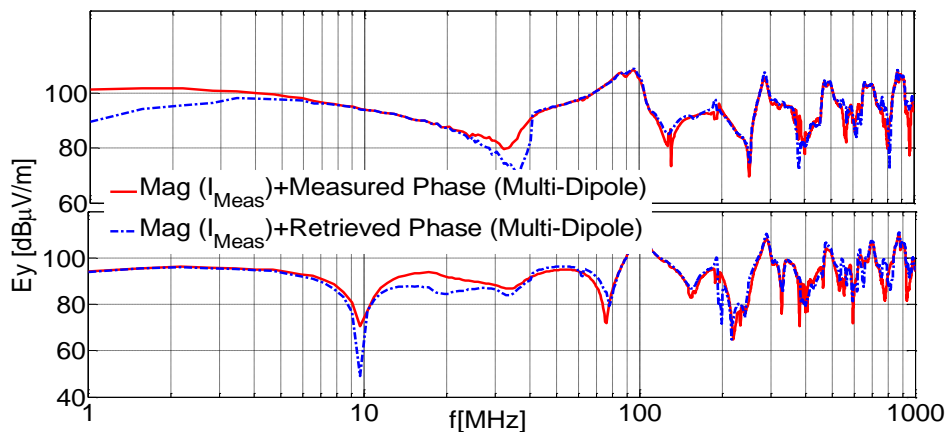


**Figure 3.33** Calculated electric field when the phase is measured and retrieved from 1 MHz to 1 GHz, when the fed cable with loads of a 50 Ω upper) and "open" (lower)

In order to verify both the frequency- and time-domain current scan methods, the source cable is also driven by a voltage pulse, with frequency of 40 MHz and peak-peak value of 5 V. The fed cable is terminated by a 50 Ω resistance. And the same settings of the EMI receiver and the oscilloscope for the twisted-pair cable above are applied here. Current amplitude and phase distribution at different frequencies acquired by the EMI receiver and the oscilloscope are shown in Figure 3.34, for example distributions at 40 MHz, 120 MHz, and 200 MHz. Y-directional electric field at the observation point, depicted in Figure 3.22, is calculated from the scanned currents. Figure 3.35 presents the comparison of the simulation results and the antenna measurement.

In general, the two current scanning methods can achieve high accuracy. At the main radiated frequency peaks (10 harmonics for integral multiples of 40 MHz and 1 non-harmonic (290 MHz)), the field deviation from current scanning using the EMI receiver is less than 4 dB. As discussed in the examples above, there are more factors influencing the accuracy of time-domain current scan method, due to the additional data processing steps. Each step may introduce deviations and uncertainties which are accumulated in the radiation prediction. Figure 3.36 presents

the deviations of the predicted electric field by the current scan methods compared with the direct antenna measurement, using different oscilloscope settings [76]: (1) Single sweep and Rectangle-window of FFT; (2) Single sweep and Hamming-window of FFT; (3) Averaging 200-sweep and Hamming-window of FFT. The average prediction deviations at all frequency-components for the three different settings are 4.33 dB, 2.85 dB and 4.43 dB. However, the maximum deviation amounts to 6 dB, 5.3 dB and 7.6 dB respectively, as shown in Figure 3.36. This means that the setting (2) can achieve higher accuracy. For the first setting of the oscilloscope, the relative higher side-lobe effect of FFT Rectangle-window might lead to errors at some frequencies when currents are low. And it further leads to errors of radiated field, for example 160 MHz and 320 MHz (even harmonics of the fundamental frequency). For the third setting of oscilloscope, averaging sweeps might distort the original non-periodic time-domain signal and it further leads to amplitude and phase distortion in the frequency domain after FFT transformation [77], although it can reduce the noise floor significantly.

From results in Figure 3.36, it can also be seen that the field calculation based on time-domain current scan method shows lower accuracy than the frequency-domain current scan method. Except for the common influence factors in the field prediction, instability of the current phase measurement by FFT is another possible major reason, especially for weak signals. For example, current amplitudes acquired by the oscilloscope show high stability at 40 MHz, 120 MHz and 200 MHz, as they are at least 10 dB higher than the sensitivity limit from the oscilloscope, as shown in Figure 3.34 (left). However, phase ripples can also be observed at 120 MHz and 200 MHz in Figure 3.34 (right). This may be the reason that the fields at these main radiated peaks have a 2.5 dB higher error than predicted fields based on the frequency-domain current measurement. Additionally, a problem in the time-domain measurement often occurs, that the current spectrum is distorted by the inappropriate sweep time and trigger condition. This problem can be avoided in the frequency-domain measurement.
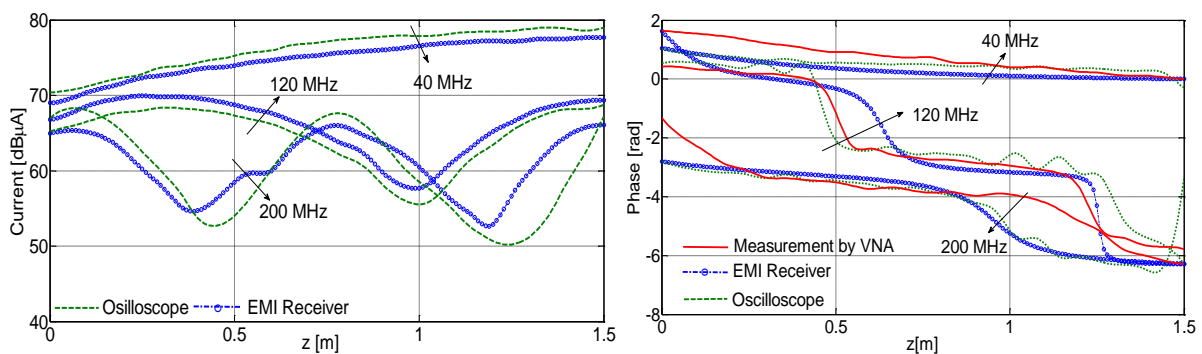


**Figure 3.34** Current distribution scanned by the EMI receiver and oscilloscope (OS)
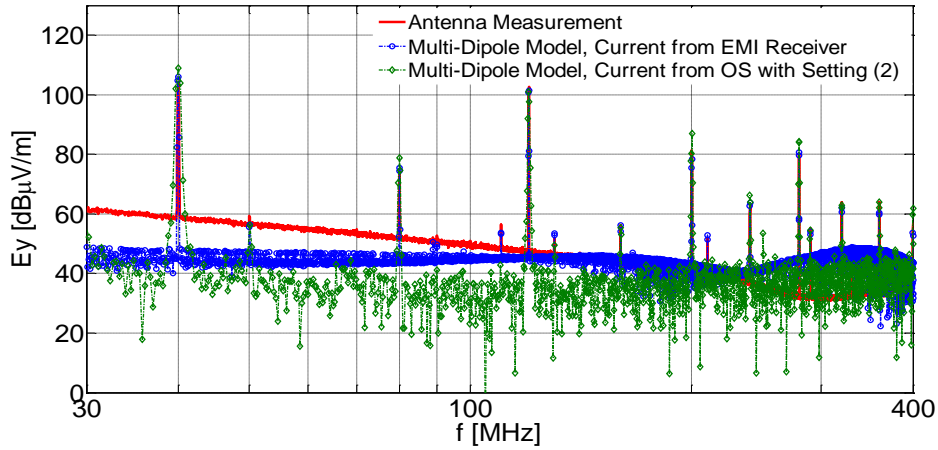
**Figure 3.35** Electric field from the antenna measurement and the multi-dipole model based on the cable current scanned by the EMI receiver and the oscilloscope (OS)
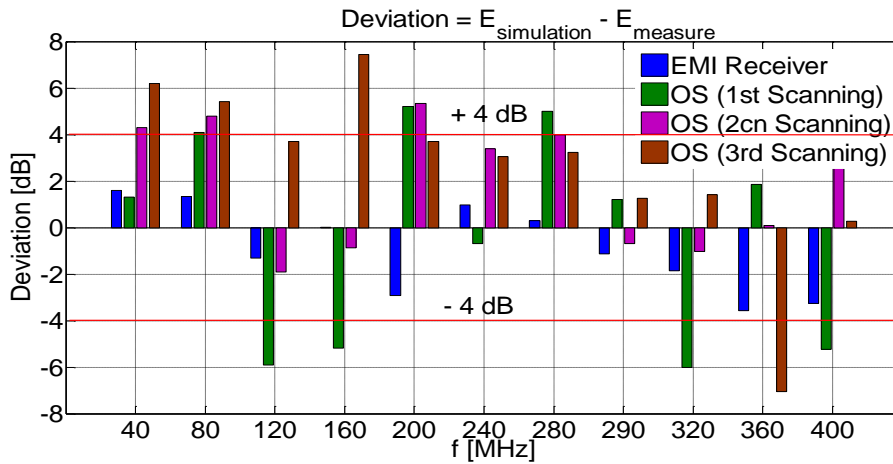


**Figure 3.36** Deviations of calculated field at main 11-frequency peaks based on the cable current scanned by the EMI receiver and the oscilloscope (OS) compared with antenna measurement

In order to investigate the low frequency range from 150 kHz to 30 MHz, a voltage pulse of 100 kHz and 5 V peak-peak value is used to drive the fed wire of the cable bundle. For improving the measurement accuracy and avoiding a weak coupling effect at low frequencies, a CISPR 25 compliant active Rod antenna of 1 meter length is used. Figure 3.37 presents the envelop curves of the electric field from measurement and field simulations based on cable current acquired by the EMI receiver or oscilloscope. The frequency-domain scan method leads to an apparent error in the field calculation below 30 MHz. As shown in Figure 3.37, there is a big resonance deviation around 7 MHz in the curve based on the current acquired by the EMI receiver, because of the high sensitivity of multi-dipole radiation model to the retrieved phase error at low frequencies. Compared with the frequency-domain current scan method, time-domain current scanned by oscilloscope presents a relative smooth curve in this frequency range, because it can obtain the phase distribution along the cable bundle by direct transformation from time-domain data via

65

FFT. However, below 10 MHz a deviation can also be observed compared with the antenna measurement. Besides the high sensitivity of the multi-dipole radiation model to phase error at low frequencies, the antenna measurement result in Figure 3.37 might include some test errors due to the capacitive coupling between the elevated ground plate and the chamber ground. This well-known problem [18] at low frequencies often occurs in real test configurations of the ALSE method, and it will be discussed thoroughly in next chapter.



**Figure 3.37** Electric field from the measurement of 1 m active Rod antenna, the simulation based on the cable current scanned by the EMI receiver and the oscilloscope (OS) below 30 MHz
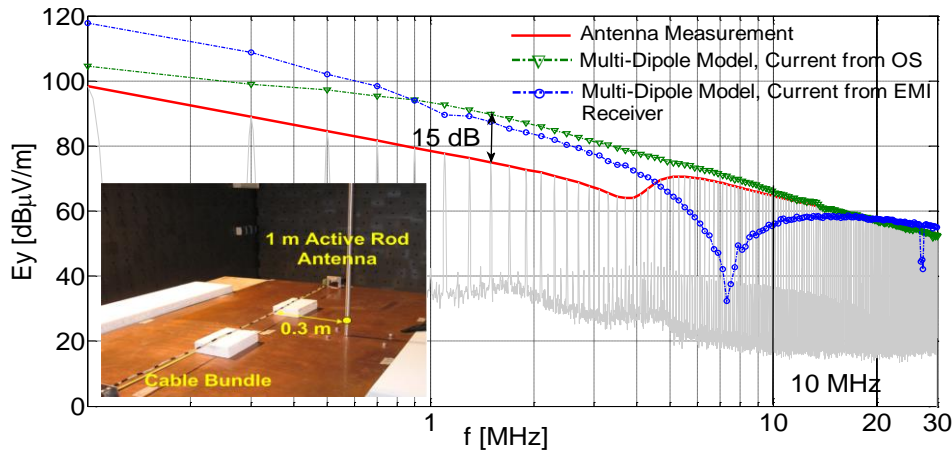
## 3.5  Chapter Conclusion

This chapter has shown the multi-dipole model to predict radiation from a cable bundle. Current distribution as the radiation source can be acquired by proposed current scan methods in frequency domain or time domain. Since the radiation prediction assumes the common-mode current flowing along an equivalent single path as shown in Figure 2.2. The presented simulations have shown that assuming the axial center of the cable bundle is accurate enough to represent the cable radiation in the model, as long as the cross-sectional radius of the cable bundle is less than 1 cm, which only introduces less than 2 dB field error in the worst case. Below a 1 cm cross-sectional radius of a cable bundle, it is also reasonable to ignore contributions from the differential-mode currents in the radiation calculation with respect to the 1 m distant field observation point.

Additionally, in the radiation model for the wire structure as depicted in Figure 3.12, the vertical currents can be approximated by the measured currents at the start and end points of the wire. It can give high accuracy in the vertical field prediction up to 600 MHz and horizontal field prediction up to 1 GHz. Extrapolated approximation based on known transmission line parameters can improve the accuracy up to 1 GHz in both the vertical and horizontal case. Moreover, the length of vertical segments in

66

the radiation model within 1 cm changes only induce less than 2 dB error at the vertical and horizontal field peaks, but it has a big influence on the resonance minimums of horizontal field. And the position offset of the vertical segments within 3 cm nearly has no influence on the vertical and horizontal field peaks, but it will induce the frequency shift at most resonance minimums, especially in vertical field component. In real current measurements, the weak common-mode current is often a challenge for current scan methods. Taking into account the wide range of currents along a cable bundle, it is nearly impossible to acquire all the current information, especially around resonance zeros of the current distribution. Two possible solutions can be used to address this problem. In frequency-domain current scanning, the missing current amplitude can be extrapolated based on the transmission line model. In time-domain current scanning, the missing current amplitude and phase both can be reconstructed through an appropriate interpolation function, such as *spline* function, based on the correct current data on other cable positions. However, simulations have revealed that these solutions only work when the missing current amplitude below the sensitivity limit or noise floor $0.3 \cdot SWR$ (dB) or less (SWR is defined by (3.8). Too much deficient current data will lead to the failure of reconstructing complete current amplitude and phase distribution.

Several cable bundles have been used to verify the proposed current scan methods and multi-dipole radiation model. From these analysis results, frequency-domain scan method can provide good prediction accuracy using an EMI receiver with a considerable low noise level. The retrieved phase can match well with the measured phase distribution using the special optimal algorithm up to 1 GHz. However, the predicted electric field might lead to a great deviation below 30 MHz based on the retrieved phase. The lower the frequency is; the bigger the field deviation is. This reason could be ascribed to the high sensitivity of the multiple-dipole radiation model to the phase error at low frequencies. Compared with frequency-domain scan method, time-domain scan method derives current amplitude and phase via FFT from time-domain data. This FFT based current as the radiation source can also achieve good prediction accuracy in the radiation calculation. However, due to the FFT algorithm and sensitivity limits from the oscilloscope, this method often suffers from more instabilities and uncertainties.

The investigations in this chapter have verified the proposed current scan methods and multi-dipole radiation model of a cable bundle. However, when taking into account the real ALSE test method, the horizontal polarization, the receiving antenna, the finite ground plate and the anechoic chamber have to be considered in an alternative of the radiation estimation. Therefore, next chapter will develop the current scan methods to predict radiation, considering the real ALSE test configuration and environment.

# 4 Predicting Radiation of CISPR 25 Compliant ALSE Configurations

To be a promising low-cost alternative to full-compliance ALSE method, current scan methods must consider more real aspects in the radiation prediction. The elevating finite ground plate used in the ALSE method cannot be modeled by mirror theory, due to the existence of edge currents and reflections [18]. Therefore, a more accurate radiation model for the finite ground plate is needed. Additionally, the complicated ALSE test environmental factors [33]-[36], such as reflections from imperfect absorber walls, the behavior of real test antenna, losses of connection cables, and so on, also need to be considered in a new test alternative.

In order to simulate the finite ground plate, this chapter proposes several possible models. Besides the commonly used model with mirror theory, the edge current model depicted in Figure 1.12 and the surface current model depicted in Figure 1.13 are both applied. MoM-based models for the ALSE test configuration are also constructed. These models are compared and discussed. However these ideal simulation models are difficult to achieve high prediction accuracy if considering real test environment. Accordingly, a calibration procedure based on ALSE measurements is proposed to correct the field calculation based on current scan methods. Several improvements are also recommended to enhance the repeatability and stability of this calibration procedure. In order to verify the proposed improved radiation model and calibration procedure, a cable bundle with seven wires and a general stepper motor drive system are investigated. Additionally, considerations about the radiation from the EUTs and the currents correlated to radiation limits in CISPR 25 are discussed in this chapter.

## 4.1 Modeling Radiation of Finite Ground Plate

### 4.1.1 Mirror Theory and Edge Current Model

Mirror theory can only simulate the influence of infinite ground. However, in a real ALSE test configuration the ground plate is finite which has a large influence on the radiation characteristics from 30 MHz to 1GHz, due to the plate edge currents and edge reflections. Edge current model [52] according to (1.21) - (1.22) is a possible solution, which can approximately calculate the current distribution on both left and right edges through multiplying the available wire current by the defined coefficients. Aside from edge currents, the return currents are represented approximately by the mirror currents, as shown in Figure 4.1. In order to verify the edge current model for the finite ground, the wire configuration above a finite plate in

Figure 4.1 (left) is constructed by MoM. This configuration refers to the ALSE set-up, where the field observation point is 1 m distant to the wire center.
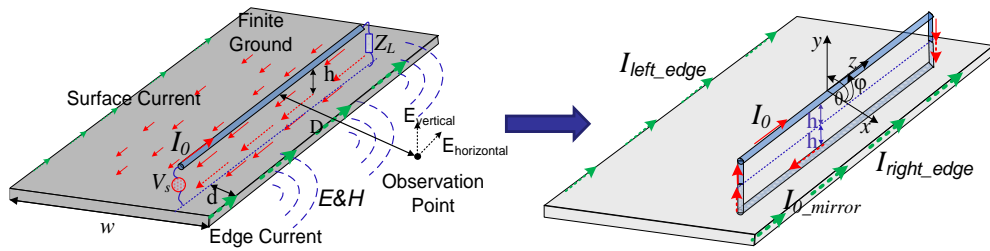


**Figure 4.1** Equivalent mirror and edge current model for the radiation emissions of a wire above a finite ground plate

Electric fields at the observation point are calculated by the proposed edge current model and the MoM model respectively. And the wire in the edge current model calculation adopts the proposed multi-dipole radiation model, which has been verified in last chapter. The current distribution on the wire is exported from MoM simulation, in which the voltage source is $V_s$ = 1 V and the load is $Z_L$ = 50 Ω. Figure 4.2 presents the vertical electric field simulated by MoM, mirror model and edge current model from 30 MHZ to 1 GHz. It can be observed that the result from mirror model matches well with MoM when the ground is infinite, and it is approximate 6 dB higher at resonance peaks than the field result of finite ground. The edge current model can obtain high accuracy in the vertical electric field calculation. Figure 4.3 also compares the electric field in horizontal polarization from different models. These results clearly show the influence from the finite ground plate on electric horizontal field. Approximately 20 dB to 25 dB is enhanced by the finite ground plate. A simple mirror model can simulate both the vertical and horizontal field accurately when the ground is infinite. However, edge current model can only simulate the vertical field when the ground is a finite plate.
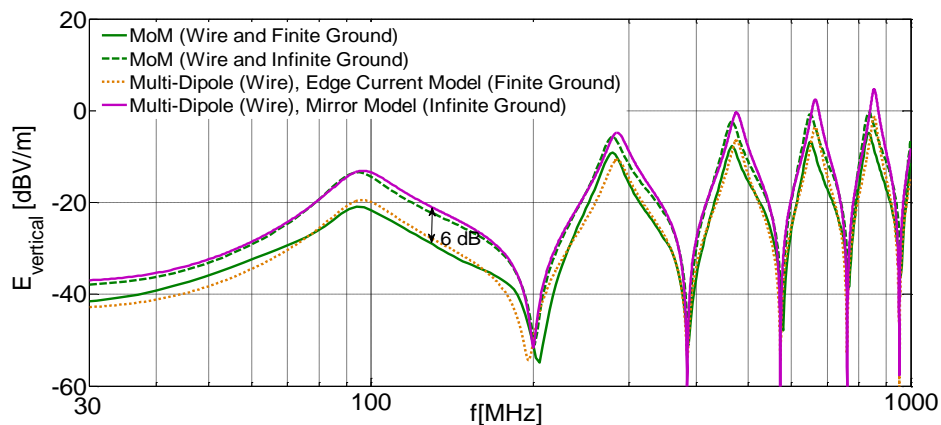


**Figure 4.2** Vertical electric field at the observation point from the mirror model (the wire uses multi-dipole model), the edge current model (the wire uses multi-dipole model) and the MoM model
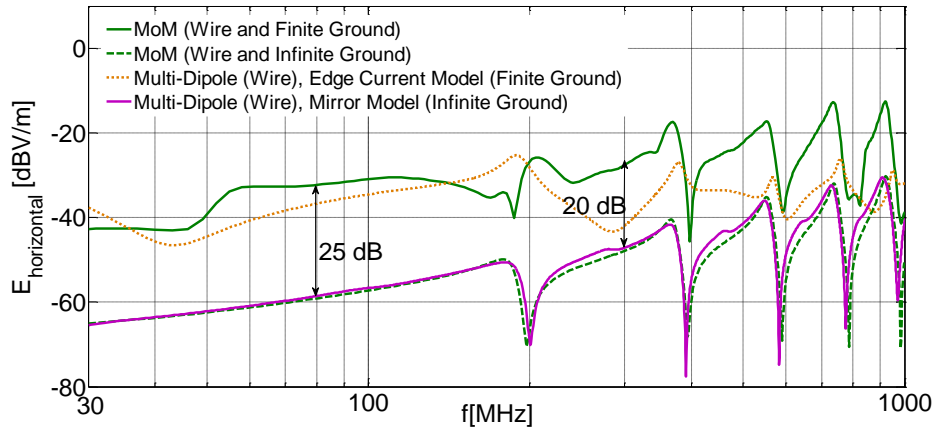
**Figure 4.3** Horizontal electric field at the observation point from the mirror model (the wire uses multi-dipole model), the edge current model (the wire uses multi-dipole model) and the MoM model

## 4.1.2  Surface Current Model

To simulate the influence of finite ground plate more accurately, surface current model based on the equivalence theorem is introduced. Basic idea of this model is to use equivalent surface currents to represent the finite ground. The equivalent surface current density $J(s)$ on the finite ground are assumed to be the density of surface current on an infinite ground, but restricted to the actual area of finite ground [53]. According to (1.23), $J(s)$ can be calculated. In order to get the radiation from the equivalent surface current, a number of electric dipoles represent the surface currents on the metal plate. These elements have to be arranged in a grid structure, as shown in Figure 4.4:



**Figure 4.4** Replacement of finite ground plate by equivalent surface current model

Here surface current density can also be rewritten by:

71

$$\begin{aligned}
\boldsymbol{J}(s) &= J_x \boldsymbol{e}_x + J_z \boldsymbol{e}_z \approx \boldsymbol{e}_y \times (\boldsymbol{H}^{TL}(s) + \boldsymbol{H}^{TL\_mirror}(s)) \\
&= -H_z \boldsymbol{e}_x + H_x \boldsymbol{e}_z
\end{aligned} \tag{4.1}$$
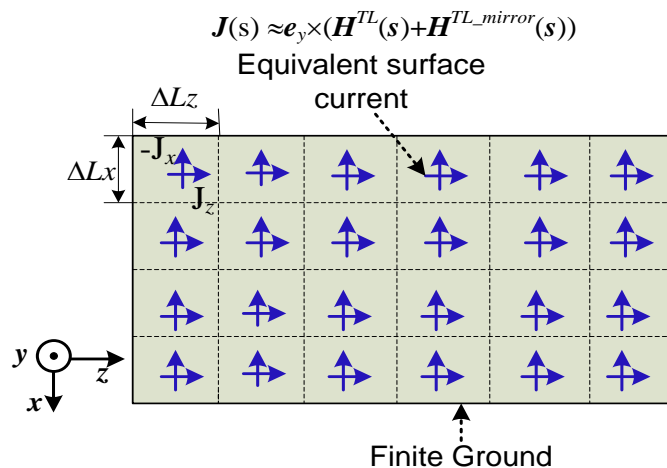
Where $\boldsymbol{e}_y$ is the unit vector normal to the finite ground surface as shown in Figure 4.4, $\boldsymbol{H}^{TL}(s)$ is the magnetic field originating from common-mode current of a cable bundle above the ground plate; while $\boldsymbol{H}^{TL\_mirror}(s)$ originates from the mirror current based on mirror theory. Accordingly for each grid, the equivalent current on the electric dipole can be approximated by:

$$I_{dipx}\boldsymbol{e}_x = \Delta L_z \cdot J_x \boldsymbol{e}_x \qquad I_{dipz}\boldsymbol{e}_z = \Delta L_x \cdot J_z \boldsymbol{e}_z \tag{4.2}$$

Associated with multiple-dipole model, the field due to the induced surface currents on the finite ground can be calculated. $I_{dipx}\boldsymbol{e}_x$ on the plate, for example, produces the $y$-direction electric field $E_y^P$:

$$E_y^P = \sum_{k=1}^{N} \frac{I_{dipx}^k \Delta L_x^k \cdot (z-z_k)(y-y_k)}{4\pi r_k^2} \eta_0 \beta_0^2 (j\frac{1}{\beta_0 r_k} + \frac{3}{\beta_0^2 r_k^2} - j\frac{3}{\beta_0^3 r_k^3}) e^{-j\beta_0 r_k} \tag{4.3}$$

Where $N$ is the number of grid elements on the finite ground, $r_k$ is the distance from the grid center $(x_k, y_k, z_k)$ to the observation point $(x, y, z)$, and $\Delta L_x^k$ is the grid length along $x$-direction. After discretization of the cable bundle and finite ground by a set of electric dipoles, the total radiated field from the cable bundle above a finite ground plate ($\boldsymbol{E}^{\text{Total}}\&\boldsymbol{H}^{\text{Total}}$) can be calculated as the sum of two components in (4.4): the field from the cable bundle in the absence of the plate ($\boldsymbol{E}^{\text{TL}}\&\boldsymbol{H}^{\text{TL}}$), and the field from the finite ground plate in the absence of the cable bundle ($\boldsymbol{E}^{\text{P}}\&\boldsymbol{H}^{\text{P}}$). The illustration is depicted in Figure 4.5.

$$\begin{aligned}
\boldsymbol{E}^{\text{Total}} &= \boldsymbol{E}^{\text{TL}} + \boldsymbol{E}^{\text{p}} \\
\boldsymbol{H}^{\text{Total}} &= \boldsymbol{H}^{\text{TL}} + \boldsymbol{H}^{\text{p}}
\end{aligned} \tag{4.4}$$

To verify the surface current model for the finite ground plate, vertical and horizontal fields at the observation point in Figure 4.1 (left) are calculated by the proposed model and MoM, as shown in Figure 4.6. The wire in surface current model calculation adopts the multi-dipole radiation model, on which the current distribution is exported from MoM simulation. It can be seen that the vertical electric field from surface current model matches very well with the result from MoM. Horizontal field can achieve high accuracy in a wide frequency range, with the exception of the range from 150 MHz to 220 MHz. This deviation might be caused by the limitation of surface current model, which assumes the ground plate is infinite in the calculation of surface currents.

Besides the field at the observation point with 1 m distance, the far field radiation pattern ($0° \leq \theta \leq 180°$) on the plane $\varphi = 0°$ with 10 m distance are also investigated, which refers to the spherical coordination system in Figure 4.1 (right). Figure 4.7 shows the radiation pattern at 300 MHz calculated by MoM and surface current model respectively. Also it can be observed from these curves that the finite ground plate has a strong influence on the radiation pattern particularly on $E_\theta$, but less impact on $E_\varphi$. Results from the surface current model are generally in agreement to full-wave MoM. The maximum difference between $E_\theta$ of MoM and the surface current model is approximately 3 dB near $\theta = 60°$. For $E_\varphi$, the difference between $90° \leq \theta \leq 180°$ is relatively larger than $0° \leq \theta \leq 90°$, and the maximum error is about 5 dB near $\theta = 165°$. Main reason for these differences is that the induced edge currents along the plate fringe are not taken into account accurately. The approximated surface current distribution in the proposed model is calculated on the assumption of an infinite ground according to (4.1). However, compared with MoM this simpler model can achieve higher computation efficiency and is easy to program. Simulation time of MoM model is about 29 times larger than the surface current model when using the same simulation environment and the same mesh size for the finite ground plate.
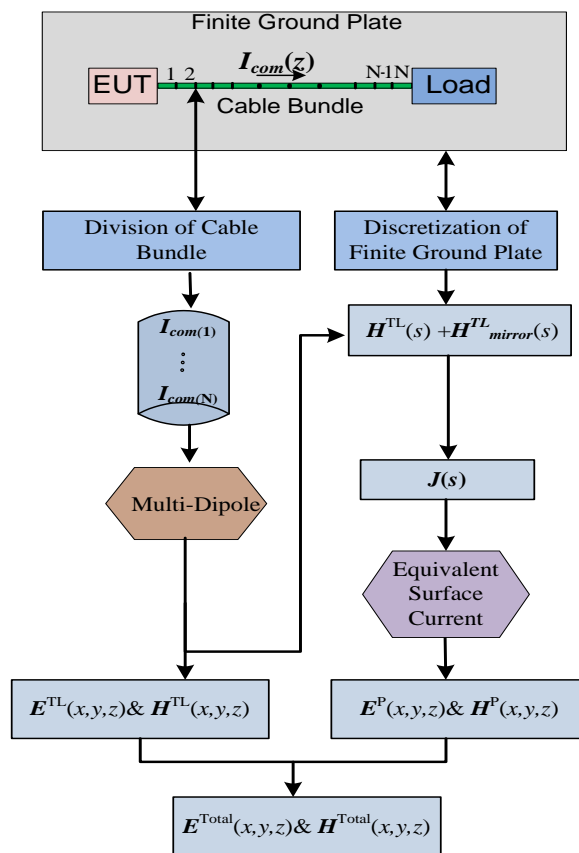


**Figure 4.5** Illustration of radiation models from cable bundle based on the multi-dipole model and finite ground based on the surface current model
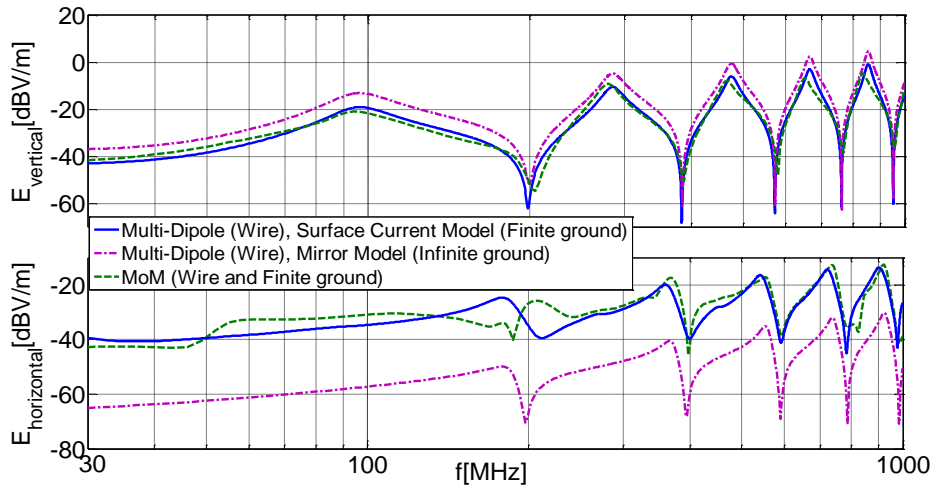
**Figure 4.6** Comparison of electric field in vertical (upper) and horizontal (lower) polarization at observation point between surface current model and MoM model
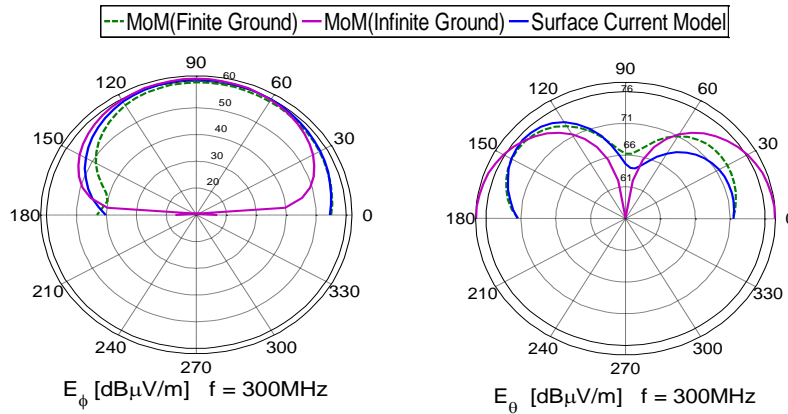


**Figure 4.7** Radiation pattern from the MoM and the surface current model on the plane $\varphi=0^o$ at 300 MHz

## 4.2  Improving Accuracy with Measurement Correction Functions

According to CISPR 25, the ALSE test method must be implemented in an anechoic shielded chamber with a specific test antenna. From 150 kHz to 30 MHz, an active Rod antenna (here SCHWARZBECK VAMP 9243) can be used to measure the vertical electric coupling field; from 30 MHz up to 1 GHz a Bilog antenna (here TESEQ CBL 6141B) can be used to measure both the vertical and horizontal electric field, as shown in Figure 4.8. The proposed simplified and ideal radiation models are problematic due to the complex behavior of the anechoic chamber, where peripheral systems and reflections from the chamber walls can influence the antenna voltage. Thereby it is necessary to take these factors into account. For this purpose a measurements based calibration procedure is proposed.

74

A 1.5 m long single wire, fed by a sinusoidal signal, is used. Then corresponding correction function for the ALSE environment can be obtained:

$$K_C = E_{sim} - E_{antenna} \quad (dB)$$

$$E_{antenna} = V_{antenna} + AF_{antenna}(dB)$$

(4.5)

Here $E_{antenna}$ is the measured electric field, which is the sum of antenna voltage $V_{antenna}$ and the specific antenna factor $AF_{antenna}$. It involves the influencing factors from ALSE environment. $E_{sim}$ is the simulated field at the antenna reference point based on the scanned current data from the measurement configuration model. It involves errors from current data and radiation models. For high accuracy, the measurement equipment and all the coaxial cables in process of current scanning should be maintained similar as in the process of antenna measurement. These correction functions are the fingerprint of a test chamber and will vary from location to location. Therefore calibration procedure needs to be applied in each test chamber to obtain their respective correction functions. This procedure can also be a very useful method to compare different test chambers.
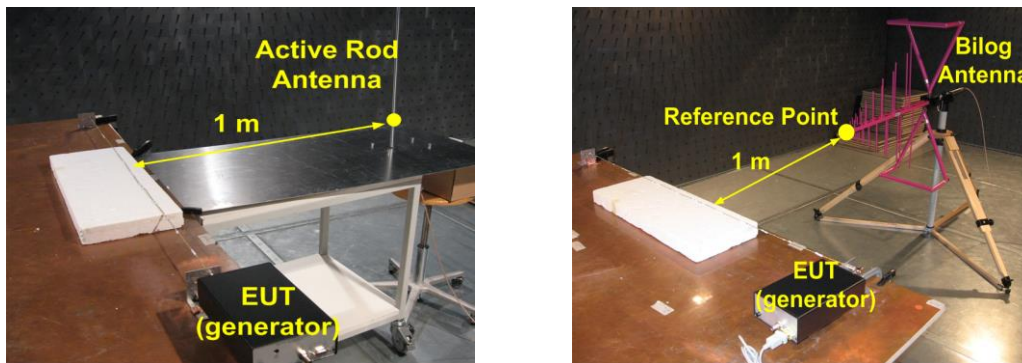


**Figure 4.8** ALSE test configurations for the active Rod antenna (left) and the Bilog antenna (right)

## 4.2.1  Calibration by an Active Rod Antenna below 30 MHz

In the active Rod antenna set-up as shown in Figure 4.8 (left), the active impedance convertor should give a frequency independent coupling factor, due to the high input impedance. However, taking into account the capacitive coupling between metallic table and chamber floor, as well as the inductive coupling from connected coaxial cable to antenna, this coupling factor is no longer a straight line. For example in Figure 4.9, a rise occurs above 2 MHz in the ALSE test configuration, depicted by measurement curve labeled by *ALSE*. When the calibrated wire and active Rod antenna are placed on the chamber floor to remove the capacitive table coupling, this rise cannot be observed anymore as denoted by the measurement curve labeled by *Chamber-Floor*. Some measures could suppress the coupling effects in the ALSE

configuration to guarantee the test accuracy [36], for example adjusting the antenna height or counterpoise grounding. The correction function $K_C$, which describes the deviation between antenna measurement and simulation from 2 MHz to 30MHz, is about 7 dB. Here the simulation is based on multi-dipole model for the wire and mirror model for the ground plate. $K_C$ can be used as a correction function to compensate the error due to capacitive table coupling.
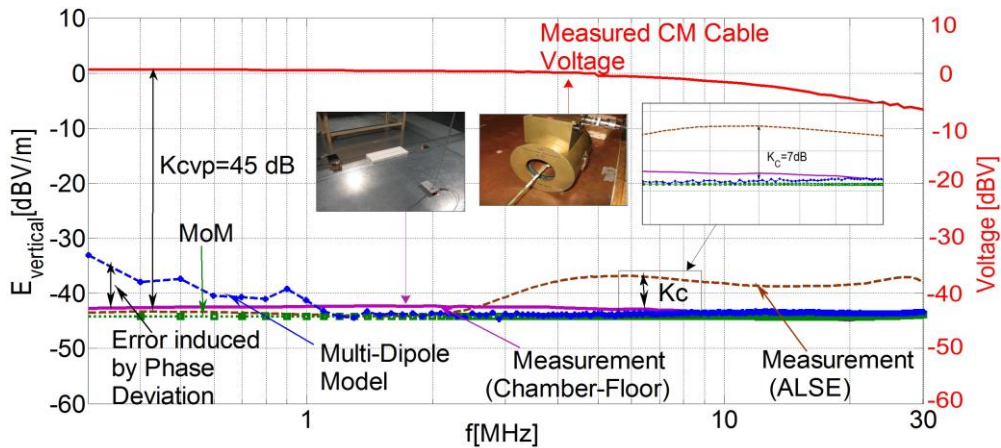


**Figure 4.9** Normalized measured and simulated data from the calibration of active Rod antenna

Below 1 MHz, the simulation curve from the multi-dipole model shows big deviations compared to the measurement and MoM, which originate from the insufficient measured phase accuracy. Figure 4.10 shows the sensitivity of electric field with respect to phase distribution accuracy up to 30 MHz, where electric fields are calculated by multi-dipole model with measured phase from VNA and simulated phase from MoM, respectively. The results show that the sensitivity of multi-dipole model below 1 MHz is up to 150, which is much higher than the sensitivity above 2 MHz. Therefore, this high sensitivity of multi-dipole model at very low frequencies can bring field calculation error, due to the inaccurate phase distribution.



**Figure 4.10** Sensitivity of electric field to the phase distribution

In order to fix this problem, directly measured cable voltage by a Common-mode Voltage Probe (CVP) [80] with known coupling function $K_{CVP}$ can be used as alternative to evaluate radiated field at very low frequencies. The function $K_{CVP}$ between the measured cable voltage and the measured electric field of active Rod antenna is about 45 dB below 5 MHz, and it can be defined by:

$$K_{CVP} = V_{Cable} - E_{Rod-antenna} \, (dB)$$

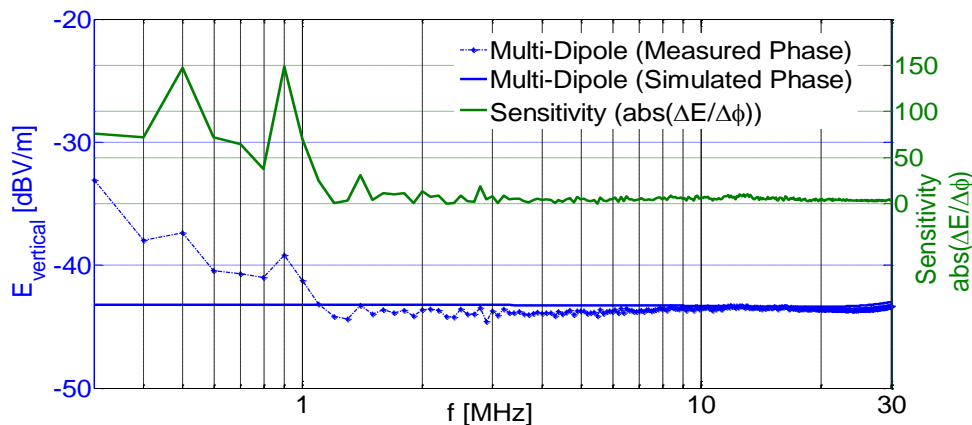$$E_{Rod-antenna} = V_{Rod-antenna} + AF_{Rod-antenna} \, (dB)$$

(4.6)

This coupling function should be constant at low frequencies, but it will vary with different CVPs, active Rod antennas or test sites.

## 4.2.2  Calibration by a Bilog Antenna from 30 MHz to 1 GHz

In the analysis of active Rod antenna below 30 MHz, the mirror currents and multi-dipole radiation model in simulations are accurate enough to model the metallic table in Figure 4.8 (left). However for Bilog antenna used from 30 MHz to 1 GHz, an infinite ground model and mirror theory cannot reflect the influence of the finite metallic plate, especially in horizontal polarization. Therefore, the more accurate surface current model is used. To calculate the correction function with (4.5), the wire current distribution measurement and antenna measurement are both required. Figure 4.11 is the configuration to acquire current amplitude distribution on the single wire in frequency domain. Current acquired in time domain is similar to this configuration, but an extra reference probe is needed.
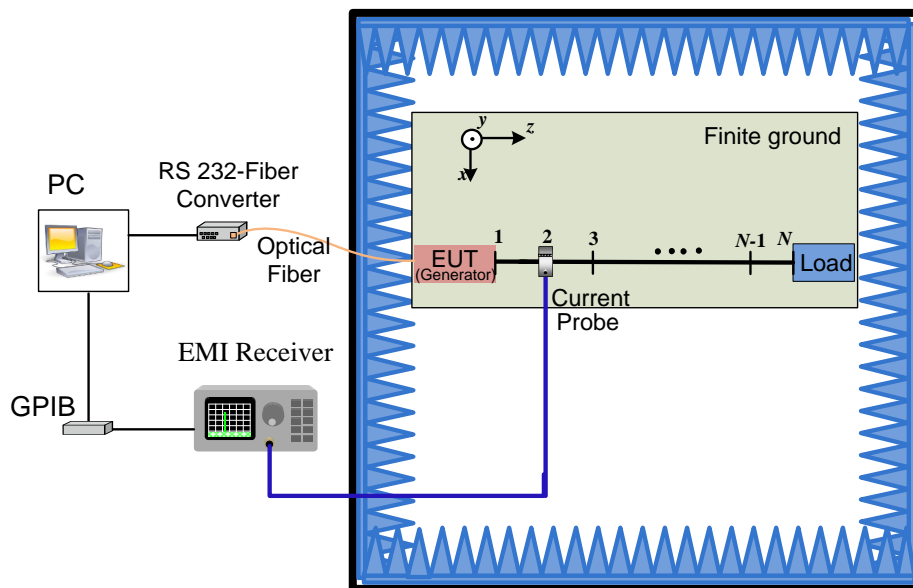


**Figure 4.11** Calibration configuration for the current scan method in frequency domain

Figure 4.12 shows a necessary measure to suppress the non-cable radiation component in the antenna measurement, since the proposed simulation method is based on an assumption that the wire is the main radiating structure. For this reason, a metallic box is used to shield the generator and a semi-rigid coaxial cable is connected from generator to the wire. However, a small common-mode current $I_{CM}$ along the semi-rigid coaxial cable might still exist, which can be damped through a ferrite.
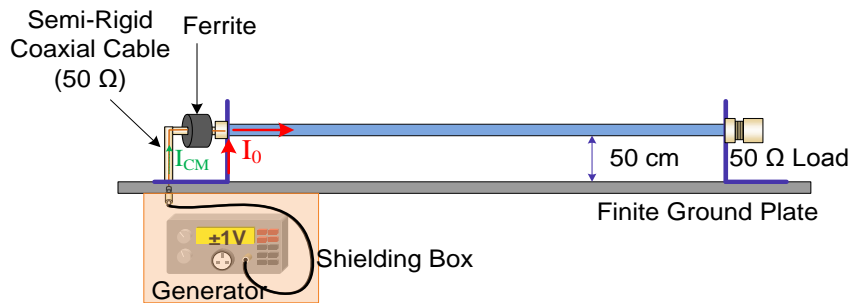


**Figure 4.12** Generator in a metallic box to prevent its field emission in the calibration procedure

In the calibration of the Bilog antenna using frequency-domain current scan method, the wire current amplitude distribution is measured by an EMI receiver and the phase distribution is retrieved by proposed retrieval algorithm. Then they are applied to calculate electric fields at reference point depicted in Figure 4.8 (right), based on multi-dipole radiation model for the wire and surface current model for the finite ground plate. Figure 4.13 shows the vertical electric field from direct antenna measurements, proposed simulation methods, and MoM. $K_C$ denoted in plot is the correction function according to equation (4.5), representing the deviation between the simulated field based on scanned current and the measured field directly from Bilog antenna. Also horizontal field at reference point is calculated as shown in Figure 4.14. Compared with the vertical component, the horizontal component in measurement is more sensitive to the configuration, especially at high frequencies. As mentioned above, the horizontal field deviation that originates from the surface current model from 150 MHz to 220 MHz in Figure 4.6 (lower) is also corrected by the function $K_C$. From 30 MHz to 40 MHz, there is a relatively high deviation of the horizontal field, which comes from the same low-frequency problem as multi-dipole radiation model of a cable bundle. Since the equivalent surface current on the finite ground in the surface current model is represented by electric-dipole arrangements as shown in Figure 4.4, this approximation is also sensitive to current phase error at low frequencies. However this deviation can also be corrected by $K_C$. Compared with

the result of MoM, the measured horizontal field curve is distorted above 500 MHz, which might come from the influence from the coaxial test cable of antenna and the imperfect absorber walls.

**Figure 4.13** Measured and simulated vertical field from the calibration configuration based on the scanned current by the EMI receiver

**Figure 4.14** Measured and simulated horizontal field from the calibration configuration based on the scanned current by the EMI receiver

Likewise, calibration of the Bilog antenna using time-domain current scan method is implemented with the same procedure. But current amplitude and phase along the calibrated wire are both acquired from an oscilloscope and FFT transformation. Correction factor $K_C$ calculated by (4.5) involves not only the test environment influencing factors, but also the algorithm deviations from FFT. In the calibration procedure, the reference probe can be adopted as another current probe or voltage probe. However it shall be ensured that the used oscilloscope is triggered correctly in the whole scanning process. As expected, the vertical field from simulation based on the time-domain measured current shows good agreement with measurement, as shown in Figure 4.15. However, the horizontal field difference

between simulation and measurement is apparent especially at high frequencies, as shown in Figure 4.16.



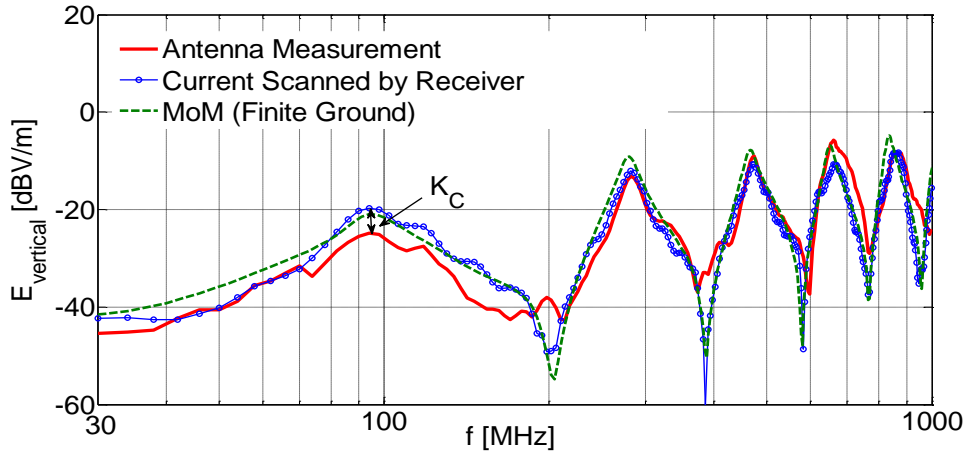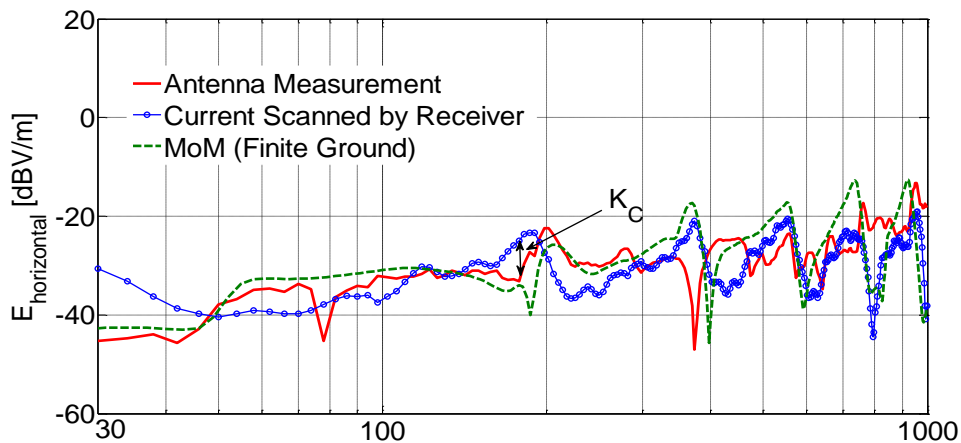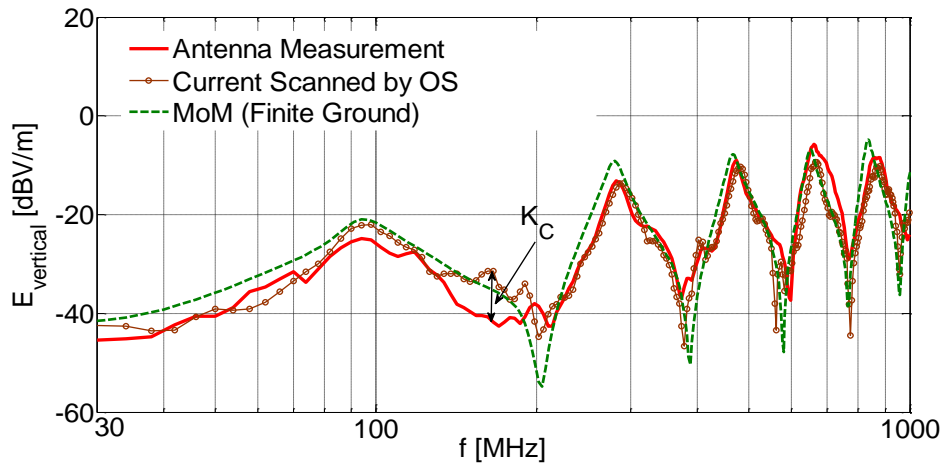**Figure 4.15** Measured and simulated vertical field from the calibration configuration based on the scanned current by the oscilloscope (OS)
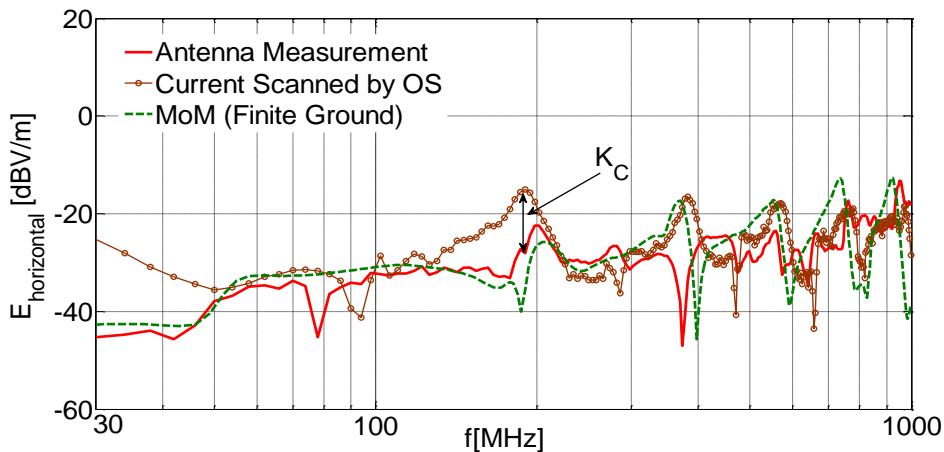


**Figure 4.16** Measured and simulated horizontal field from the calibration configuration based on the scanned current by the oscilloscope (OS)

## 4.2.3  Load Dependence of Correction Functions

In the calibration procedure shown above, the single wire is terminated by a 50 Ω load. Correction function is nearly a constant with different loads in the active Rod antenna calibration. However, in the Bilog antenna calibration the correction function varies with different loads over frequency resonance minimums. Therefore, different loads terminated at the calibrated wire can obtain a set of correction functions. The average of these correction functions is more reasonable, because the common-mode current on a real cable bundle would encounter complex terminal circumstances at different frequencies. Figure 4.17 and Figure 4.18 present the correction functions with short, open, 1 kΩ loads and their average data in vertical and horizontal polarization, respectively. It can be observed that an apparent difference in correction functions due to different loads occurs around 200 MHz, 400

MHz, 600 MHz, 800 MHz and 1000 MHz in vertical polarization, which are also around resonance minimums in vertical electric field curve as shown in Figure 4.13; whereas apparent difference occurs around 100 MHz, 180 MHz, 300 MHz, 500 MHz, 550 MHz and 900 MHz in horizontal polarization.
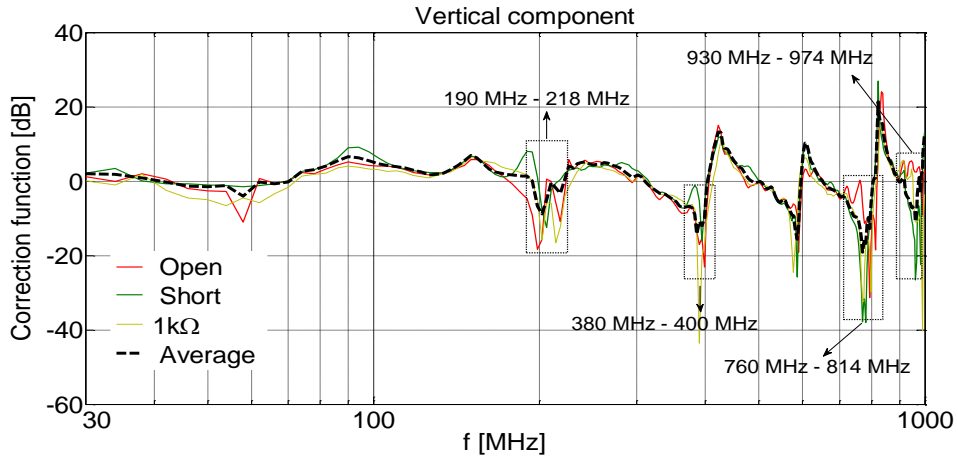
**Figure 4.17** Correction functions in the vertical polarization
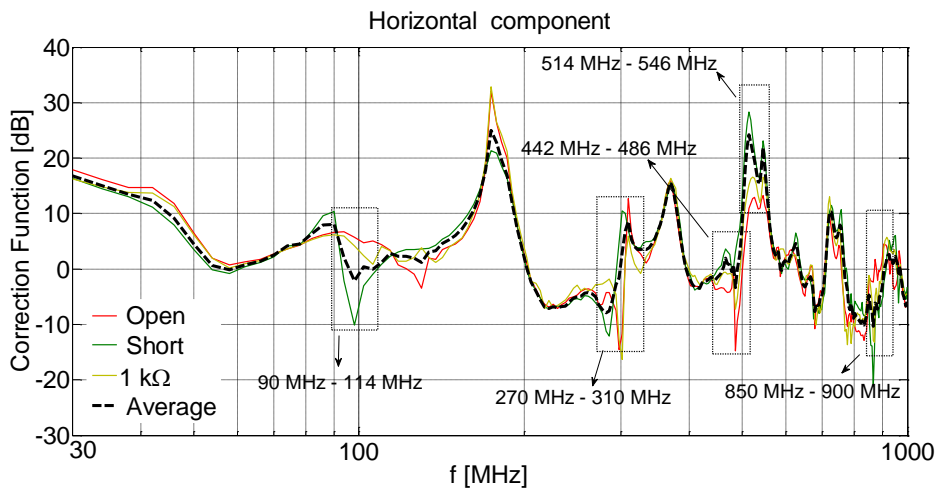
**Figure 4.18** Correction functions in the horizontal polarization

# 4.3  Application and Validation Considering  ALSE Configurations

In order to verify the proposed simulation methods considering real ALSE environments, the same cable bundle with seven wires in the last chapter is used. But the vertical and horizontal electric fields are both simulated based on current scan methods, radiation models and correction functions, to get the comparable results with ALSE method. In the measurement of seven-wire cable bundle, the source is a regular pulse, which might differ from disturbance sources in a real EMC test. Therefore, the proposed methods are also applied to a more complex stepper-motor drive system.

## 4.3.1  Cable Bundle with Seven Wires

Figure 4.19 shows the test configuration according to ALSE method. Fed cable is driven by a 3.3 V digital signal with 40 MHz, of which rising time and falling time are about 2.5 ns. Source wire is terminated by a 50 Ω load, and other wires are terminated according to Table 3.1. In the antenna measurement the reference point of Bilog antenna is 1 m distant to the cable bundle center. The antenna voltage is measured by the EMI receiver (average detector, 120 kHz BW, and 5 ms MT). In the current scan methods, the common-mode currents on the cable bundle are acquired by the EMI receiver with same setting as the antenna measurement, or acquired by the oscilloscope (single sweep, 550 µs sample time, and 0.5 ns interval time). Multi-dipole radiation model for the cable bundle and surface current model for the finite ground are applied to predict the radiated field at the reference point of Bilog antenna. After correcting these predicted results using the available correction function, the comparisons between the direct antenna measurement and the simulation are depicted in Figure 4.20 (vertical polarization) and Figure 4.21 (horizontal polarization).
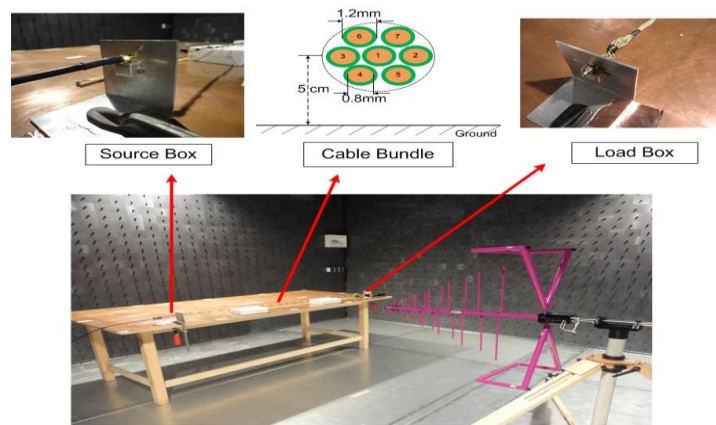


**Figure 4.19** Configuration with seven-wire cable bundle

Figure 4.22 depicts the deviation bar charts compared with the antenna measurement. Twelve main harmonics (integral multiples of the fundamental-frequency 40 MHz) are shown. In vertical polarization, most deviations from the current measured by the EMI receiver are below 4 dB. Deviations from the current measured by the oscilloscope can be less than 5 dB except at 360 MHz. Compared with vertical fields, the calculated horizontal fields show higher deviation. Maximum deviation from simulation nearly amounts to 13 dB at 280MHz and 480 MHz. These two frequency points are also located around the resonances in the horizontal correction function in Figure 4.18, where the horizontal field measured by the Bilog antenna is very sensitive to the small changes in configuration. The proposed averaged correction functions from the calibration procedure can improve the predicted accuracy of current scan methods. For example, the simulation results

including correction functions can improve the accuracy by 1.5 dB ~ 11 dB in the vertical field and 3 dB ~ 13 dB in the horizontal field at main radiation peaks, as shown in Figure 4.23. However, the accuracy of horizontal field at 280 MHz is reduced after adding an unreliable value of 8.3 dB. This frequency is close to 300 MHz, where the correction function is very sensitive to load impedances.



**Figure 4.20** Vertical electric field from the antenna measurement and the simulation based on the cable current scanned by EMI receiver and oscilloscope (OS)



**Figure 4.21** Horizontal electric field from the antenna measurement and the simulation based on the cable current scanned by EMI receiver and oscilloscope (OS)



**Figure 4.22** Deviations of calculated fields based on the cable current scanned by the EMI receiver and the oscilloscope (OS) compared with antenna measurement

83
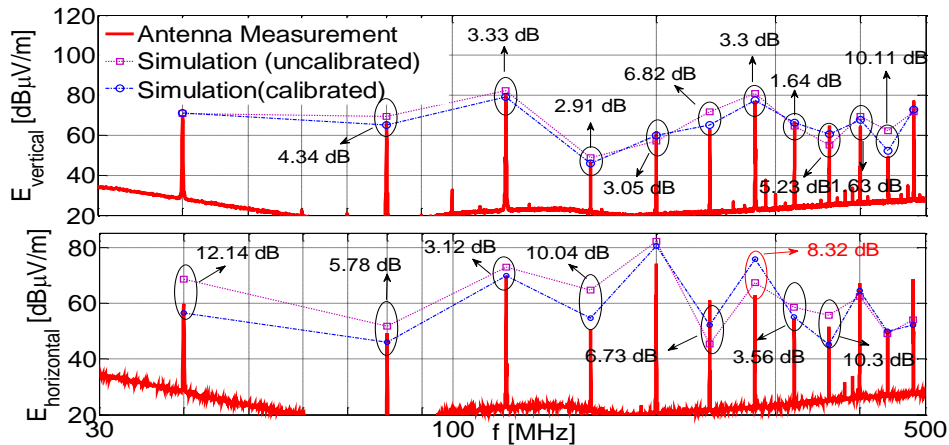
**Figure 4.23** Electric fields from antenna measurement and simulation based on the cable current scanned by the EMI receiver with and without correction functions

## 4.3.2 Stepper-Motor Drive System

Figure 4.24 shows the radiation test configuration with the Bilog antenna (30 MHz to 1 GHz) and the active Rod antenna below 30 MHz. For flexibility in programming, a microcontroller board (Ardunio with16 MHz-clock frequency) with a motor drive board is applied as EUT, which is similar to typical automotive electronic control units. A 20 dB pre-amplifier (Rohde&Schwarz Hz-16) is used to improve the measurement dynamics.
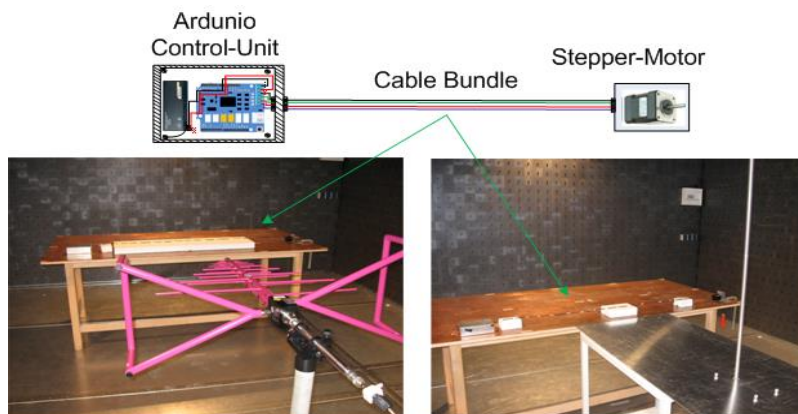


**Figure 4.24** Analyzed configuration of a stepper-motor drive system

EMI receiver (average detector, 120 kHz BW, and 5 ms MT) is used to measure the antenna voltage, and the voltage can be transferred to electric field at the antenna reference point with the antenna factor. Electric fields at the reference point are also calculated based on the acquired cable current by the EMI receiver with same setting as antenna measurement, or by the oscilloscope (single sweep, 550 µs sample time, and 0.5 ns interval time). Figure 4.25 and Figure 4.26 present the predicted fields and antenna measurements from the Bilog antenna in the vertical

and horizontal polarization up to 600 MHz. Radiation above 600 MHz is not presented since there are nearly no radiation peaks. In general, the results at the main radiation peaks in the vertical direction from current acquired by EMI receiver and oscilloscope both can match well with the measurements. Error distribution is shown in Figure 4.27 (upper). At the main harmonic peaks (32 MHz, 64 MHz, 96 MHz, 128 MHz, 288 MHz and 384 MHz), the calculated errors based on scanned current by EMI receiver amount to 5.6 dB, 0.6 dB, 0.6 dB, 1 dB, 1.7 dB and 5.9 dB; while errors based on scanned current by oscilloscope are 6.1 dB, 1.1 dB, 3.1 dB, 1.5 dB, 1.7 dB and 2 dB. Compared with vertical polarization, the horizontal emission includes less radiated peaks. Figure 4.27 (lower) shows the error distribution. At main peaks (32 MHz, 64 MHz, 128 MHz, 192 MHz, 288 MHz and 384 MHz), the errors based on scanned current by EMI receiver are 0.1 dB, 0.4 dB, 3.7 dB, 4.5 dB, 6.5 dB and 1.1 dB; while the errors from scanned current by oscilloscope amount to 5 dB, 2.5 dB, 3.5 dB, 1.1 dB, 3.8 dB and 0.5 dB.
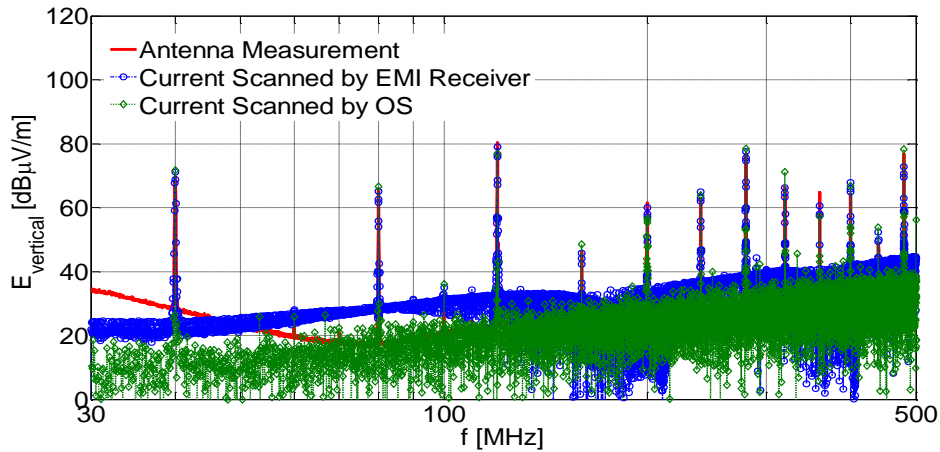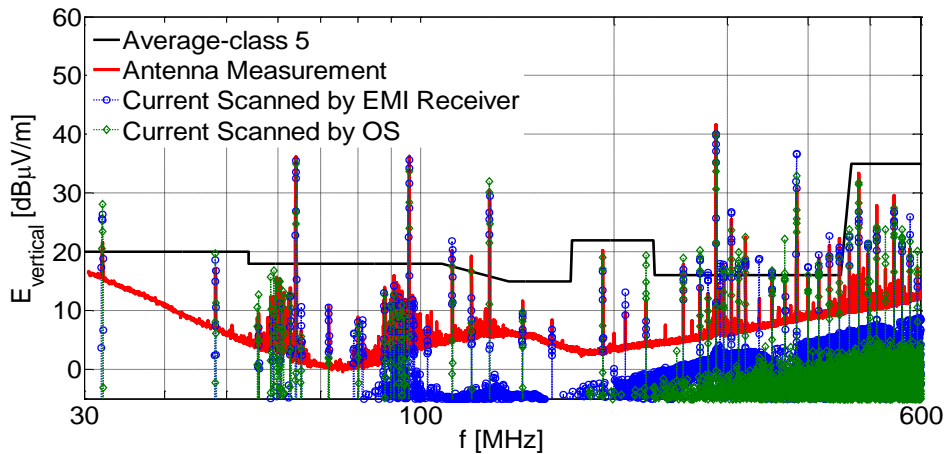


**Figure 4.25** Vertical electric fields from the antenna measurement and the simulation based on the cable current scanned by the EMI receiver and the oscilloscope (OS)
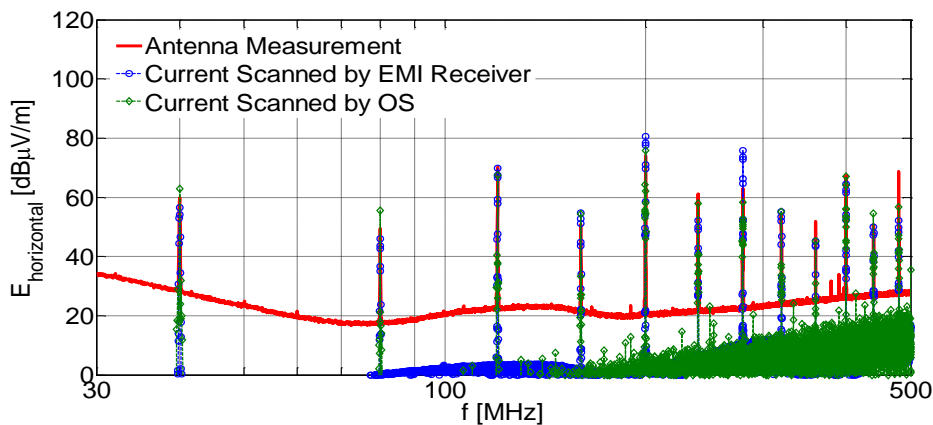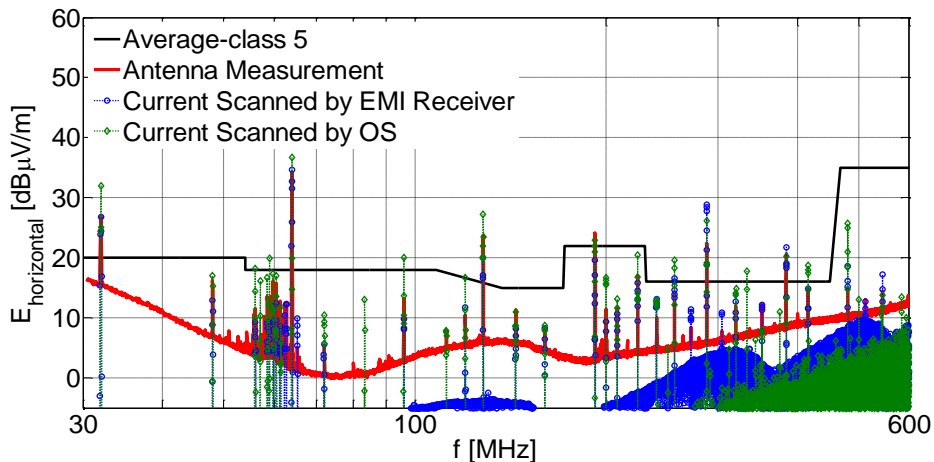


**Figure 4.26** Vertical electric fields from the antenna measurement and the simulation based on the cable current scanned by the EMI receiver and the oscilloscope (OS)
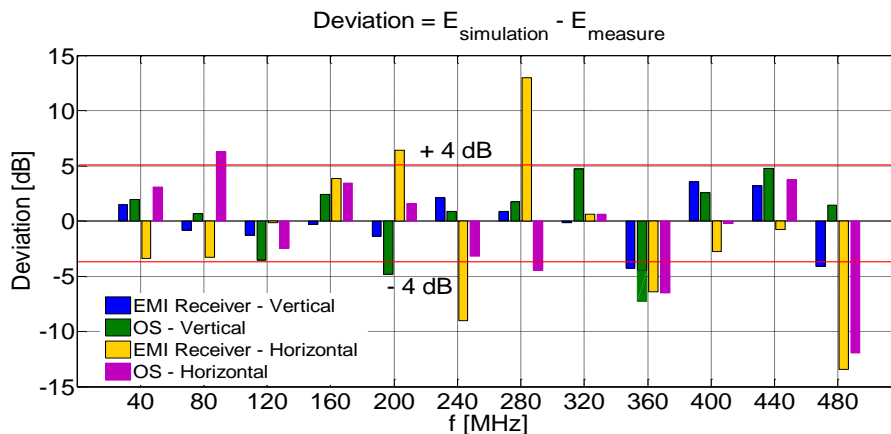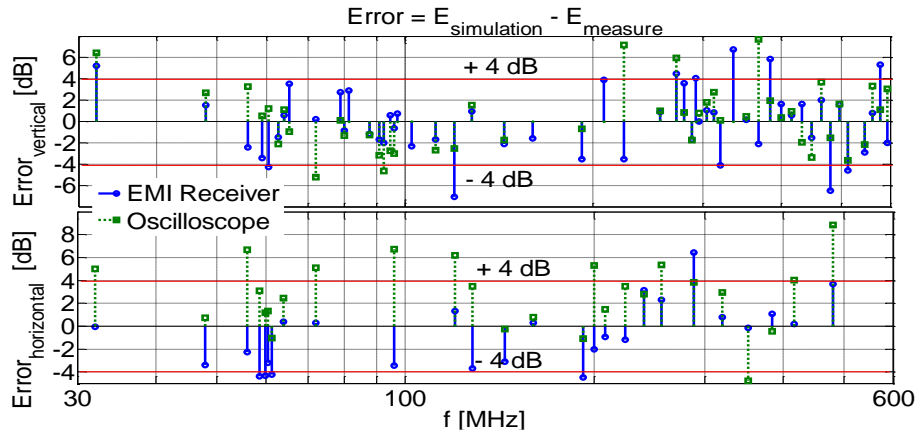
**Figure 4.27** Deviations of calculated fields based on the cable current scanned by the EMI receiver and the oscilloscope compared with the antenna measurement

Figure 4.28 shows the main radiation peaks of vertical or horizontal fields, which exceed the average limits according to CISPR 25. Some of these peaks might disturb the commercial frequency band, for example the peak at 96 MHz is located in FM band and it exceeds the class-2 limit. In addition, the common-mode current distributions with respect to these peaks are also depicted. They flow along the cable bundle in the form of current standing wave. From these curves, a current distribution in the order of several decibels in μA also may exceed the radiation limit, for example the maximal value of current distribution at 384 MHz is less than about 10 dBμA.
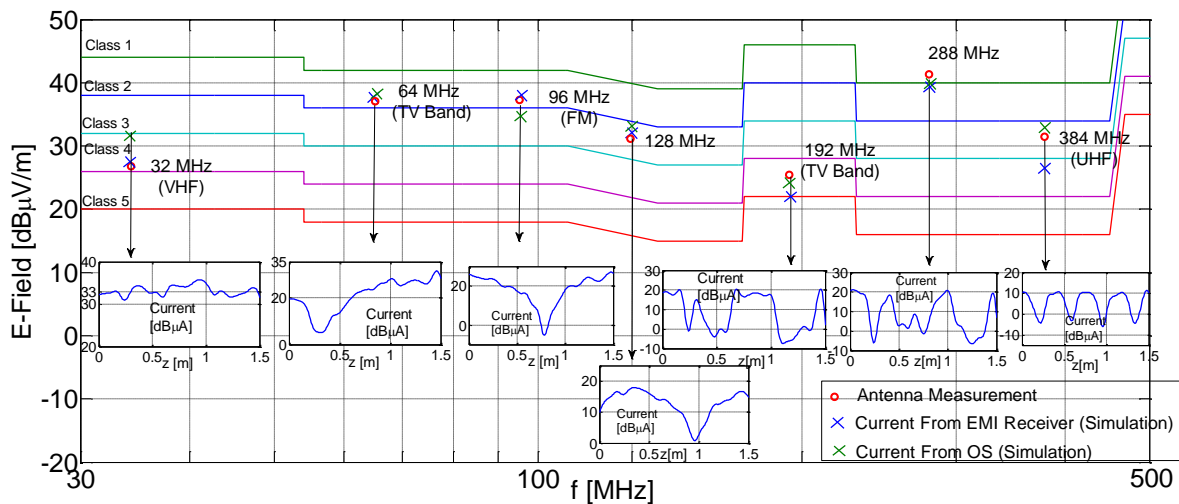


**Figure 4.28** Average limits for radiated disturbs from CISRP 25 and main radiation peaks from stepper motor drive system associated with the corresponding common-mode current distributions

As well as the prediction of radiated emissions above 30 MHz, radiated emissions from the stepper-motor drive system at low frequencies are also investigated. Figure 4.24 (right) shows the active Rod antenna test set-up according to the ALSE method. Due to the difficulty of the proposed frequency-domain scan

method to predict the field emission at low frequencies, only time-domain scan method is applied here. Capacitive coupling from the metallic table to the chamber ground can be corrected by $K_C$ denoted in Figure 4.9. Calculated results from time-domain scan method and antenna measurement are both depicted in Figure 4.29. It can be seen that simulation has high accuracy at the clock frequency of 16 MHz and the first harmonic of 32 MHz, where the error is less than 2 dB. However, the results still have a large deviation below 5 MHz, due to the high sensitivity of the multi-dipole radiation model to phase distribution error. Moreover, the noise from the pre-amplifier during current acquisition at low frequencies is also an important factor in degradation of the prediction accuracy. In order to solve this problem at very low frequencies, the cable voltage measurement by the CVP with correction function $K_{CVP}$ is another alternative as shown in Figure 4.9. Figure 4.30 depicts the vertical field from direct antenna measurement and the cable voltage minus $K_{CVP}$ in decibel. Compared with cable-current based alternative, the cable-voltage based method can obtain better prediction accuracy with higher reliability below 5 MHz.
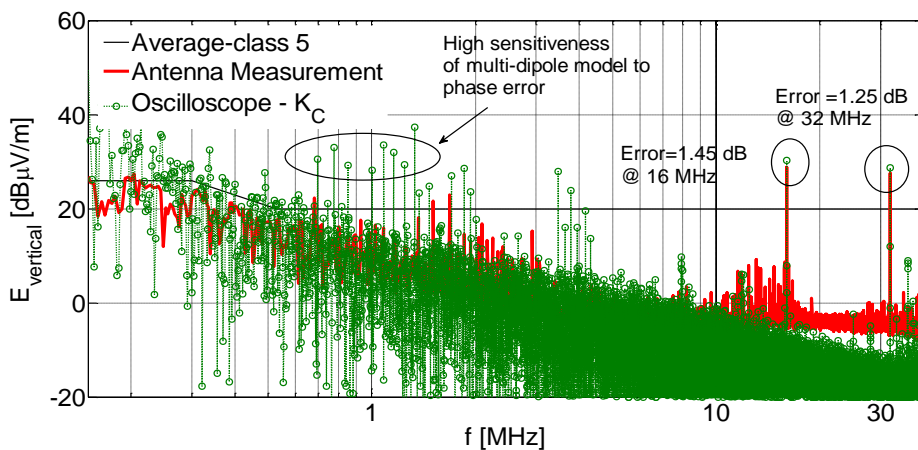


**Figure 4.29** Vertical electric fields from the stepper-motor drive system by the antenna measurement and the simulation based on the cable current scanned by the oscilloscope
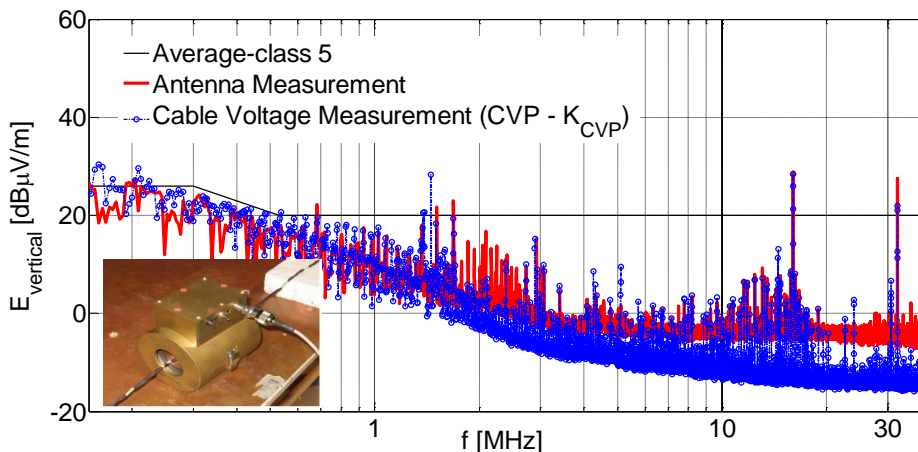


**Figure 4.30** Vertical electric fields from the stepper-motor drive system by the antenna measurement and the cable voltage measurement

87

# 4.4 Limitations of Current Scan Methods in Radiation Prediction

From the verification results above, the proposed alternative based on current scan can achieve good prediction accuracy in the component radiation estimation. However, the limitations in the alternative should be concerned in real applications. This alternative mainly includes three individual steps: common-mode current measurement; radiated field calculation; radiated field correction, as shown in Figure 4.31. Limitations and errors from each step may reduce the predication accuracy in final radiation estimation.

| Cable Current Measurement | Radiated Field Calculation | Radiated Field Correction |
|---|---|---|
| **Current Scanned by EMI Receiver**<br><br>- Unavailability in physics of retrieved transmission line parameters for a cable bundle | **Multi-Dipole Model of Cable**<br><br>- High sensitiveness to phase deviation below 30 MHz<br><br>- Approximation of EUTs and Loads by Simple Vertical Currents | **Calibration by ALSE Method**<br><br>- Unreliability of correction functions around some frequencies due to different load terminations in ALSE calibration<br><br>- Hardship of horizontal field measurement at high frequencies in ALSE calibration |
| **Current Scanned by Oscilloscope**<br><br>- Limited Dynamics<br>- Failure of triggering<br>- Errors in FFT Algorithm | **Surface Current Model of Finite Ground**<br><br>- Deviation due to the approximation of surface current calculation | |

**Figure 4.31** Process of the proposed alternative of radiation test and the limitations in each step

In the step of cable current measurement, the common-mode current distribution can be acquired in the frequency domain and time domain. In the frequency domain, the phase information can be retrieved based on the equivalent transmission line model, of which parameters are searched by an optimization algorithm. However, these parameters may lose their physical meanings due to current amplitude measurement error. Under this condition, it is difficult to use them for the further simulation, for example the calculation of load impedance. In time domain, the phase can be directly derived from the time-domain measurement by FFT. However, this current acquisition approach might be limited by the lower measurement dynamics of oscilloscope, possible triggering failure, and errors from FFT algorithm.

In the step of radiation field calculation, the proposed multi-dipole model for a cable bundle is accurate in the considered frequency range from 1 MHz to 1 GHz. However, in real applications the accuracy of this model is often reduced by the phase error below 30 MHz. The proposed surface current model for a finite ground

plate is not accurate at some frequencies in horizontal field simulation from 30 MHz to 1 GHz, since this model calculates the surface current on the assumption of an infinite ground. In addition, the EUT and load components are modeling by simple vertical current paths, which might reduce the prediction accuracy.

In the step of radiation field correction, the correction functions of vertical fields are unreliable at the resonance minimums in the calibration by the Bilog antenna. The correction functions of horizontal fields at some frequencies are unreliable mainly due to the antenna measurement sensitivity to the changes in test configuration.

Besides the discussed limitations in each implementation step, another issue is the proposed alternative assumes that the long cable structure dominates the radiated field in the radiation test configuration. Automotive component test methods usually attempt to reach correlation with real vehicle configuration, where some components with the shielded enclosures, some without enclosures. Additionally, unlike the cable bundle which has a certain length, the varying size of the components increases the difficulty in establishing a general radiation model. In this thesis, the experimental verifications of a twisted-pair cable and a cable bundle with seven-wire did not consider the extended EUT structures. The control unit in the stepper-motor drive system was well shielded intentionally to exclude the PCB radiation. In these verifications, current scan methods show good correlation with the full-compliance ALSE method for radiation estimation.

However, in some measurements the radiation from the non-cable component might change the cable radiation level, especially at higher frequencies. Here the stepper-motor drive system is further investigated when the control unit is shielded or unshielded. The results at some radiation peaks have deviations of several decibels, compared with the results shown before, due to the fact that these two measurements are implemented at different times. Small changes in configuration (antenna location, coaxial connected cable and peripheral equipment) might change some decibels at the radiation peaks. But this has no impact on the investigation of the radiation level from EUT. Figure 4.32 and Figure 4.33 shows the electric fields in the Bilog antenna measurement when EUT is shielded and unshielded, according to the configuration of Figure 4.24 (left). The main radiation peaks of both conditions are basically on a similar level. Compared with the shielded EUT, the vertical field in the measurement of unshielded EUT is increased by more than 5 dB at 32 MHz, 224 MHz, and 416.2 MHz. Another cluster of new peaks from 544.2 MHz to 624 MHz can also be observed. The horizontal field is increased by more than 5 dB at 48 MHz, 72 MHz, 192 MHz and 320 MHz.
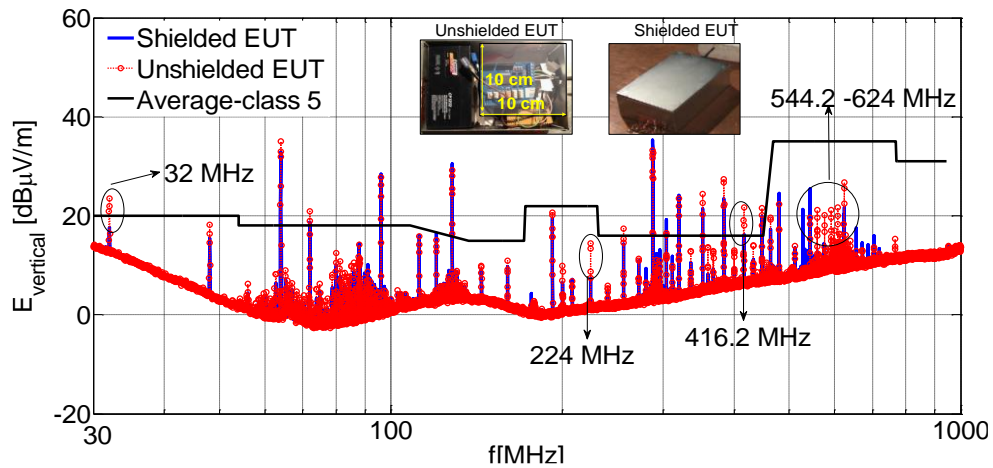
**Figure 4.32** Comparison of the vertical electric field when the EUT of stepper-motor drive system is shielded and unshielded
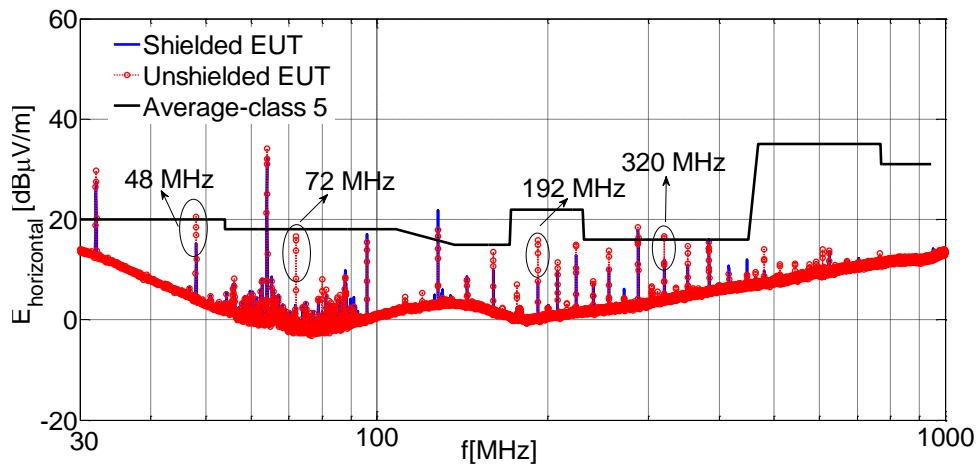


**Figure 4.33** Comparison of the horizontal electric field when the EUT of stepper-motor drive system is shielded and unshielded

# 4.5  Chapter Conclusion

This chapter has introduced several approaches to simulate the influence of finite ground, which could be used to improve the accuracy of proposed current scan methods. The edge currents can be used to predict the vertical field at the observation point, but fails to predict the horizontal field, as shown in Figure 4.3. Therefore, the more accurate surface current model has been proposed, which represents the finite ground plate by equivalent surface currents. This approximation model performed well in both vertical and horizontal polarizations at the observation point, as shown in Figure 4.6. Compared with the full-wave MoM model, these approximated models are more easily programmed and have lower computational times. The verification results show that in comparison with infinite ground from 30 MHz to 1 GHz, finite ground plate reduces the radiation by about 6 dB in the vertical field, but increases the radiation by about 20 dB to 25 dB in the horizontal field.

90

Due to the difficulty of modeling real ALSE test environments, a calibration procedure based on measured data has been proposed. In calibration of an active Rod antenna test from 150 kHz to 30 MHz, the antenna frequency response often suffers from the capacitive coupling between the metallic table and the chamber floor, as well as the inductive coupling of connected coaxial cable to antenna. Multi-dipole radiation model associated with simple mirror theory is expected to show good perform to simulate the test configuration below 30 MHz. However, the high sensitivity of multi-dipole model to phase error often leads to failure in the electric field prediction by current measurements. Therefore, common-mode voltage measurement by CVP which is characterized by a more stable frequency response may be a feasible solution, especially at very low frequencies below 5 MHz. In the calibration of Bilog antenna test from 30 MHz to 1 GHz, the calibrations based on frequency-domain and time-domain current scan methods have been both implemented. Averaging correction functions from different load impedances in calibration procedure is an effective measure to improve calibration accuracy.

To verify the proposed current scan methods, radiation models, and calibration procedure, a seven wires cable bundle with randomly selected terminals and a stepper-motor drive system have been designed. When EUTs or loads have little or no radiation contribution, the proposed alternative have only several decibels deviation at the main radiation peaks from 30 MHz to 1 GHz. Compared with the antenna measurement by ALSE method, the prediction error in vertical field by proposed current scan methods can be less than 5 dB at main peaks; prediction error in horizontal field can be less than about 6 dB at most main peaks. Generally speaking, the current scan method in frequency domain shows better performance than the method in time domain. Even though the current scanned by an oscilloscope can directly acquire the current amplitude and phase, higher noise floor, rigid triggering condition and limitation of FFT algorithm make this method suffer from more instabilities and uncertainties. From 150 kHz to 30 MHz the current scan method in frequency domain shows low performance, due to the high sensitivity of multi-dipole model to retrieved phase deviation. FFT based phase in time domain scan method can partly extend the availability of multi-dipole model down to 10 MHz. For lower frequencies, cable common-mode voltage measurement has been recommended to be as an effective solution. In addition, limitations in the proposed methods are also discussed in this chapter.

# Conclusion and Outlook

In radiated emission test of automotive components, the well-known ALSE method as specified in CISPR 25 is assumed to show the best correlation to the device emission behavior in a vehicle. However, this full-compliance test method requires an expensive anechoic chamber. In this context, a low-cost alternative based on the measurements of cable common-mode currents, for the estimation of the radiated emissions of automotive components has been developed. Linked to this alternative, three problems have been solved: firstly, frequency- and time-domain current scan methods are proposed to acquire the needed common-mode current distribution (amplitude and phase) on a cable bundle; secondly, electric-dipole based common-mode radiation model for a cable bundle is used; thirdly, taking real ALSE test environment into account, simpler radiation model for finite ground plate and measurements based calibration method are developed. Capabilities and limitations of these solutions have been investigated and discussed.

To acquire the common-mode current on a cable bundle, this thesis has proposed two current scan methods in frequency- and time-domain. Frequency-domain scan method can measure the common-mode current amplitude distribution on a cable bundle by frequency-domain receiving equipment, e.g. an EMI receiver. The deficient phase information is retrieved by an optimization algorithm, only from the acknowledgement of measured amplitude data. *Trust-Region-Reflective* iterative algorithm has been introduced as optimization algorithm to find equivalent common-mode transmission line parameters of the cable bundle, and further to retrieve the phase information. Time-domain scan method derives the amplitude and phase distribution directly from an oscilloscope measurement through FFT. But an additional signal is needed to provide a reference phase. These two current scan methods can both successfully acquire the common-mode amplitude and phase distributions in concerned frequency range (150 kHz to 1 GHz), if currents with sufficient  amplitude flows on the cable. Due to measurement errors, the retrieved equivalent transmission line parameters often lose their physics meanings, but the mathematics based retrieval algorithm can guarantee the phase accuracy up to 1 GHz. Additionally, the minimum measurable value is mainly limited by the sensitivity from the receiving equipment. Frequency-domain scan method can reach great measurement dynamics, for example -13 dBμV noise floor and -10 dBμV amplitude sensitivity with respect to the used EMI receiver. However, the time-domain scan method suffers from lower measurement dynamics, for example 18 dBμV noise floor and 24.8 dBμV amplitude sensitivity with respect to a typical setting of oscilloscope. In practice, a higher level than the noise floor (about 12 dB) is needed to get stable measured amplitude and phase distribution. Averaging of sweeps is a useful technique to reduce the noise floor significantly (down to -6 dBμV), but the amplitude

sensitivity is still kept on about 20 dBµV level due to the sensitivity limited by the 8-bit oscilloscope (2/$2^8$ mV or 17.9 dBµV). Besides the sensitivity limit by the oscilloscope, the trigger voltage level is another important factor to ensure successful data acquisition.

To establish an appropriate radiation model for a cable bundle, the common- and differential-mode radiations from the cable bundle have been firstly analyzed through simulations. From these simulations, it is reasonable to ignore differential-mode radiation with respect to a typical radiation configuration, if the cross-sectional radius of the cable bundle is less than 1 cm. Also, the axial-central line of the cable bundle as the equivalent common-mode path in the radiation model is accurate enough, which only induces less than 2 dB error in worst case. Based on this equivalent model, a multi-dipole model has been proposed to predict common-mode radiation from a cable bundle. Each electric dipole source is fed with the acquired current from current scan. Three aspects of the real application have been considered, to guarantee the prediction accuracy when using the multi-dipole model and current scan methods. First of all, the currents on vertical segments from the cable bundle to ground (Figure 3.12) can be approximated by the measured currents at the start and end points of the cable bundle. It gives good accuracy in vertical field prediction up to 600 MHz and horizontal field prediction up to 1 GHz. Extrapolated approximation based on known transmission line parameters can improve the accuracy up to 1 GHz in both vertical and horizontal field. Secondly, taking into account the size of EUT or load components, the simplified vertical segments as electric dipoles in radiation model might influence radiation accuracy. Simulations have shown that the length of vertical segments (ΔL is shown in Figure 3.12) in the radiation model within 1 cm changes only induce less than 2 dB error at the vertical and horizontal field peaks, but it has a big influence on the resonance minimums of horizontal field. And the position offset of the vertical segments (Δz is shown in Figure 3.12) within 3 cm nearly has no influence on the vertical and horizontal field peaks, but it will induce the frequency shift at most resonance minimums, especially in vertical field component. Thirdly, considering the standing wave property of the current amplitude distribution, it is nearly impossible to acquire all the current information especially around amplitude resonance minimums. Two solutions have been introduced to reconstruct these missing current data: transmission line model and interpolation function. However, simulations have shown that these solutions fail when the missing current amplitude below the sensitivity limit or noise floor 0.3·SWR (dB) or more (SWR is defined by (3.8)), i.e. too much deficient current data will lead to the failure of reconstructing complete current amplitude and phase distribution by the solutions.

To improve the comparability of proposed alternative to full-compliance ALSE test method, different simulation models for finite ground plate in ALSE configuration

have been discussed. Eddy current model can predict the vertical field at observation point successfully, but fail to predict the horizontal field. Improved surface current model, much simpler compared with MoM model, has given good prediction accuracy in both vertical and horizontal polarization. Simulations have shown that the finite ground plate can reduce the vertical radiated field at peaks about 6 dB, but enhance the horizontal field up to 20 dB to 25 dB from 30 MHz to 1 GHz. However, other radiation influence factors from ALSE environment are hard to model due to their complexity and uncertainty, for example test antenna and reflections from absorber walls. Therefore, a measurement based calibration process has been developed to incorporate real test environmental factors. The correction function is calculated as difference between the antenna measured field and the simulated field based on the proposed radiation model. For the calibration of active Rod antenna set-up from 150 kHz to 30 MHz, an apparent difference between the antenna measurement and the simulation from 2 MHz to 30MHz can be observed, due to the capacitive coupling of antenna set-up. This difference can be as a correction function to incorporate the measurement coupling influence. But at lower frequencies, the high sensitivity of the multi-dipole radiation model to phase error might lead to the electric field calculation error. Therefore, the cable common-mode voltage measurement by CVP with a stable correction function (below 5 MHz) would be a more feasible solution to this problem. For the calibration of Bilog antenna set-up from 30 MHz to 1 GHz, surface current model has been used to simulate the finite ground plate. The model errors due to surface current approximation from 30 MHz to 40 MHz and 150 MHz to 220 MHz can be observed. But these model errors are also incorporated into the correction function. Moreover, utilizing average correction function from the wire with different loads in calibration procedure is an effective measure to improve the accuracy.

The developed alternative can be summarized to three individual steps for radiation estimation: the current acquisition, the radiation prediction based on multi-dipole radiation model for a cable bundle and surface current model for a finite ground plate, and the predicted field corrected by the functions from ALSE measurements. To verify this alternative, several cable structures have been investigated. In the verifications of a twisted-pair cable and a seven-wire cable bundle, the measurements using a short rod antenna directly on a ground plate verify the current acquisition methods in frequency- and time-domain, as well as multi-dipole radiation model for a cable bundle. In the verification of the seven-wire cable bundle and a stepper-motor system using full CISPR 25 compliant set-up verify all the steps in the proposed alternative. From the results, maximal prediction deviation is below 6 dB at most frequencies using current scan methods, compared with direct antenna measurements from 30 MHz to 1GHz. Moreover, the prediction accuracy in vertical field is higher than horizontal field. And the accuracy based on frequency-

domain current measurements is higher than time-domain current measurements. But from 150 kHz to 30 MHz, calculated phase in frequency-domain current scan method results in a big error in the electric field prediction using the proposed multi-dipole model. Directly measured phase in time-domain current scan method performs better from 10 MHz to 30 MHz. For very lower frequencies, common-mode voltage measurement with correction function can achieve good accuracy in electric field prediction.

The proposed alternative performs better than previous works. However, there are some aspects of the proposed alternative to improve in future work. For the current acquisition, time-domain scan method by an oscilloscope needs further investigation to guarantee higher accuracy, especially for phase measurement. For the radiation models, multi-dipole model for a cable bundle has an apparent error in the prediction of the electric field below 30 MHz, due to its high sensitivity to the insufficient phase accuracy. Simple approximation of various EUTs or loads by a single vertical current path might reduce the prediction accuracy at higher frequencies. Moreover, surface current approximation model for a finite ground plate has deviations at some frequencies. Therefore, more accurate models are needed, such as MoM-based radiation model. For the calibration procedure, the stability and reliability of the correction function for horizontal polarization should be considered in more detail.

# Reference

[1]   K. Reif: "*Bosch Autoelektrik und Autoelektronik: Bordnetze, Sensoren und elektronische Systeme*," Vieweg+Teubner Verlag, Spinger Fachmedien Wiesbaden GmbH,  2011.

[2]   A. Emadi, Y. J. Lee, K. Rajashekara: "*Power Electronics and Motor Drives in Electric, Hybrid Electric and Plug-In Hybrid Electric Vehicles*," IEEE Transactions on Industrial Electronics, 55(6): 2237-2245, June 2008.

[3]   T. Steinbach, F. Korf, T. C. Schmidt: "*Comparing time-triggered Ethernet with FlexRay: An evaluation of competing approaches to real-time for in-vehicle networks*," IEEE International Workshop on Factory Communication Systems, pp. 199-202, May 2010.

[4]   T. Kosch: "*Car2Car Communication Concepts*," IEE on Automotive Electronics, pp. 253-262, March 2006.

[5]   Institution of Engineering and Technology (IET): "*Electromagnetic Compatibility for Functional Safety*," England&Wales, 2008.

[6]   M. Mardiguian: "*Controlling Radiated Emissions by Design, Second Edition*," Kluwer Academic Publisher, Massachusetts, 2001.

[7]   Y. L. Zheng: "*Equivalent Cable Bundle Method for Simulating Automotive Electromagnetic Compatibility*," Dissertation, Chongqing University, 2011.

[8]   K. Siebert: "*Entiwicklung von Mehrleitermodellen für Signalintegritäts- und EMV-Anlysen von Kfz-Busystemen*," Dissertation, TU Dortmund, 2013.

[9]   CISPR 25 Ed.3.0: "*Vehicles, boats and internal combustion engines-Radio disturbance characteristics – Limits and methods of measurements for the protection of on-board receivers*," 2007.

[10]  W. T. Smith, K. Frazier: "*Prediction of Anechoic Chamber Radiated Emissions Measurements through Use of Empirically-Derived Transfer Functions and Laboratory Common-Mode Current Measurements*," IEEE International Symposium on Electromagnetic Compatibility, pp.387-392, August 1998.

[11]  D. Schneider, M. Bottcher, B. Schoch, S. Hurst: "*Transfer functions and current distribution algorithm for the calculation of radiated emissions of automotive components*," EMC Europe, Brugge, pp.443-448, September 2013.

[12]  H. Rebholz, S. Tenbohlen: "*A fast radiated emission model for arbitrary cable harness configurations based on measurements and simulations*," IEEE International Symposium on Electromagnetic Compatibility, pp.1-5, August 2008.

[13]  A. Radchenko, V. V. Khilkevich, N. Bondarenko, D. Pommerenke, M. Gonser, J. Hansen, C. Keller: "*Transfer Function Method for Predicting the Emissions in a CISPR-25 Test-Setup*," IEEE Transactions on Electromagnetic Compatibility, 56(4): 894-902, August 2014.

[14]  G. H. Li, W. Qian, A. Radchenko, G. Hess: "*Estimating the radiated emissions from cables attached to a switching power supply in a MIL-STD 461 test*," IEEE International Symposium on Electromagnetic Compatibility, pp.626-631, August 2014.

[15] F. Kremer, S. Frei: "*Modellierung des Stoeraussendungsverhaltens von Kfz-Hochspannungsbordnetzen in VHDL-AMS,*" ASIM, Krefeld, 2011.

[16] G. Ala, M.C. Di Piazza, G. Tine, F. Viola, G. Vitale: "*Evaluation of Radiated EMI in 42-V Vehicle Electrical Systems by FDTD Simulation,*" IEEE Transactions on Vehicular Technology, 56(4):1477-1484, 2008.

[17] G. Andrieu, A. Reineix, X. Bunlon, J. P. Parmantier, L. Kone, B. Demoulin: "*Extension of the "Equivalent Cable Bundle Method" for Modeling Electromagnetic Emissions of Complex Cable Bundle,*" IEEE Transactions on Electromagnetic Compatibility, 51(1): 108-118, February 2009.

[18] F. J. Bongartz, J. Deckers, M. Heina, H. Hirsch: "*Proposal for the validation of absorber lines shielded enclosures for CISPR 25 emission tests,*" IEEE International Symposium on Electromagnetic Compatibility, pp.116-120, August 2009.

[19] S. Sun, G. Liu, J. L. Drewniak, D. J. Pommerenke: "*Hand-Assembled Cable Bundle Modeling for Crosstalk and Common-Mode Radiation Prediction,*" IEEE Transactions on Electromagnetic Compatibility, 49(3): 708-718, 2007.

[20] S. Frei: "Kfz-Bordnetze," Dortmund, 2010.

[21] G. L. Maxam, H. P. Hsu, P. W. Wood: "*Radiated ignition noise due to the individual cylinders of an automobile engine,*" IEEE Transaction on Vehicular Technology, 25(5): 33-38, 1976.

[22] T. Rybak, M. Steffka: "*Automotive Electromagnetic Compatibility,*" Kluwer Academic Publisher, 2004.

[23] S. Niedzwiedz, S. Frei: "*Transient Emission Analysis of EV- and HEV-Powertrains using Simulation,*" EMC Europe 2013, Brugge, pp.247-252, September 2013.

[24] M. Gursoy, S. Jahn, B. Deutschmann, G. Pelz: "*Methodology to Predict EME Effects in CAN Bus Systems Using VHDL-AMS,*" IEEE transactions on Electromagnetic Compatibility, 50(4): 993-1002, 2008.

[25] J. Jia, S. Frei: "*Analysis of radiated emissions from flexray automotive bus system,*" EMC Europe 2011, York, pp.234-239, September 2011.

[26] T. Williams: "*EMC for Product Designers, Four Edition,*" Elsevier, 2007.

[27] MIL-STD-461E: "*USA Department of Defense Interface Standard, Requirements for the Control of Electromagnetic Interference Characteristics of Subsystems and Equipment,*" August 1999.

[28] MIL-STD-461F: "*USA Department of Defense Interface Standard, Requirements for the Control of Electromagnetic Interference Characteristics of Subsystems and Equipment,*" December 2007.

[29] Ford Motor Company ES-XW7T-1A278-AC: "*Component and Subsystem Electromagnetic Compatibility: Worldwide Requirements and Test Procedure,*" October 2003.

[30] C. R. Paul: "*Introduction to Electromagnetic Compatibility, Second Edition,*" John Wiley&Sons, Inc., 2006.

[31] C. A. Balanis: "*Antenna Theory: Analysis and Design, Second Edition,*" John Wiley&Sons, Inc., 1997.

[32] C. Capps: "*Near Field or Far Field*," EDN, August, 2001.

[33] J. D. Kraus, R. J. Marhefka: "*Antenna: For All Applications, Third Edition*," The McGraw-Hill Companies, Inc., 2002.

[34] D. Warkentin, A. Wang, W. Crunkhorn: "*Shield enclosure accuracy improvement for MIL-STD-461E radiated emissions measurement*," IEEE International Symposium on Electromagnetic Compatibility, pp: 404-409, 2005.

[35] D. D. Swanson: "*Analysis of MIL-STD-461E and MIL-STD-461F RE 102 Test setup configurations below 100 MHz*," IEEE International Symposium on Electromagnetic Compatibility, pp.1-11, August 2008.

[36] C. W. Fanning: "*Improving monopole radiated emission measurement accuracy; RF chamber influences, antenna height and counterpoise grounding (CISPR 25; MIL-STD-461E vs. MIL-STD-461F)*," IEEE International Symposium on Electromagnetic Compatibility, pp.103-108, August 2009.

[37] T. Omori, H. Sasaki, H. Jing, R. K. Robin: "*Antenna design and its application for near field disturbance measurement in upper VHF band*," IEEE International Symposium on Electromagnetic Compatibility, pp.18-23, August 2008.

[38] T. Burghart, H. Rossmanith, G. Schubert: "*Evaluation the RF-emissions of automotive cable harness*," IEEE International Symposium on Electromagnetic Compatibility, pp.787-791, August 2004.

[39] H. D. Li: "*Investigations into the radiated emission test according to CISPR 25 ALSE method*," IEEE International Symposium on Electromagnetic Compatibility, pp.400-403, August 2005.

[40] A. Kriz, W. Milliner: "*Analysis of the CISPR 25 component test setup*," IEEE International Symposium on Electromagnetic Compatibility, pp.229-232, August 2003.

[41] M. J. Alexander, M. J. Salter, D. G. Gentle, D. A. Knight, B. G. Loader, K. P. Holland: "*Calibration and use of antennas, focusing on EMC application*," National Physical Laboratory, Teddington, UK, December 2004.

[42] CISPR 16-4-2, Ed.1.0: "*Specifications for radio disturbance and immunity measuring apparatus and method-part 4-2: Uncertainties, statistics and limit modeling- Uncertainties in EMC measurement*," November 2003.

[43] R. Neumayer, A. Stelzer: "*Continuous simulation of system-level automobile EMC problems*," IEEE International Symposium on Electromagnetic Compatibility, 1(8): 409-413, 2003.

[44] J. Jia, F. Kremer, S. Frei: "*Modellierung von CISPR-25 Antennenmessungen mittels schneller approximierender Berechnungsverfahren*," EMV-Düsseldorf, Germany, 2012.

[45] Giovanni Miano, Antonio Maffucci: "*Transmission Lines and Lumped Circuits*," Academic Press, New York, 2001.

[46] J. Nitsch, F. Gronwald, G. Wollenberg: "*Radiation Non-uniform Transmission Line System and the Partial Element Equivalent Circuit Method*," John Wiley&Sons, Inc., Unite Kingdom, 2009.

[47] M. T. Frederick, V. I. Michel, K. Torbjörn: "*EMC Analysis Methods and Computation Models*," John Wiley&Sons, Inc., 1997.

[48] C. R. Paul: "*Analysis of Multiconductor Transmission Lines*," John Wiley&Sons, Inc., 2007.

[49] J. Nitsch, C. E. Baum, R. Sturm: "*Analytical treatment of circulate non-uniform multicondutor transmission lines*," IEEE transactions on Electromagnetic Compatibility, 34(1): 28-38, 1992.

[50] J. Jia, D. Rinas, S. Frei: "*Prediction of radiated fields from cable bundle based on current distribution measurement*," EMC Europe 2012, Rome, pp.1-7, September 2012.

[51] Y. Vives-Gilabert, C. Arcambal, A. Louis, F. de Daran, P. Eudeline, B. Mazari: "*Modeling Magnetic Radiations of Electronic Circuit Using Near-Field Scanning Method*," IEEE transactions on Electromagnetic Compatibility, 49(2): 391-400, 2007.

[52] M. Y. Koledintseva, J. L. Drewniak, T. P. Van Doren, D. J. Pommerenke, M. Cocchini: "*Method of Edge Currents for Calculating Mutual External Inductance in a Microstrip Structure*," Progress In Electromagnetics Research, PIER 80, 197-224, 2008.

[53] V. Vladimir, G. A. E. Vandenbosch: "*Efficient Physical Optics Approximation for the Calculation of Radiation Patterns of Planar Antenna Located on a Finite Ground Plane*," IEEE transactions on Electromagnetic Compatibility, 53(1): 460-465, January, 2005.

[54] W. D. Rawle: "*The Method of Moments: A numerical Technique for Wire Antenna Design*," High Frequency Electronics, 5: 42-47, 2006.

[55] M. N. O. Sadiku: "*Numerical Techniques in Electromagnetics, Second Edition*," CRC Press LLC, 2001.

[56] C. S. Desai, J. F. Abel: "*Introduction to the Finite Element Method: A Numerical Approach for Engineering Analysis*," Van Nostrand Reinhold, New York, 1972.

[57] P. K. Banerjee: "*The Boundary Element Method in Engineering*," McGraw-Hill College, 1994.

[58] T. Weiland: "*A discretization method for the solution of Maxwell's equations for six-component Fields*," Electronics and Communications AEUE, 31(3): 116-120, 1977.

[59] K. S. Yee: "*Numerical solution of initial boundary-value problems involving Maxwell's equations in isotropic media*," IEEE transactions on Antenna and Propagation, 14: 302-307, May, 1966.

[60] C. Christopoulos: "*The Transmission-Line Modeling (TLM)*," IEEE Press, New York, 1995.

[61] H. Chobanyan, I. Badzagua, T. Injgia, A. Gheonjian: "*Application of hybrid MoM/MTL method to simulation of interaction between cable harness and antennas*," Direct and Inverse Problems of Electromagnetic and Acoustic Wave Theory, pp.33-38, 2009.

[62] F. Sabath, H. Garbe: "*Radiation analysis of PCB layout using a hybrid MoM-MTL method*," IEEE Transactions on Electromagnetic Compatibility, 45(2): 424-435, 2003.

[63] D. D. Ward, S. Lawton: "*Numeric Modeling for Automotive EMC*," IEEE

International Symposium on Electromagnetic Compatibility, pp.222-227, 1995.

[64] G. Andrieu, A. Reineix, X. Bunlon, J. P. Parmantier, L. Kone, B. Demoulin: "*Extension of the Equivalent Cable Bundle Method for Modeling Electromagnetic Emissions of Complex Cable Bundle*," IEEE Transaction on Electromagnetic Compatibility, 51(1):108-118, February 2009.

[65] C. Poudroux, M. Rifi: "*A simplified approach to determine the amplitude of the transient voltage induced on a cable bundle*," IEEE Transactions on Electromagnetic Compatibility, 37(4): 497-504, 1995.

[66] S. Frei: "*Where we stand today with automotive EMC simulation*," IEEE International Symposium on Electromagnetic Compatibility, pp.1-9, 2008.

[67] F. Grassi, G. Spadacini, F. Marliani, S. A. Pignari: "*Use of double bulk current injection for susceptibility testing of avionics*", IEEE Transaction on Electromagnetic Compatibility, 50(3):524-535, August 2008.

[68] J. Meng, Y. X. Teo, D. W. P. Thomas, C. Christopoulos: "*Fast Prediction of Transmission Line Radiated Emissions Using the Hertzian Dipole Method and Line-End Discontinuity Models*," IEEE Transaction on Electromagnetic Compatibility, PP(99):1-9, May 2014.

[69] S. Frei, R. G. Jobava, D. Topchishvili: "*Complex Approaches for the Calculation of EMC Problems of Large Systems*," IEEE International Symposium on Electromagnetic Compatibility, 3(8):826-831, 2004.

[70] D. Rinas, S. Niedzwiedz, J. Jia, S. Frei: "*Optimization methods for equivalent source identification and electromagnetic model creation based on near-field measurements,*" EMC Europe, York, pp.298-303, September 2011.

[71] T. Isernia, G. Leone, R. Pierri: "*Radiation pattern evaluation from near-field intensities on planes*," IEEE Transaction on Antennas Propagation, 44(5): 701-710, May 1996.

[72] M. Meyer, P. Asfaux: "*Radiated emissions modeling of a power cable*," IEEE International Symposium on Electromagnetic Compatibility, Hamburg, pp.1-5, September 2008.

[73] *Help Handbook* in Matlab version R2010a, Mathworks Inc., Natick, Massachusetts, 2010.

[74] K. Siebert, H. Gunther, S. Frei, W. Mickisch: "*Modeling of frequency Dependent Losses of Transmission Lines with VHDL-AMS in Time Domain*," International Zurich EMC Symposium, Zurich, Switzerland, 2009, pp.313-316, Jan. 2009.

[75] O. Zinke, H. Brunswig: "*Lehrbuch der Hochfrequenztechnik*," Springer, 1986.

[76] Operator's Manual of X-stream Oscilloscope, Lecroy Co., NY, 2007.

[77] V. Janssen*: "Accelerated EMI Measurements with Time Domain Scan,"* EMC Europe, Tutorial, Rome, September 2012.

[78] E. Bogatin: "*Signal Integrity: Simplified*," Pearson education. Inc. 2004.

[79] S. A. Pignari, D. Bellan: "*Incorporating vertical risers in the transmission line equations with external sources*," IEEE International Symposium on Electromagnetic Compatibility, pp.974-979, 2004.

[80] S. Frei, T. Nägel; R.Jobava: "*Bestimmung der Störaussendung im KFZ durch*

*die getrennte Betrachtung der elektrischen und magnetischen Verkopplungen*,"
EMV-Düsseldorf, Germany, 2004.

# Publications of Author Jin Jia

1. J. Jia, A. Zeichner, D. Rinas, S. Frei, "*Anwendung von alternativen Verfahren zur Vorhersage von EMV Antennemessergebnissen nach CISPR-25,*" EMV-Düsseldorf, Germany, 2014.

2. J. Jia, D. Rinas, S. Frei: "*An Alternative Method for Measurement of Radiated Emissions According to CISPR 25,*" EMC Europe 2013, Brugge, pp.304-309, September 2013.

3. J. Jia, D. Rinas, S. Frei: "*Prediction of radiated fields from cable bundles based on current distribution measurements,*" EMC Europe 2012, Rome, pp.1-7, September 2012, **also referred as [50] in this thesis**.

4. J. Jia, F. Kremer, S. Frei: "*Modellierung von CISPR-25 Antennenmessungen mittels schneller approximierender Berechnungsverfahren,*" EMV-Düsseldorf, Germany, 2012, **also referred as [44] in this thesis**.

5. J. Jia, S. Frei: "*Analysis of radiated emissions from flexray automotive bus system,*" EMC Europe 2011, York, pp.234-239, September 2011, **also referred as [25] in this thesis**.

6. F. Kremer, J. Jia, S. Frei: "*Simulationsbasierte Bewertung der zulässigen Kopplung zwischen verschiedenen Spannungsebenen in Elektrofahrzeugen,*" EMV-Düsseldorf, Germany, 2012.

7. D. Rinas, S. Niedzwiedz, J. Jia, S. Frei, "*Optimization methods for equivalent source identification and electromagnetic model creation based on near-field measurements,*" EMC Europe 2011, York, pp.298-303, September 2011**, also referred as [70] in this thesis**.

# Student Theses Supervised by Jin Jia

1. Y. Bao, "*Statistical Analysis of Common Mode Radiation due to Random Wire Positions in Automotive Cable Bundle*," Diplomarbeit, Dortmund, February 2012.

2. J. Ma, "*Entwicklung und Anwendung einer auf Feldscandaten basierenden Methode der Strahlungsmessung für Kfz-Komponenten*," Diplomarbeit, Dortmund, September 2013.

3. Y. Zhao, "*Untersuchung von Zeitbereichsmessmethoden für die Vorhersage von Störaussendungen auf Basis von Scan-Verfahren*," Bachelorarbeit, Dortmund, Juni 2014.

# Acknowledgement

In the past four and half years, studying for a doctoral degree abroad was a special experience. This period was full with challenges and excitements. Even though it was accompanied by the pressure from research task, sometimes the boredom of everyday life and the cultural difference, this experience gives me courage and confidence to pursue more accomplishments in further. Exact academic spirit and excellent research environment, deep in education system of Germany, improve me the capability of scientific independent thinking as well as the engineering practical quality.

Sincerely thanks for Prof. Dr.-Ing Stephan Frei to provide me a chance to conduct the research in On-Board System Lab, and give me many chances of academic activities in the past years. Moreover the experience of participating in industrial meeting enriches my research and studying. Because of his supervision and encouragement on my academic research, I can struggle with my research tasks and finally finish the dissertation. Also thanks for Prof. Dr.-Ing Frank Jenau, the leader of High Voltage Technique Lab, to read and modify this thesis.

Research is only one part of abroad life for a foreign student. Long-term living and studying alone sometimes discouraged me. Without the support from family in China, I nearly cannot continue my studying. I should especially thanks for my wife, Ruimiao Wang. Thanks for her understanding and full support, I can concentrate on my research and studying.

In these four and half years, I make many friends from different countries in On-Board System Lab. I gained a lot from the discussion with them in research process. Thanks for the colleagues of Dipl.-Ing. Denis Rinas and M. Sc. Zongyi Chen from near-field scan team, they provided a lot supports in my experiments. Thanks for M. Sc. Sergey Miropolsky and Dr.-Ing. Friedrich zur Nieden, they gave me a lot help at the beginning of my studying in Germany.

# Curriculum Vitae

**Personal Data**

| | |
|---|---|
| Name | Jin Jia |
| Date of Birth | February 28, 1985 |
| Place of Birth | Sichuan, China |

**Experience**

| | |
|---|---|
| Since 09/2010 | On-Board Systems Lab, Technical University of Dortmund, Germany. Research Assistant in a Ph .D program about: "Automotive Electromagnetic Compatibility" |
| 09/2007 – 07/2010 | College of Electrical Engineering, Chongqing University, Chongqing, China. Master thesis about: "Study on the Method of Electromagnetic Interference Prediction for Automotive Ignition System" |
| 03/2008 – 05/2009 | Changan Automobile, Chongqing, China. Working Student in R&D Center Electronics Division about: "Study on EMC for Automobile Electrical Systems" |
| 09/2003 – 07/2007 | College of Electrical Engineering, Chongqing University, Chongqing, China. Bachelor thesis about: "Developing and Applying the Element-Free Galerkin Method (EFGM) for Electromagnetic Computation" |

**Education**

| | |
|---|---|
| 09/2007 – 07/2010 | College of Electrical Engineering, Chongqing University, Chongqing, China (Master of Electrical Engineering Theory and New Technology) |
| 09/2003 – 07/2007 | College of Electrical Engineering, Chongqing University, Chongqing, China (Bachelor of Electrical Engineering and Automation) |
| 09/1997 – 07/2003 | Junior and Senior Middle School of Quxian, Sichuan, China |
| 09/1991 – 07/1997 | Primary School of Guifu, Sichuan, China |